The hole spin in a semiconductor quantum dot

Inauguraldissertation

zur
Erlangung der Würde eines Doktors der Philosophie

vorgelegt der
Philosophisch-Naturwissenschaftlichen Fakultät
der Universität Basel

von

Jonathan H. Prechtel

aus Wiesenbronn, Deutschland

Basel, 2015

Genehmigt von der Philosophisch-Naturwissenschaftlichen Fakultät auf Antrag von

Prof. Dr. Richard Warburton

Dr. Gian Salis

Basel, den 21.04.2015

Prof. Dr. Jörg Schibler
Dekan

Namensnennung - Nicht kommerziell - Keine Bearbeitungen 4.0 International

(CC BY-NC-ND 4.0)

Dies ist eine alltagssprachliche Zusammenfassung der **Lizenz** (die diese nicht ersetzt).

Haftungsbeschränkung

Sie dürfen:

Teilen — das Material in jedwedem Format oder Medium vervielfältigen und weiterverbreiten

Der Lizenzgeber kann diese Freiheiten nicht widerrufen solange Sie sich an die Lizenzbedingungen halten.

Unter folgenden Bedingungen:

Namensnennung — Sie müssen **angemessene Urheber- und Rechteangaben machen**, einen Link zur Lizenz beifügen und angeben, ob **Änderungen vorgenommen** wurden. Diese Angaben dürfen in jeder angemessenen Art und Weise gemacht werden, allerdings nicht so, dass der Eindruck entsteht, der Lizenzgeber unterstütze gerade Sie oder Ihre Nutzung besonders.

Nicht kommerziell — Sie dürfen das Material nicht für **kommerzielle Zwecke** nutzen.

Keine Bearbeitungen — Wenn Sie das Material **remixen, verändern oder darauf anderweitig direkt aufbauen** dürfen Sie die bearbeitete Fassung der Materials nicht verbreiten.

Keine weiteren Einschränkungen — Sie dürfen keine zusätzlichen Klauseln oder **technische Verfahren** einsetzen, die anderen rechtlich irgendetwas untersagen, was die Lizenz erlaubt.

Hinweise:

Sie müssen sich nicht an diese Lizenz halten hinsichtlich solcher Teile des Materials, die gemeinfrei sind, oder soweit Ihre Nutzungshandlungen durch **Ausnahmen und Schranken des Urheberrechts** gedeckt sind.

Es werden keine Garantien gegeben und auch keine Gewähr geleistet. Die Lizenz verschafft Ihnen möglicherweise nicht alle Erlaubnisse, die Sie für die jeweilige Nutzung brauchen. Es können beispielsweise andere Rechte wie **Persönlichkeits- und Datenschutzrechte** zu beachten sein, die Ihre Nutzung des Materials entsprechend beschränken.

"Isn't it funny how day by day nothing
changes but when you look back
everything is different..."

– C.S. Lewis

Preface

Extensive research on semiconductor quantum dots (QDs) has been a hot topic in the semiconductor community over the past 20 to 30 years and is still ongoing. In the late 1980s the term "quantum dot" was introduced to describe a semiconductor nano-structure. Some of the motivating prospects driving the research are low-threshold QD lasers, single dots for medical markers, lighting technologies for TVs or single spins for spintronic applications, e.g. quantum information processing. The size and the structure of a QD can vary from a few nanometres in colloidal dots (also known as nanocrystals) to a few hundred nanometres in lithographically defined electrostatic devices. The material components and the fabrication methods can differ a lot between the individual types of QDs. One feature all different kinds of QDs have in common is the restriction of the carrier motion in all three dimensions, which is induced by confinement. That property is the origin of the name zero-dimensional ("0D") structures. A second term often used describes the QD as an "artificial atom". The strong confinement establishes discrete energy states for the localized single carriers inside the QD, which resembles the properties of carriers in atoms. The QDs investigated in this thesis are self-assembled InAs QDs in a semiconductor heterostructure, laying the focus on the confined positive charged carriers, the holes. The spin properties of the individual quantum states are characterized with advanced optical spectroscopy techniques.

The following thesis is split into four parts. The first part motivates the search for coherent single hole spins and explains how to get from a bulk semiconductor to a single spin. After a short introduction of semiconductor self assembled quantum dots, their optical properties and bandstructure, the requirements to perform single spin physics are described. The advantage to choose the hole spin for a spin qubit instead of the electron spin, regarding their decoherence properties is discussed. The second section of the introduction covers the experimental techniques and improvements to current systems paving the way to a highly coherent spin qubit via the hole spin and high quality data. The new device structure as well as the sophisticated technique of resonance fluorescence detection are explained here. A description of the laser frequency locking mechanism and a power stabilization ("noise eater") concludes the chapter.

In the second part the first experiments of this thesis on coherent hole spins are presented. With the spectroscopic measurement method of coherent population trapping (CPT)

long decoherence times are achieved. Charge noise is determined as a hole spin dephasing mechanism. Despite the very promising results the experiment suffers from two disadvantages. First the measurement method via resonant absorption spectroscopy in combination with the unstable measurements conditions (laser fluctuations) offers a very poor signal to noise ratio. Secondly the low frequency charge fluctuations, inherent in the sample, promote dephasing and induce shifts in the CPT resonance position from scan to scan.

The third part covers different approaches to address the noise issue of part two. The optical linewidth and the noise are closely related in solid state emitters: The linewidth broadening is caused by spin and charge noise in the quantum device. First, low frequency charge fluctuations are reduced by a feedback scheme, which stabilizes the emission frequency of the quantum dot to a stabilized reference. The feedback loop minimizes the fluctuations in the emission frequency, even over several hours, and eliminates the charge noise in the quantum dot to a large extent. This method realises a frequency stabilized source of single photons in the solid-state. The next chapter introduces a new sample design in order to reduce spectral fluctuations. The n-i-p device growth sequence is inverted, which prevents the usual contamination of the QDs by the C-doping. The characteristics of the ultra clean p-doped samples are narrow linewidths in combination with high count rates. The "transform-limit" is reached with a fast scanning method. In the sample a voltage dependent blinking behaviour of the positively charged exciton is discovered. The story of low-noise samples and noise control continues in the next chapter. Transform-limited linewidth of the neutral and the negatively charged exciton are presented. For the neutral exciton this is even true for slow measurements lasting several seconds. For already low-noise structures the residual linewidth broadening is only caused by the nuclear spin noise. A two colour experiment provides control over the nuclear spins, which dominate the exciton dephasing.

In the last part the interaction of the hole spin with its environment is investigated. The hole spin states interact in an in-plane magnetic field with an external electric field. The interactions result in a tunable hole g-factor, showing a linear dependency over a large electric field range. In contrast the electron g-factor is not influenced by the electric field at all. Theory reproduces the hole g-factor dependence, which arises from a soft hole confining potential, an In concentration gradient and a strong dependence of the material parameters on the In concentration. The last chapter demonstrates the anisotropic behaviour of the hyperfine interaction between nuclear spins and the hole spin. In the experiment, again with the measurement method of coherent population trapping, a low-noise sample and resonance fluorescence spectroscopy are combined. The resulting high signal to noise ratio and the ultra narrow CPT dip enable the measurement of very precise values for the energy splitting of the hole spin states. This is leading to the main result: a minimal hole hyperfine interaction in an in-plane magnetic field, proofing a decoupling from the hole spin and the nuclear spins.

Contents

PART I

Introduction: Quantum dots, single hole spins and the experiment

Chapter 1

Introduction to quantum dots: Concept and experimental techniques

1.1 Quantum dots, holes, single hole spins and spin qubits

The introductory chapter's aim is to give an overview of the indium gallium arsenide (InGaAs) III-V semiconductor quantum dots (QDs), considering preferentially the carriers with positive charges, the holes. In the following some background information is provided and it is explained why and how single hole spins are advantageous candidates for spin qubits. The second part of the introduction gives a short overview of the basic parts of the experimental setup and measurement techniques. The chapter concludes with a description of four important experimental aspects, which are essential to the experiments presented in this thesis.

1.1.1 Motivation - Coherence

Self-assembled QDs are known for their outstanding optical properties. There has been a lot of excellent work in recent years, presenting the bright and narrow linewidth single photon emission of a QD. The exact single charge control of the QD and the access to their spin properties qualifies QDs for spintronic applications.

Their quantum nature yields QDs and their spins as ideal candidates for a quantum bit (qubit), a two level quantum system. Implementing a qubit routine of initialization, manipulation and read-out is essential for a potential application in quantum information processing or quantum communication. The two different spin states, up ($|\Uparrow\rangle$) and down ($|\Downarrow\rangle$), are the obvious choices for the qubit states. The information is encoded in the phase of the quantum mechanical superposition state, a condition in which the spin can be simultaneously in the up and down states. The qubit manipulation should then be conducted before this information is lost. The loss of the phase in the superposition state, known as decoherence, is due to interactions of the spin with the environment. Interactions for instance with lattice vibration

(phonons), other carriers or the nuclear spin bath. The challenge is the realisation of a highly coherent spin system by identifying the decoherence mechanisms and switching them off, if possible.

The most prominent candidate for a qubit is the electron spin in many ways [1]. In the area of solid state systems a single electron spin in a nitrogen-vacancy center in diamond shows long coherence times at room temperature in the millisecond range [2], or even up to 30 s in ultrapure ^{28}Si at low temperatures [3]. However, processing diamond into real devices is a challenge, because of the very hard material properties. And it is very challenging to achieve the kind of purified ^{28}Si required for the reported decoherence times. Spins in III-V semiconductors materials have considerable advantages. Apart from the confinement of single spins in an area of a few nanometers and a straightforward growth mechanism, the design possibilities of heterostructures and the nanofabrication technology are highly developed, leading to highly sophisticated devices. However, electron spins in these devices exhibit rather small coherence times in the microsecond regime and time averaged coherence times as low as a few nanoseconds [4].

The hole spin is a viable alternative: its interaction with the nuclear spin bath is different and therefore presumably longer coherence times are achievable. The ultimate goal of this thesis is to explore the boundaries of hole spin coherence in real QDs. The main tool is the quantum mechanical effect of coherent population trapping (CPT).

1.1.2 Quantum dots self-assembly and optical properties

Semiconductor QDs are formed via self-assembly in the heteroepitaxial growth of various semiconductors, such as InAs and GaAs. The Stranski-Krastanov (SK) growth mode is based on the strain induced by the lattice constant mismatch between the materials. The lattice constant of InAs is 7% larger than the one of GaAs. During the layer-by-layer growth process of InAs on GaAs by molecular beam epitaxy (MBE) the strain accumulates and after the thickness exceeds a certain threshold InAs QDs form. After the deposition of 1.5 monolayers of InAs, where the lattice adapts to GaAs, a partial relaxation of the strain eventually results in the formation of islands (the QDs) [5]. Fig. 1.1 shows a transmission electron microscopy image of an InAs QD. The height of the QDs is typically $\sim$ 7-8 nm with a lateral extent of $\sim$ 30 nm. The rest of the heterostructure is grown on top of a GaAs capping layer. The nucleation of the QDs is self-organized and they are positioned randomly over the sample. Special techniques enable site selected growth [6]. In total $\sim 10^5$ atoms form a QD.

The spatial confinement on the nanoscale has important consequences to the electronic properties of the system. The electronic properties of bulk semiconductor materials are described by a bandstructure diagram [7]. In Fig. 1.2(a) the band structure diagram of a confined di-

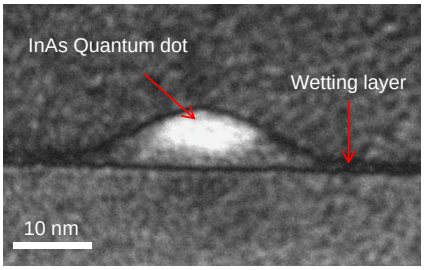

Figure 1.1 | Transmission electron microscopy image of a InAs QD with its wetting layer. (Image recorded by Jean-Michel Chauveau and Arne Ludwig)

rect semiconductor is presented. The confined periodic energy levels of the atoms merge into energy bands. The lowest unoccupied band (conduction band) and the highest occupied band (valence band) are separated by the band gap energy (E_g). The energy band gap difference in heterostructures, here between InAs and GaAs, shifts the bandstructure and creates a potential barrier, which determines the lowest valence and conduction band states for the free carriers in the low bandgap material (InAs). Based on an additional strong confinement in three dimensions, as it is the case for QDs, discrete and fully quantized energy levels emerge (Fig. 1.2(b)). The levels are energetically shifted with respect to the band gap energy of InAs by the additional confinement energy. The levels exhibit an energy separation of $\sim$ 20–50 meV in the conduction and $\sim$ 10–25 meV in the valence band.

The energy bands are drawn with respect to the crystal momentum k in the material and can be calculated by the k·p model [8]. The k·p model is based on the quantum mechanical perturbation theory and describes the conduction and the valence bands [9, 10] very accurately. The s-like conduction band is constructed from Bloch states (S,S_z = 1/2, $\pm$1/2) and resembles a parabola close to the point with the lowest energy. In contrast the valence band with p-like symmetry is six fold degenerate. The valence bands originate from the atomic p-states of the host material. The different effective masses and therefore different confinement energies as well as strain, lift the degeneracy of the heavy hole (HH) (J,J_z = 3/2, $\pm$3/2) and light hole (LH) (J,J_z = 3/2, $\pm$1/2) states by Δ_C. A large gap (Δ_{SO}) is formed by the spin-orbit interaction leading to the split-off (J,J_z = 1/2, $\pm$1/2) Bloch states.

In a semiconductor a hole is created in the highest valence band, when an electron is energetically excited into the lowest conduction band and is leaving a vacancy behind (Fig. 1.2). The concept of a hole is a virtual positively charged quasi-particle describing the absence of an electron. The Coulomb attraction between the two particles, caused by the spatial proximity in the QD, leads to the formation of an exciton (electron-hole pair). The exciton (X^0) will recombine by emitting a photon with the energy of the optical transition between the highest valence band and the lowest conduction band level [11]. An additional charge (hole or electron)

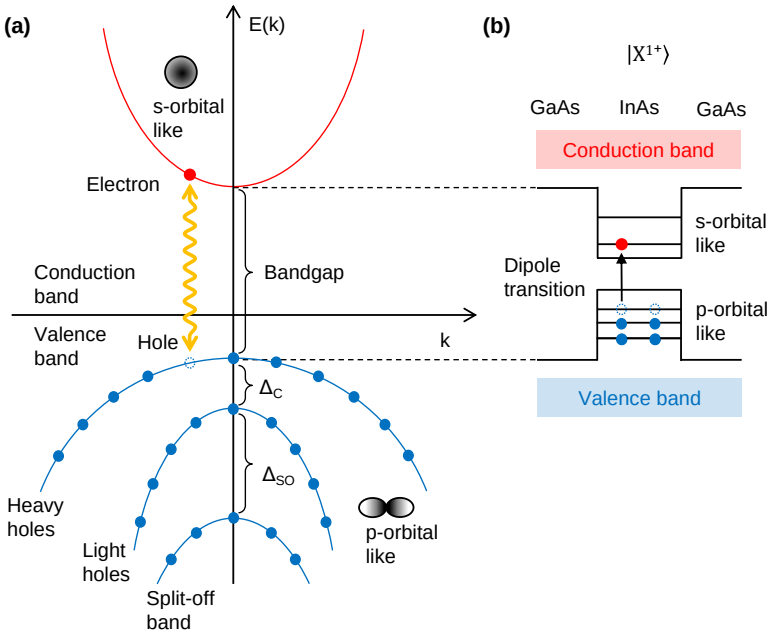

Figure 1.2 | (a) Band structure of a direct semiconductor. The energy of the electrons is shown as a function of the wave vector k. The conduction band states are formed from atomic s-orbital, the valence band states from p-orbitals. The energy band gap (E_g) of GaAs is 1.5 eV at low temperature. The degeneracy of the valence band states is primary lifted owing to the spin orbit interaction Δ_{SO}. Additionally confinement and strain Δ_C lifts the degeneracy between light and heavy hole states. For undoped materials at low temperature the valence bands are fully occupied and the conduction bands are empty, until an electron is energetically promoted into the conduction band, leaving a hole behind. (b) Energy level diagram of a self assembled QD. The confinement leads to discrete energy levels for the valence and conduction band. A strong optical dipole transition connects the energy levels of the valence and conduction states. Here the QD occupation of a optically excited state, the positively charged trion X^{1+} is illustrated.

forms the positively (X^{1+}) or negatively charged trion (X^{1-}). The three-dimensional confinement and the discrete energy levels in the QD render the notion of the k-vector redundant. The electrons and holes inside the QD behave similarly to a single real atom, opening the wide field of atomic physics to a solid-state environment.

The emission wavelength of the optical transition for as-grown QDs, the ones described so far, lies at low temperatures around ~ 1200 nm. This is very inconvenient in terms of excitation and detection wavelength. A post-growth process of rapid thermal annealing (RTA) diffuses GaAs into the InAs QDs, which reduces the In concentration and hence the confinement potential and leads to a blue-shifted emission wavelength [12].

A different approach is the In-flush technique [13]: After their formation the islands are capped only partially by GaAs (~ 2.4 nm). An increase in temperature to 600°C evaporates the uncapped indium partially. Now the flat QD is capped entirely by GaAs and embedded in a

semiconductor heterostructure. The In-flush process reduces the dimensions of the QD and shifts its emission energy to smaller wavelengths around 950 nm. The In composition inside the QD experiences usually a gradient from the bottom to the top [14].

The optical transition is the fundamental basis for the application of a self-assembled QD as a robust, fast and narrow-linewidth source of on-demand single photons. The high refractive index material GaAs (n = 3.5) compromises the outcoupling efficiency of photons from the devices. Ways to improve the efficiency are: the use of a hemispherical solid immersion lens (SIL) on top of the sample, leading to a enhancement of the outcoupled photons [15]; putting the QDs into a microcavity [16]; embedding the dots in an optical wave-guide, tapered towards the end, with outcoupling efficiencies up to 70% [17]. Experiments in the field of QDs are routinely carried out by non-resonant excitation of excitons in the high energy continuum states above the bandgap of GaAs. The electron and hole states in the QD are populated through fast relaxation and recombine under spontaneous emission of photons, the photoluminescence (PL). In contrast, coherent laser spectroscopy excites the QD with exactly the energy of the exciton transition. This technique establishes a coherent coupling of the driving laser with the single quantum dot. Driven resonantly, the quantum dot acts like a close-to-ideal two level system from atomic physics with a Lorentzian absorption lineshape [18], Mollow triplet [19], power broadening and power induced transparency [20], Rabi oscillations [19], dynamic Stark effect [21] and the antibunching of the resonance fluorescence (see e.g. Chapter 3).

In principle one could imagine the neutral exciton X^0 as a qubit. The excitonic state with one electron and one hole as state $|1\rangle$ and the empty dot as state $|0\rangle$. The large optical dipole of the QD allows quantum operations on the THz rate or even faster [22]. The experiments in terms of qubit initialization, manipulation and readout for excitons have been carried out in the ultrafast regime (time scale of a few ps) [23, 24]. The drawback with this scheme is the short exciton lifetime <1 ns [25], resembling a fast decoherence process. The short coherence time of the exciton makes single spins the more favourable candidates for qubits. It is shown, that this is especially true as the large optical dipole moment enables fast spin manipulation with optical techniques [26].

1.1.3 Single spins in semiconductor QDs

The first prerequisite for single spin qubits in QDs is the control and the trapping of one single carrier in the QD, either a single hole or electron. Three techniques place a single carrier in the QD: growing a doping layer nearby the QD layer and thus loading permanently an electron or hole in the QD [27, 28]; optical generation of the carriers [29, 30]; controlled tunnelling from a near by Fermi reservoir [31, 32]. In this work the third method is applied: the QDs are embedded in a particular heterostructure (sample designs are described later).

A voltage applied to the structure creates a electric field along the growth direction and tunes the energy levels of the QD relative to the Fermi energy. The number of carriers trapped inside the QD depends on the position of the conduction levels to the Fermi energy. The device works in the Coulomb blockade regime and the carriers experience a whole series of Coulomb interactions, which influence the total exciton emission energies. The Coulomb blockade model explains all interactions inside the QD [33]. For instance if one electron occupies the dot, it is not possible for a second electron to tunnel into the QD at the same voltage. First it has to overcome the Coulomb repulsion from the first electron. Clear steps in the QD emission spectrum reveal that the energy for a exciton follows the Coulomb blockade model [31]. The electric field allows a charging configuration to be chosen and a singly charged exciton to be addressed [34] (e.g. the positively charged exciton X^{1+} in Chapter 4, Fig. 4.2). Tunnelling is suppressed in the Coulomb blockade regime, but a second order spin flip process, the co-tunnelling, is allowed [35]. An additional result of the electric field is the dc-Stark effect. The electric field alters the separation between electron and hole wave function in the QD, which modifies the transition energy. The energy dependency derives from perturbation theory and is in good approximation quadratic in the electric field[36].

The second step for the creation of a spin qubit is the access to the individual spin energy levels, which are degenerate at zero magnetic field. An external magnetic field interacts with the magnetic moment of the electron or hole, resulting in a potential energy change by $-\boldsymbol{\mu B}$. The magnetic moment can be described in terms of the total angular momentum $\boldsymbol{\mu_j} = -\hat{g}_j \boldsymbol{\sigma_j} \mu_B$. μ_B is the Bohr magneton, $\boldsymbol{\sigma_j}$ the spin Pauli matrix and $\hat{g}_j$ the particular g-factor tensor of carrier j [37, 38]. The total splitting is dependent on the magnetic field direction. In growth direction (Faraday geometry) the electron and hole Zeemann splittings are $Z_e = g_e \mu_B B_z$ and $Z_h = g_h \mu_B B_z$, respectively. A pseudo spin of $\pm 1/2$ is assigned to the hole spin here.

Now all building blocks are available to describe the individual spin systems and merge into the spin level diagram in Fig. 1.3. The degeneracy of the heavy and light hole valence band states is lifted (Fig. 1.2) through the uniaxial strain and the strong vertical confinement. This implies the valence band ground state is dominated by a heavy hole contribution. Atomistic calculation support this picture [39]. The pure heavy hole states are J,$J_z = 3/2, \pm 3/2$ in the valence electron basis and $|\Uparrow\rangle$, $|\Downarrow\rangle$ in the hole basis [9]:

$$\begin{aligned} \left|\frac{3}{2}, +\frac{3}{2}\right\rangle &= \frac{1}{\sqrt{2}} \left|(p_x + ip_y)\uparrow\right\rangle \equiv |\Downarrow\rangle \\ \left|\frac{3}{2}, -\frac{3}{2}\right\rangle &= \frac{1}{\sqrt{2}} \left|(p_x - ip_y)\downarrow\right\rangle \equiv |\Uparrow\rangle \end{aligned} \tag{1.1}$$

p_x and p_y are the p-orbitals in the plane. $|\uparrow\rangle$ and $|\downarrow\rangle$ represent the electron states in the valence band. The optical selection rules are rather strict an depend on the direction of the external

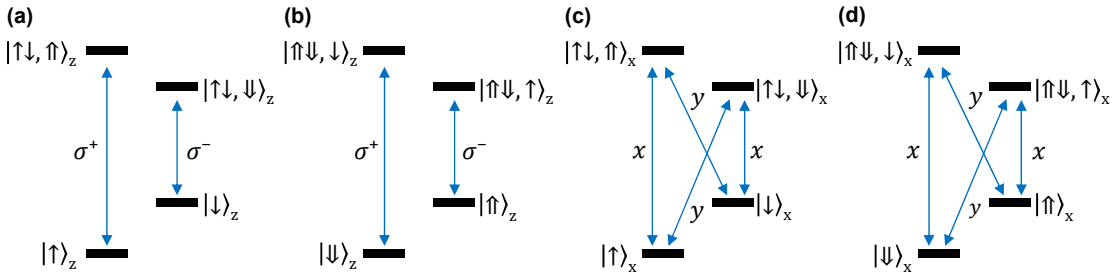

Figure 1.3 | (a) and (b). Single spin level diagrams for electron $|\uparrow\rangle_z$ and $|\downarrow\rangle_z$ (hole,$|\Uparrow\rangle_z$ and $|\Downarrow\rangle_z$) spin states in an external magnetic field $\boldsymbol{B}$ along the growth direction (z). The charged trion states X^{1-} (X^{1+}) are formed out of two spin-paired electrons (holes) and one hole (electron). The allowed transitions under conservation of the angular momentum (blue), are right (σ^+)- and left (σ^-)-handed polarized. (c) and (d). Level diagram for electron (hole) states with a magnetic field in-plane along the x-direction. Here all transitions are allowed with linear polarized light in x- and y-direction.

magnetic field [40]. The selection rules for the magnetic field in growth direction (z) and a pure heavy hole spin, Fig. 1.3(b), are

$$\begin{aligned} |\Downarrow\rangle_z &\xleftrightarrow{\sigma^+} |\Uparrow\Downarrow,\downarrow\rangle_z \\ |\Uparrow\rangle_z &\xleftrightarrow{\sigma^-} |\Uparrow\Downarrow,\uparrow\rangle_z \end{aligned} \tag{1.2}$$

The transition is allowed under conservation of the spin angular momentum, depended on the photon polarization σ^+ $(+1)$ and σ^- (-1). A laser with circular polarized light can only drive the vertical transitions. Fig. 1.3(a) represents the electron spin case. The diagonal transitions are have no spin conservation and are forbidden. The constraint on the diagonal transitions is only partially lifted in case of a light hole admixture [41].

An in plane magnetic field modifies the level diagram. The new spin eigenstates in the x-basis are a linear combination of the spin states in z:

$$\begin{aligned} |\Downarrow\rangle_x &= \frac{1}{\sqrt{2}}(|\Downarrow\rangle_z - |\Uparrow\rangle_z) \\ |\Uparrow\rangle_x &= \frac{1}{\sqrt{2}}(|\Downarrow\rangle_z + |\Uparrow\rangle_z) \end{aligned} \tag{1.3}$$

With the new spin states in x-basis and the selection rules from the z-basis applied, all four transitions are equally allowed. Fig. 1.3(c) for electron and (d) for hole spins show the new level diagram with the allowed transitions. A linear y-polarized laser couples to the "diagonal" and a x-polarized laser to the "vertical" transitions of the new level diagram.

1.1.4 The electron spin and the problem of decoherence

The individual hole $|\Uparrow\rangle$ and $|\Downarrow\rangle$ or electron $|\uparrow\rangle$ and $|\downarrow\rangle$ states can be seen as a spin qubit. The in-plane configuration enables individual control of the spin qubit states, if the spin states are sufficiently separated. Coupling both spin ground states to a common upper state by two lasers, establishes a Λ system [42] used for coherent population trapping experiments [43, 44].

The main limitation for the perfect electron spin qubit in a QD is the lack of spin coherence. Three timescales are of interest in this context. First the spin relaxation time T_1, which is the time of a spin-flip process ($|\uparrow\rangle \rightarrow |\downarrow\rangle$) resulting of interactions with the environment, such as the lattice. For electron spins this time is very promising as experiments state $T_1 > 20$ ms [30] and even predict times up to $T_1 = 1$ s [45]. (For lateral QDs defined from a two-dimensional electron gas relaxation times of $T_1 > 1$ s [46] have been observed.) Second, the decoherence time of the quantum system T_2, which describes the life time of a quantum mechanical superposition of spin up and spin down states ($|\uparrow\rangle + |\downarrow\rangle$). This time is surprisingly small $T_2 = 3$ µs [4, 27]. And finally the decoherence time for an ensemble measurement, the time averaged coherence, called the dephasing time T_2^*. This decay time includes the all statistically distributed noise contributions over several experiments and turns out to be in the order of just a few nanoseconds $T_2^* \simeq 1 - 10$ ns [4, 27, 43]. The three timescales are related to some extent. The decoherence time can be generally expressed as [47, 48]

$$\frac{1}{T_2} = \frac{1}{2T_1} + \frac{1}{T_\phi}. \tag{1.4}$$

T_ϕ is the dephasing contribution to the decoherence rate, which contains the pure dephasing mechanisms of the single spin. T_1 is limited by phonons. The ideal limit of decoherence for electrons and holes, $T_2 = 2T_1$ [47, 49], can only be reached if noise induced by phonons is dominant and T_ϕ is minimal. The relation between the decay times in case the hyperfine coupling of the nuclear spins prevails is $T_2 \leqslant 2T_1$, but usually $T_2^* < T_2$ and $T_2 \ll T_1$.

The two dominant decay channels for spin qubits in QDs are the spin orbit interaction (SOI) and the hyperfine interaction [50]:

Different types of asymmetry in the system lead to Rashba SOI, which couples the electric field to the spin states, and Dresselhaus SOI terms [8]. The Dresselhaus term (bulk inversion asymmetry) depends strongly on the growth direction and can cancel in certain directions with the Rashba term (structural inversion asymmetry) in the lowest order [51]. The SOI terms drive mainly the spin relaxation by a phonon-mediated mechanism, all other effects are negligible [52, 53]. For electrons at high magnetic fields the influence of the phonons dominate the T_1 relaxation with a B^{-5}-dependence [30]. At low temperatures the spin relaxation via phonons is mostly suppressed.

The theoretical limit, $T_2 = 2T_1$ [47], is achievable if the decoherence is only limited by phonons. The hyperfine interaction is the main source of decoherence [54, 55] and the reason for the experimentally achieved poor $T_2 \ll T_1$. As a result of the approximately $10^4 - 10^6$ atoms in a QD, the electron wavefunction overlaps with a large number of atoms. Each atom contains a non-zero nuclear spin contributing to the hyperfine interaction. Three different components of the hyperfine interaction can be derived from the Dirac equation [56]: the isotropic contact hyperfine interaction H_c; the anisotropic hyperfine interaction (dipole-dipole like) H_{dd}; and the coupling of orbital angular momentum to the nuclear spin H_{ang}. For electrons the contact hyperfine interaction is the predominant coupling to the nuclear spin bath, while the other components are negligible, due to their spherical symmetry and their vanishing orbital momentum. The contact hyperfine interaction is:

$$H_c \approx \sum_i A_i^e \mid \psi_i \mid^2 \boldsymbol{I}_i \cdot \boldsymbol{S} \equiv \mu_B \hat{g}_e \boldsymbol{B}_N \cdot \boldsymbol{S} \tag{1.5}$$

with A_i^e the coupling coefficient with nuclear spin i, $\boldsymbol{I}_i$ the nuclear spin vector, ψ_i the electron envelope function, $\boldsymbol{S}$ the electron spin and the electron g-factor tensor $\hat{g}_e$. A_i^e is dependent on the individual isotopes and typically around 100 µeV for In, Ga and As [57]. The conduction band wavefunction consists of atomic s-orbitals (see Fig. 1.2) and exhibits therefore a large amplitude at each individual nuclei, Fig. 1.4(a). Each nuclear spin interacts with the electron via an effective magnetic field. In principle the effective magnetic field for N nuclear spins balances itself out, just a residual factor of $1/\sqrt{N}$ remains [54]. The Overhauser field, the remaining effective magnetic field, for InAs QDs is around $B_N \approx 20$ mT [58]. The fluctuating Overhauser field leads to dephasing. The part of B_N fluctuating perpendicular to the applied magnetic field in z-direction, is responsible for the electron spin flip-flop process. In terms of the relaxation time T_1 at zero and very low magnetic fields (below 0.3 T) the flip-flop processes result in very small relaxation times. As soon as a magnetic field lifts the degeneracy of the spin states this process is suppressed and large T_1 times can be achieved. In contrast the other part of B_N fluctuating along the applied field, e.g. in z-direction, results in random changes in the electron precession frequency and therefore in large dephasing and a small T_2^* ($\boldsymbol{B_{tot}} = \boldsymbol{B} + \boldsymbol{B_N}$). The changes in the precession frequency are proportional to the Zeeman splitting of the electron spin levels by the Overhauser field ($g_e \mu_B B_N$). Therefore the dephasing time T_2^* is connected to the Zeeman splitting ($T_2^* \propto \hbar/\Delta Z_e^{nu} \sim 1$ ns). The electron g-factor is $g_e \simeq -0.5$ for the usual QDs [59].

Attempts to prolong the dephasing time have been made, including optical polarization of the nuclei with a dynamic nuclear polarization scheme (DNP) [60] or feedback control to narrow the distribution of the nuclear spin ensemble around a mean value B_N^{max} [61]. Although the

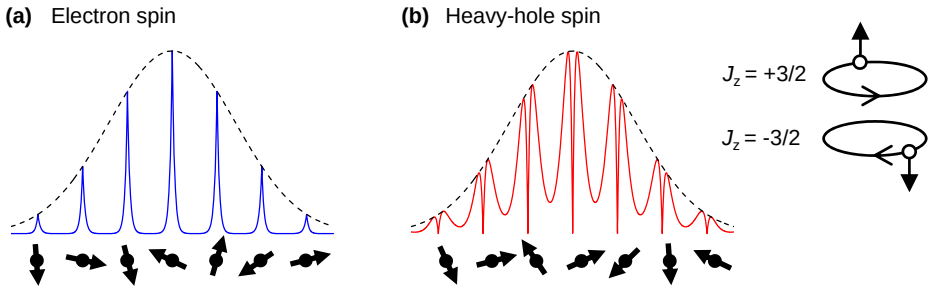

Figure 1.4 | (a) Atomic s-orbitals build the electron conduction band states (blue), each localized to a nucleus (black circle with spin) and modulated by an envelope function (black dashed line). (b) The valence band hole states are predominantly constructed from atomic p-orbitals (red), with a minimal amplitude at the position of each nucleus. The magnetic dipole moment of the heavy hole spin is illustrated by a circulating microscopic current and points in spin direction. In +z-direction for a clockwise rotation with spin up and in −z-direction for anticlockwise and spin down.

polarization of the nuclear spin is only partially (50–70%) achieved, the dephasing time can be extended to $T_2^* \geq 0.1$ µs [62].

Despite the decoherence the qubit routine is fully implemented for an electron spin: Initialization with close to 100% fidelity by optical spin pumping (OSP) [63, 64], manipulation with fast laser pulses [65] or alternating magnetic fields [66], and subsequent read-out [4, 65].

1.1.5 The hole spin

An interesting alternative for a spin qubit represents the hole spin. The big advantage is the coherence of the hole spin as reported by Brunner *et al.* [44]. A prominent reason for the coherence of holes is the difference in hyperfine interaction compared to electrons [67, 68]. Recently, similar experiments as the ones for electron spins have been realized for the hole spin to achieve the spin qubit routine: initialization [29, 69], manipulation [70–72] and read-out [73].

Phonon-mediated spin relaxation for a hole spin is comparable to the one of electrons in a strongly confined environment [49]. The sensitivity to confinement leads to long relaxation times $T_1 > 0.5$ ms [69] for low magnetic fields. The hole spin experiences a T^{-1} and magnetic field dependence, pointing towards phonon related decay mechanisms [74]. A weak magnetic field dependence is predicted to arise from two phonon processes in the limit $B \to 0$ [75]. If only pure phonon related decoherence is present the upper limit for holes, $T_2 = 2T_1$, can be theoretically achieved [49].

For holes, similar to electrons, the hyperfine induced dephasing is claimed to be a prominent

decoherence mechanism at low temperatures. The hole states are constructed from atomic p-orbitals, Fig. 1.2, with one p-orbital per atom. The hole wavefunctions have a vanishing amplitude at the location of each nucleus, see Fig. 1.4(b), such that the contact hyperfine interaction H_c is switched off. For holes with a p-type symmetry of the wavefunction the dipole part of the interaction is significantly enhanced with respect to an electron spin. The dipole part is the combined anisotropic hyperfine interaction H_{dd} and the coupling of orbital angular momentum to the nuclear spin H_{ang}. Confined systems, with a large HH-LH splitting, have approximately pure HH states in the valence band. For a pure HH, with a magnetic dipole moment along the z-direction and inside an unstrained QD, the effective dipole hyperfine interaction Hamiltonian of H_{dd} and H_{ang} takes a simple Ising form (only one direction of spin component possible) [67]

$$H_{dipole}^{HH} \approx \sum_i A_i^{h,z} \mid \psi_i \mid^2 I_i^z \cdot J^z \equiv \mu_B \hat{g}_h B_N^h J^z. \tag{1.6}$$

Here is A_i^h the coupling coefficient of HH to the nuclear spin i, I_z is the z-component of the nuclear spin, ψ_i is the hole envelope function, J_z is the z-component of the hole spin vector and $\hat{g}_h$ the hole g-factor tensor. $A_i^{h,z}$ is typically around 10 µeV (-10% of A_i^e) [76, 77]. This anisotropy of the Overhauser field opens great possibilities for hole spins ($\boldsymbol{B_{tot}} = \boldsymbol{B} + zB_N^h$). The heavy hole only experiences a fluctuating Overhauser field in z-direction, which leads to dephasing if no magnetic field or a field in z-direction is applied [67]. However for a strong in-plane magnetic field the fluctuations in z-direction have a negligible influence on the total magnetic field. The strongly suppressed magnetic field fluctuations imply a highly coherent heavy hole spin. The dephasing T_2^* time should rise despite a noisy Overhauser field with an applied in-plane magnetic field [78]. Basically the amount of the fluctuating Zeeman energy leading to fast dephasing of the spin precession is very small, therefore T_2^* should increase ($T_2^* \propto \hbar/\Delta Z_h^{\perp,nu}$). First experiments on InAs QDs support the claim of long decoherence and dephasing times in an in-plane magnetic field: $T_2 = 1$ µs [44, 70] and $T_2^* = 0.1$ µs [44].
These predictions hold only for a pure heavy hole state. In reality the valence band ground state is an admixture of heavy hole, light hole and the spin orbit contributions. That includes components of the p_z-orbitals to form the hole states, giving rise to non vanishing contributions to the hyperfine interaction Hamiltonian [79]. It is therefore still unclear to which extent the non-HH component in real QDs influences the coherence of the hole spins in InGaAs QDs. The extended interaction Hamiltonian for the real hole spin is

$$H_{dipole} \approx \sum_i \mid \psi_i \mid^2 (A_i^{h,z} I_i^z \cdot J^z + A_i^{h,y} I_i^y \cdot J^y + A_i^{h,x} I_i^x \cdot J^x) + \cdots . \tag{1.7}$$

The effective hyperfine Hamiltonian includes the ladder operators $J^{\pm} = J^x \pm iJ^y$ for the hole spins, $I_i^{\pm} = I_i^x \pm iI_i^y$ for the nuclear spins and the non-collinear contributions. It can be written as [79]

$$H_{dipole} \approx \sum_i \mid \psi_i \mid^2 (A_i^{h,z} I_i^z \cdot J^z + \frac{1}{2} A_i^{h,\perp} (I_i^+ \cdot J^- + I_i^- \cdot J^+) + A_i^{h,nc} (I_i^+ \cdot J^z + I_i^- \cdot J^z)) + \cdots . \quad (1.8)$$

The hyperfine coupling coefficient for the transverse part is $A_i^{h,\perp}$ and for the non-collinear fraction $A_i^{h,nc}$.

The goal of the thesis is to explore the boundaries of hole spin coherence in real QDs, basically mapping the contribution of additional terms to the hole hyperfine interaction. The main tool is the quantum mechanical phenomenon of coherent population trapping (CPT) which is introduced in Chapter 2. The first experiments (Chapter 2) suffer from material issues, noise in the sample and a bad signal-to-noise ratio in the experiment. The issues are addressed one by one in this thesis. Finally the CPT effect is a highly sensitive and ultra-precise measurement method, which enables the probing of the magnitude of the in-plane hole hyperfine interaction coefficients in real QDs (Chapter 7).

1.2 Experimental overview

The second part of the introductory chapter lists the techniques which are used in the QD and hole spin experiments. After a short overview of the basic components of the experiment, the main improvements on the sample and on the spectroscopy setup are described in detail. Only these details made it possible to collect the high quality data presented in this thesis.

All experiments were carried out in a cryogenic environment at 4.2 K in a liquid helium bath cryostat (CryoVac). Superconducting magnets create magnetic fields up to 9 T in growth direction (Cryomagnetics) or up to 3 T in-plane with a split-coil magnet (American Magnetics). A photodiode underneath the sample enables the technique of differential transmission spectroscopy [18, 80] exploiting a Stark-shift modulation technique with lock-in detection. Here the interference between the laser field and the field of the coherently scattered photons is measured [81]. The optical detection follows the principle of a conventional confocal microscope [82], with a single mode fibre acting as a pinhole [83]. In detail the microscope consists of two parts, the microscope head outside and the microscope tube inside the cryostat (see Fig. 1.5). The microscope head is designed for standard photoluminescence spectroscopy (PL) as well as for coherent laser spectroscopy of the resonance fluorescence (RF) of the QDs. The microscope tube contains a cage system with all electrical connections and a free space optical passage for the light. On top a window with a anti-reflection coating seals the tube. At the

bottom of the tube, the QD sample is placed on top of a stack of x-y-z piezo positioners and a x-y piezo scanner (attocube). The piezo positioners enable sub-nm precision in moving even at cryogenic temperatures around 4 K and high magnetic field. This is essential for addressing and selecting individual QDs. A hemispherical SIL on top of the sample enhances the outcoupled QD emission signal. Instruments for detection of the emitted photons are a grating based Spectrometer with a CCD camera (40 µeV resolution, Princeton Instruments) or single photon avalanche photo diodes (APDs, PicoQuant).

1.2.1 Sample design

A huge impact on the optical properties of the QDs originates from the sample design and the growth process. High quality and low-noise samples are very difficult to achieve. For n-doped devices with electrons as carriers, QDs showing narrow linewidth transitions and low-noise environments are realised by increasing the capping layer [84, 85]. In Chapter 5 we present transform limited linewidth for neutral and charged excitons in n-doped devices. The first generation of samples was provided by the University of California in Santa Barbara (UCSB), the second generation with lower noise by the Ruhr-University of Bochum.

More challenging is the realization of data with comparable performance for p-doped devices employing holes as carriers. Samples with Be as a dopant exhibit coupling to the continuum states (Fano resonances) [86]. Hence C-doping is the favourable doping method. The linewidths presented so far are at best three times larger than for n-type devices ($\sim$ 5 µeV) [44, 86] and the emission count rate ten times smaller. An inverted sample design is introduced and characterized in detail in Chapter 4. The main advantage is the growth of the p-doped layer at the end of the fabrication process. Therefore the contamination of the environment, which occurs usually after the p-doping, doesn't affect the QDs at all. That makes the smallest linewidths seen so far possible, down to the transform limit.

1.2.2 Resonance fluorescence spectroscopy

The main advantage of experiments presented in this work is the ability to perform coherent laser spectroscopy and detect the resonance fluorescence of the QD. This paves the way for high resolution measurements including a high signal to noise ratio. The coherent laser drives the QD with the exact frequency of the energy transition and the exciton recombines by emitting a photon with the same energy. The experimental challenge is the separation of the scattered laser light from the QD emission. One way is to excite the QD in-plane and detect the emission out of plane, in growth direction [19, 88]. Our scheme instead takes advantage of one inherent property of the light: the polarization. The design of the microscope head is based on a dark-field concept. Crossed linear polarization for the excitation and the detection (s and p)

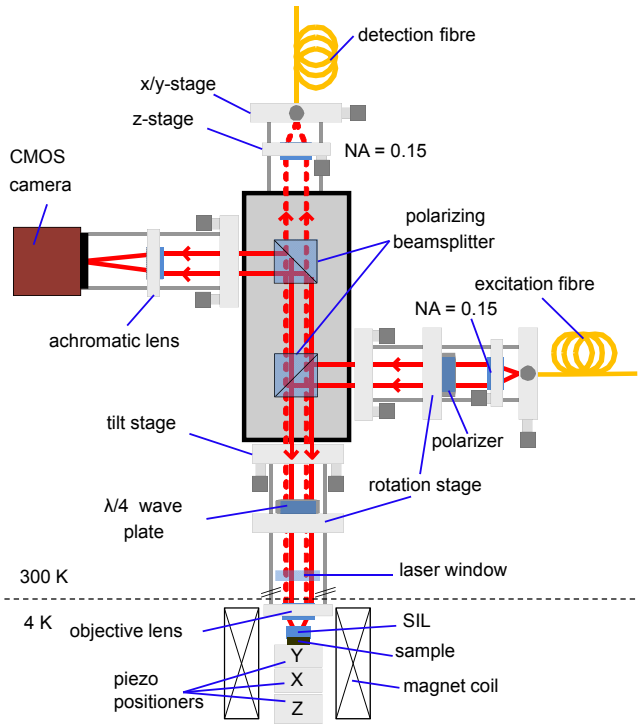

Figure 1.5 | Schematic of the microscope system. The sample on a stack of piezo positioners is located inside the cryostat. The microscope head remains at room temperature. The sealed laser window provides optical access. The microscope head consists of a center part with two polarizing beam splitters (PBS) and the horizontal excitation and vertical detection arm. The upper horizontal arm images the sample surface with a camera. Optical fibres connect the head to the lasers and detectors. The dark-field concept is realized by orthogonal polarization states of the excitation and collection: the linear polariser defines the laser polarization to s, matching the lower PBS; the quarter-wave plate controls the state of polarization; and the PBSs blocks the s-polarized back-reflected laser light. s-polarization is depicted by solid lines and the p-polarization by the dashed lines. Schematic adapted from Ref. [87].

leads to a suppression of the laser light in the detection arm of the microscope head. This is realised by two polarizing beam splitters (PBS), one linear polariser and a quarter-wave plate. The linear polariser defines the polarization of the incoming laser light, e.g. to s-polarization. The first PBS deflects the s-polarized light by 90° to the QD device. The quarter-wave plate corrects for an induced ellipticity. Backscattered s-polarized laser light is only reflected by 90° and not transmitted into the detection arm when passing the first and second PBS. Only the p-polarized emission from the QD gets transmitted and can be detected. A detailed description of the dark-field microscope head is shown in Fig. 1.5 and can be found in Ref. [87].

The striking performance features are: the long term stability over several days, a suppression of the excitation laser up to 8 orders of magnitude and a standard signal-to-background ratio of more than 10^4:1.

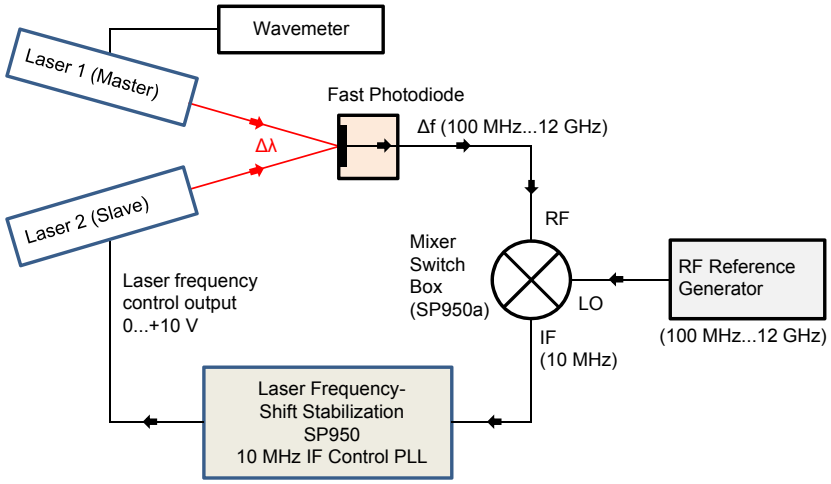

Figure 1.6 | Schematic of the laser frequency locking principle. The frequency of the slave laser 2 is locked with a stabilization loop to the master laser 1 at a fixed frequency difference Δf. Signal down-mixing with the help of a reference source enables low frequency operation around 10 MHz.

1.2.3 Laser frequency locking

Spectroscopy measurements of the coherent population trapping mechanism include two lasers and depend strongly on the mutual tuning of the two lasers with respect to each other. The frequency offset stabilization technique for single spins in QDs requires a large tunability and great flexibility. The transitions energies of the self-assembled QDs are located in a range of ± 40 nm (54 µeV, $\pm 10^{13}$ Hz). The Zeeman splitting of single spins can vary dependent on the QD and the magnetic field direction from sub 1 GHz/Tesla up to 12 GHz/Tesla. The locking scheme is designed to satisfy these requirements. (RF usually stands for resonance fluorescence, only from here until the end of the first Chapter RF corresponds to radio-frequency (3 kHz - 300 GHz).)

1.2.3.1 Principle

The working principle of the laser locking scheme fixes the laser frequency of a slave laser relative to the one of a master laser. This enables a fixed frequency difference (beat frequency: $\Delta f = f_1 - f_2$) at all times. The setup for the pump-probe locking scheme is shown in Fig. 1.6.

A small amount of the emission of both lasers (DLPro 940, Toptica) is combined via two arms of a multimode fibre. The master laser is frequency stabilized by the control software of the wavemeter (High Finnesse WS/U-30U). The beat signal is then detected with a fast photodiode (New Focus, 1554-A-50 with bandwidth up to 12 GHz). A beat frequency (Δf) proportional to $\Delta\lambda$ of the lasers can vary from 100 MHz up to 15 GHz.

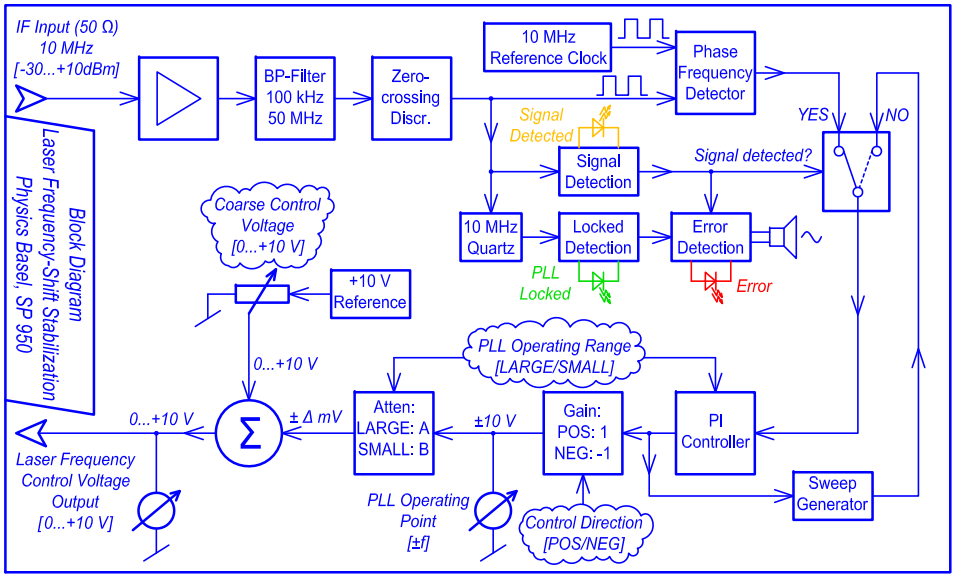

Figure 1.7 | Block diagram of the laser frequency locking electronics SP950 (Electronics Workshop Uni Basel)

The crucial idea is the downmixing of the RF signal with the help of a mixer and a RF reference generator (FSW-0020, Phasematrix). That is realised down to an output signal with the intermediate frequency (IF) of 10 MHz. Consequently the whole stabilization electronics can be operated with relatively small MHz components around 10 MHz and no wide bandwidth and GHz electronics is needed. However there is no single mixer to cover the large frequency range, therefore an additional switching system with two mixers (300 MHz to 4.3 GHz ZEM-4300 MH+, MiniCircuits and 3.2 GHz to 15 GHz, ZX05-153MH+, MiniCircuits) is implemented. The IF is fed to the Laser Frequency-Shift Stabilization (SP 950, Electronics Workshop Uni Basel), which provides the correcting voltage between 0 and 10 V to the piezo controller of the slave laser. Any deviation from the target beat frequency will be corrected and locked to 10 MHz.

1.2.3.2 Electronics

The laser frequency-shift stabilization electronics (SP 950, Electronics Workshop Uni Basel) can be understood as a phase locked loop (PLL) with an external voltage controlled oscillator (VCO) in form of the laser system. The PLL tries to stabilize the frequency from the mixer (input signal) to exactly the value of an internal clock of 10 MHz. Fig. 1.7 depicts the schematic of the SP950.

Three main features are implemented in the scheme: a sweep function, an error detection and the control direction of the stabilization circuit. The sweep generator scans the entire

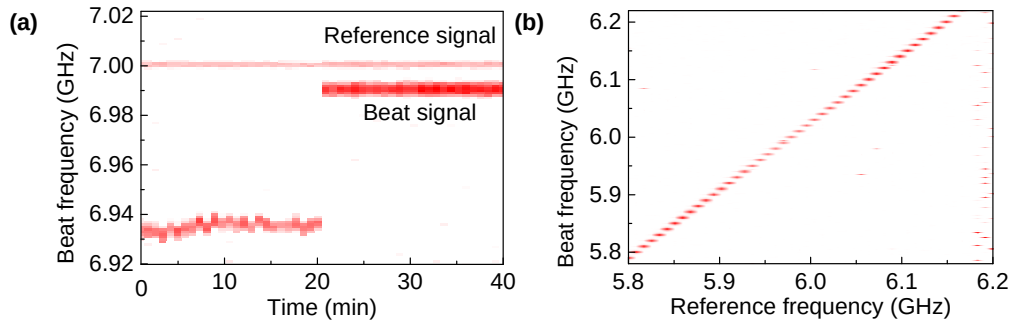

Figure 1.8 | Examples of the locking performance: (a) The frequency locking characteristics of the system. As soon as the locking electronics is switched on the beat signal of the two lasers is locked the reference signal. The locking results in a 10 MHz offset induced by the mixer. (b) Tuning characteristics of the system. The reference laser frequency is increased in 10 MHz steps and the beat frequency stays always locked with a 10 MHz offset.

capture range (200 MHz, or 2 GHz) in the case no input signal is detected. The mixer output is dependent on the beat signal of the lasers and can vary between 100 kHz and 50 MHz. An additional potentiometer changes the control voltage until a signal detection occurs. Then the normal PLL scheme is applied. If no detection or no locking is possible the error detection LED starts blinking and an acoustic signal is triggered. That happens as well in the case the locking is lost (e.g. a laser mode hop). The last feature is the detection direction. The 10 MHz offset between the beat frequency of the lasers and the reference frequency of the RF generator, induced by the mixer, is in principle direction independent. A negative or positive control function locks the output frequency 10 MHz above or below the reference frequency dependent on the actual wavelength.

1.2.3.3 Performance

The tests and analysis of the performance of the stabilization electronics are illustrated for exemplary frequency ranges in Fig. 1.8. A spectrum analyser collects the beat frequency and the reference frequency over time and for statistical measurements. The influence of the PLL electronics is clearly visible, when switched on at minute 20. The signals are perfectly locked, the FWHM of the beat frequency linewidth is only 1 MHz and the temporal drifts are eliminated. The linewidth is below the 10 MHz expected for the CPT dip and enables therefore high resolution and accurate measurements. The capture range for frequency locking stretches up to 2 GHz.

The second test (Fig. 1.8(b)) illustrates the locking performance as required during the experiment. One laser is tuned and the frequency difference to the second one is always defined. That can be implemented via tuning of the reference frequency and it is tested if the

beat frequency is and stays locked after each step. The sweep function enables locking under tuning conditions over the whole frequency span from 100 MHz up to 15 GHz.

The locking scheme is especially important if long integration times (>5 s per data point) give rise to temporal drifts and therefore broadening of the beat frequency linewidth. For the CPT measurements in Chapter 7 the technique was not used in the end, due to high count rates and the possibility to work with very short integration times per step. A second reason is the high quality and temporal stability of the lasers compared to the one used in the first experiments in Chapter 2.

1.2.4 AOM setup

The next sensitive condition of the experiment to be met by the excitation laser is the exact control of the intensity, even when scanning the laser frequency. Additionally the long-term fluctuations of the laser power have to be minimized, in order to enable high quality scans. A setup including an acousto-optic modulator (AOM) as centrepiece is designed in double passage geometry to suit the experimental needs of the measurements.

1.2.4.1 Principle

AOMs are able to modulate the frequency, intensity and direction of the laser beam, properties which can be used for e.g. spectral tunable filters [89] or laser cooling and trapping experiments [90]. The AOM (AOM 3200-1117, Crystal Technologies) contains a TeO_2 crystal connected to a strain transducer. A RF signal applied to the transducer causes an acoustic wave to build up inside the crystal, propagating at the speed of sound. The crystal with the acoustic wavefront acts like a diffraction grating to the incoming laser beam. The laser light is scattered when meeting the acoustic wavefront, a behaviour that can be approximated by Bragg diffraction. Maximum diffraction efficiency in the first order peak is determined by the Bragg angle condition:

$$\sin\theta_B = \lambda_1/2\lambda_s \tag{1.9}$$

with the Bragg angle θ_B, the laser wavelength of the first order λ_1 and the wavelength of the sound-wave λ_s. An obstacle implementing the AOM in the experiment is the dependency of the diffraction angle to the input or modulation frequency. In the experiments single mode fibres are used to couple the laser light in and out of the AOM setup. Wavelength tuning in a single pass geometry would cause the output coupling efficiency to vanish. A double pass configuration [91] eliminates that problem. Here the second pass compensates for the change in the diffraction angle and different laser wavelengths cause no displacement at the output. The double pass configuration is illustrated in Fig. 1.9. The polarization is indicated in green

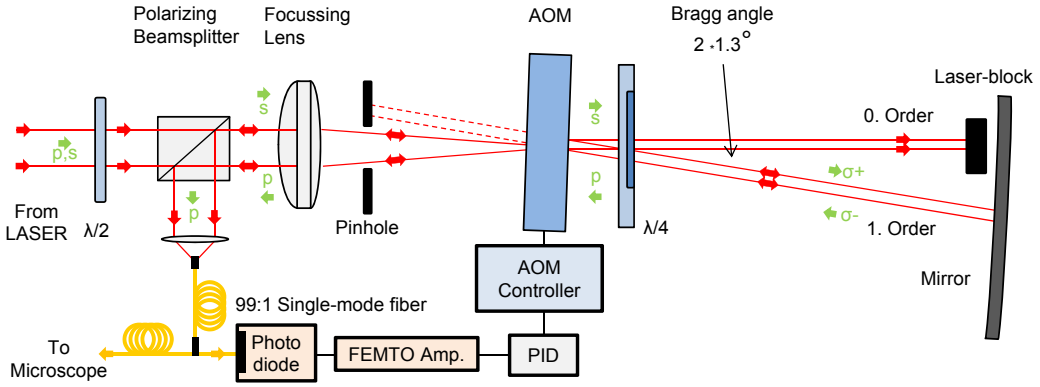

Figure 1.9 | Double pass configuration of the AOM setup with feedback loop. The arrows indicate the direction of the laser light (red) and of the particular polarisation (green).

and the laser light in red. A half-wave plate and a polarizing beam-splitter filter the laser beam such that only one linear polarization (s) is focused on the AOM and the other popularization (p) is blocked. The quarter-wave plate changes the linear polarization to circular after the AOM. A concave mirror acts as a cat's eye retro-reflector and focuses the intensity of the first order beam directly back to the AOM, independent from the spatial position on the mirror. The undiffracted zeroth order is eliminated by a beam block. The circular polarization of the reflected light is now counter clockwise due to a phase shift of 180° at the mirror. The reflected first order beam overlaps with the incident beam with a 90° difference in linear polarization (p) and is therefore reflected from the polarizing beam splitter into the single mode fibre.

The AOM, mounted on a fully movable x-z stage on top of a rotation mount, can be operated in two modes, the frequency and the amplitude modulation mode. The frequency modulation allows tuning of the laser output frequency during constant laser input frequency, maintaining a stable output in terms of intensity. The amplitude modulation regulates the amount of laser light diffracted into the first order. This mode enables the creation of short laser pulses as well as a intensity stabilized output over a large range of frequencies and a long-term stability with the help of a feedback loop. The feedback loop consists of a photo-diode as detector, a current amplifier and a PID (proportional, integral, derivative) stabilization electronics, which is connected to the RF frequency controller of the AOM. The stabilization loop readjusts the RF amplitude modulation of the AOM, while keeping the previously set output intensity.

1.2.4.2 Characteristics of the double passage AOM setup

The AOM setup in double pass geometry was built twice in order to stabilize both lasers in the experiment. A transmission photodiode beneath the sample collects the amount of

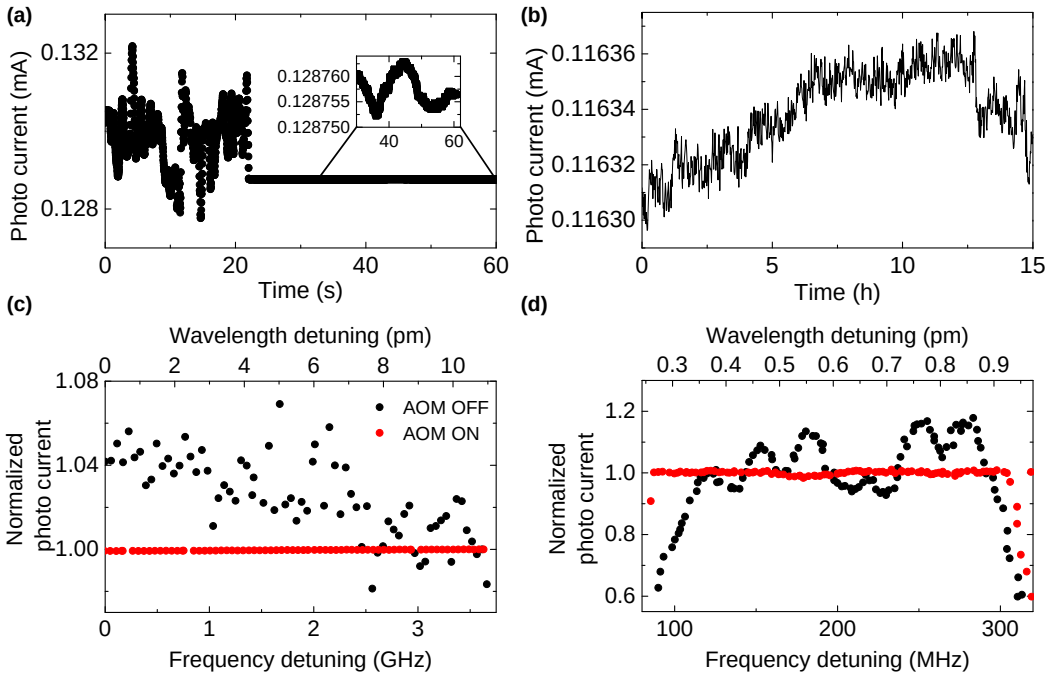

Figure 1.10 | Characteristics of the AOM setup. (a) The fluctuation of the laser intensity at the QD, without and with AOM switched on. The inset zooms into the measurement during stabilization and reveals a fluctuation suppression of more than 2 orders of magnitude. The data was recorded in transmission by a photo-diode beneath the sample. (b) illustrates the long-term stability of the AOM setup over 15h. Normalized intensity while changing the frequency of the laser (c) or tuning the frequency by the AOM frequency modulation option over a small range (d). The red data shows the result of the feedback stabilization.

coherent scattered laser light and gives a hint of the laser intensity seen by the QDs. The characteristics of the setup are tested regarding long-term stability and intensity stabilization while frequency tuning. Furthermore the AOM acts as a "noise eater" suppressing an applied square wave signal over two orders of magnitude or as a short pulse (10-20 ns) generator. In Fig. 1.10(a) the difference between the on and off mode is obvious. The photocurrent fluctuations measured by the transmission photo-diode are reduced by two orders of magnitude as soon as the stabilization is turned on. In (b) the PID parameters of the feedback stabilization are tested, if they apply for long term measurements of more than 15 hours. The intensity fluctuations show a small increase over time but are still two orders below the values without AOM.

The frequency tuning in Fig. 1.10(c) and (d) is realized in two different ways. The first way is frequency tuning of the laser itself (Toptica DlPro940) inside a mode-hop free range of 4 GHz, shown in (c). The range could be extended up to 20 GHz for the experiments in Chapter 7. In this case the amplitude modulation mode and the feedback loop adjusts the intensity. Or

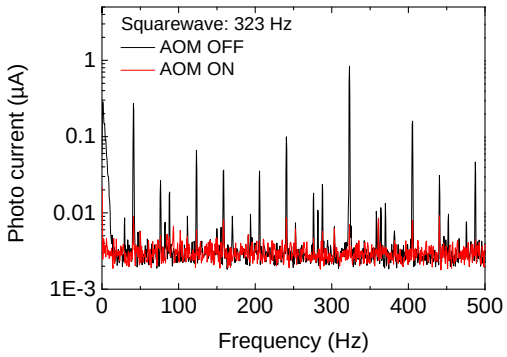

Figure 1.11 | Frequency spectrum of the laser signal, with a squarewave as artificial noise source (black) compared with the AOM intensity stabilization switched on (red).

secondly, the fine tuning option in (d), where the frequency mode of the AOM tunes the laser externally. However this mode is restricted to a small range of 200 MHz around the center frequency of the AOM. In both cases the output fluctuations are highly suppressed.

The intensity stabilization characteristics established the internal name "noise eater" when referring to the setup. Fig. 1.11 illustrates the suppression of an additional applied noise signal, in form of a square wave with a frequency of 323 Hz. The spectrum analyser demonstrates a signal reduction over 40 dB or two orders of magnitude. Last but not least the amplitude modulation of the AOM is able to create pulses as short as 10 ns, with a contrast ratio of 1:1000. This is very useful for pulsed experiments and is implemented in recent work on manipulating nuclear spin ensembles [92].

References

[1] D. Loss and D. P. DiVincenzo, Phys. Rev. A **57**, 120 (1998).

[2] G. Balasubramanian, P. Neumann, D. Twitchen, M. Markham, R. Kolesov, N. Mizuochi, J. Isoya, J. Achard, J. Beck, J. Tissler, V. Jacques, P. R. Hemmer, F. Jelezko, and J. Wrachtrup, Nat. Mater. **8**, 383 (2009).

[3] J. T. Muhonen, J. P. Dehollain, A. Laucht, F. E. Hudson, R. Kalra, T. Sekiguchi, K. M. Itoh, D. N. Jamieson, J. C. McCallum, A. S. Dzurak, and A. Morello, Nat. Nano. **9**, 986 (2014).

[4] D. Press, K. De Greve, P. L. McMahon, T. D. Ladd, B. Friess, C. Schneider, M. Kamp, S. Höfling, A. Forchel, and Y. Yamamoto, Nat. Photonics **4**, 367 (2010).

[5] D. Leonard, K. Pond, and P. M. Petroff, Phys. Rev. B **50**, 11687 (1994).

[6] C. Schneider, A. Huggenberger, T. Sünner, T. Heindel, M. Strauß, S. Göpfert, P. Weinmann, S. Reitzenstein, L. Worschech, M. Kamp, S. Höfling, and A. Forchel, Nanotechnology **20**, 434012 (2009).

[7] C. Kittel, *Introduction to Solid State Physics* (John Wiley & Sons Ltd, 1st edition, 1953).

[8] R. Winkler, *Spin-Orbit Coupling Effects in Two-Dimensional Electron and Hole Systems* (Springer Verlag, Berlin, 2003).

[9] J. M. Luttinger and W. Kohn, Phys. Rev. **97**, 869 (1955).

[10] E. O. Kane, Journal of Physics and Chemistry of Solids **1**, 249 (1957).

[11] A. Zrenner, The Journal of Chemical Physics **112**, 7790 (2000).

[12] W. Langbein, P. Borri, U. Woggon, V. Stavarache, D. Reuter, and A. D. Wieck, Phys. Rev. B **69**, 161301 (2004).

[13] Z. Wasilewski, S. Fafard, and J. McCaffrey, J.Cryst. Growth **201 - 202**, 1131 (1999).

[14] V. Mlinar, M. Bozkurt, J. M. Ulloa, M. Ediger, G. Bester, A. Badolato, P. M. Koenraad, R. J. Warburton, and A. Zunger, Phys. Rev. B **80**, 165425 (2009).

[15] K. A. Serrels, E. Ramsay, P. A. Dalgarno, B. Gerardot, J. O'Connor, R. H. Hadfield, R. J. Warburton, and D. Reid, J. Nanophotonics **2**, 021854 (2008).

[16] L. Greuter, S. Starosielec, D. Najer, A. Ludwig, L. Duempelmann, D. Rohner, and R. J. Warburton, Appl. Phys. Lett. **105**, 121105 (2014).

[17] J. Claudon, J. Bleuse, N. S. Malik, M. Bazin, P. Jaffrennou, N. Gregersen, C. Sauvan, P. Lalanne, and J.-M. Gérard, Nat. Photonics **4**, 174 (2010).

[18] A. Högele, S. Seidl, M. Kroner, K. Karrai, R. J. Warburton, B. D. Gerardot, and P. M. Petroff, Phys. Rev. Lett. **93**, 217401 (2004).

[19] A. Muller, E. B. Flagg, P. Bianucci, X. Y. Wang, D. G. Deppe, W. Ma, J. Zhang, G. J. Salamo, M. Xiao, and C. K. Shih, Phys. Rev. Lett. **99**, 187402 (2007).

[20] M. Kroner, S. Remi, A. Hoegele, S. Seidl, A. W. Holleitner, R. J. Warburton, B. D. Gerardot, P. M. Petroff, and K. Karrai, Physica E **40**, 1994 (2008).

[21] M. Kroner, C. Lux, S. Seidl, A. W. Holleitner, K. Karrai, A. Badolato, P. M. Petroff, and R. J. Warburton, Appl. Phys. Lett. **92**, 031108 (2008).

[22] P. Chen, C. Piermarocchi, and L. J. Sham, Phys. Rev. Lett. **87**, 067401 (2001).

[23] N. H. Bonadeo, J. Erland, D. Gammon, D. Park, D. S. Katzer, and D. G. Steel, Science **282**, 1473 (1998).

[24] A. Zrenner, E. Beham, S. Stufler, F. Findeis, M. Bichler, and G. Abstreiter, Nature (London) **418**, 612 (2002).

[25] P. A. Dalgarno, J. M. Smith, J. McFarlane, B. D. Gerardot, K. Karrai, A. Badolato, P. M. Petroff, and R. J. Warburton, Phys. Rev. B **77**, 245311 (2008).

[26] R. B. Liu, W. Yao, and L. J. Sham, Adv. Phys. **59**, 703 (2010).

[27] A. Greilich, D. R. Yakovlev, A. Shabaev, A. L. Efros, I. A. Yugova, R. Oulton, V. Stavarache, D. Reuter, A. Wieck, and M. Bayer, Science **313**, 341 (2006).

[28] B. Eble, C. Testelin, P. Desfonds, F. Bernardot, A. Balocchi, T. Amand, A. Miard, A. Lemaître, X. Marie, and M. Chamarro, Phys. Rev. Lett. **102**, 146601 (2009).

[29] T. M. Godden, S. J. Boyle, A. J. Ramsay, A. M. Fox, and M. S. Skolnick, Appl. Phys. Lett. **97**, 061113 (2010).

[30] M. Kroutvar, Y. Ducommun, D. Heiss, M. Bichler, D. Schuh, G. Abstreiter, and J. J. Finley, Nature (London) **432**, 81 (2004).

[31] R. J. Warburton, C. Schäflein, D. Haft, F. Bickel, A. Lorke, K. Karrai, J. M. Garcia, W. Schoenfeld, and P. M. Petroff, Nature (London) **405**, 926 (2000).

[32] H. Drexler, D. Leonard, W. Hansen, J. P. Kotthaus, and P. M. Petroff, Phys. Rev. Lett. **73**, 2252 (1994).

[33] R. J. Warburton, B. T. Miller, C. S. Dürr, C. Bödefeld, K. Karrai, J. P. Kotthaus, G. Medeiros-Ribeiro, P. M. Petroff, and S. Huant, Phys. Rev. B **58**, 16221 (1998).

[34] S. Seidl, M. Kroner, P. A. Dalgarno, A. Högele, J. M. Smith, M. Ediger, B. D. Gerardot, J. M. Garcia, P. M. Petroff, K. Karrai, and R. J. Warburton, Phys. Rev. B **72**, 195339 (2005).

[35] J. M. Smith, P. A. Dalgarno, R. J. Warburton, A. O. Govorov, K. Karrai, B. D. Gerardot, and P. M. Petroff, Phys. Rev. Lett. **94**, 197402 (2005).

[36] R. J. Warburton, C. Schulhauser, D. Haft, C. Schäflein, K. Karrai, J. M. Garcia, W. Schoenfeld, and P. M. Petroff, Phys. Rev. B **65**, 113303 (2002).

[37] J. G. Tischler, A. S. Bracker, D. Gammon, and D. Park, Phys. Rev. B **66**, 081310 (2002).

[38] M. Bayer, G. Ortner, O. Stern, A. Kuther, A. A. Gorbunov, A. Forchel, P. Hawrylak, S. Fafard, K. Hinzer, T. L. Reinecke, S. N. Walck, J. P. Reithmaier, F. Klopf, and F. Schäfer, Phys. Rev. B **65**, 195315 (2002).

[39] G. Bester, S. Nair, and A. Zunger, Phys. Rev. B **67**, 161306 (2003).

[40] A. Högele, M. Kroner, S. Seidl, K. Karrai, M. Atatüre, J. Dreiser, A. Imamoğlu, R. J. Warburton, A. Badolato, B. D. Gerardot, and P. M. Petroff, Appl. Phys. Lett. **86**, 221905 (2005).

[41] T. Belhadj, T. Amand, A. Kunold, C. M. Simon, T. Kuroda, M. Abbarchi, T. Mano, K. Sakoda, S. Kunz, X. Marie, and B. Urbaszek, Appl. Phys. Lett. **97**, 051111 (2010).

[42] M. Fleischhauer, A. Imamoglu, and J. P. Marangos, Rev. Mod. Phys. **77**, 633 (2005).

[43] X. Xu, B. Sun, P. R. Berman, D. G. Steel, Allan, Bracker, D. Gammon, and L. J. Sham, Nat. Phys. **4**, 692 (2008).

[44] D. Brunner, B. D. Gerardot, P. A. Dalgarno, G. Wüst, K. Karrai, N. G. Stoltz, P. M. Petroff, and R. J. Warburton, Science **325**, 70 (2009).

[45] J. Dreiser, M. Atatuere, C. Galland, T. Mueller, A. Badolato, and A. Imamoglu, Phys. Rev. B **77**, 075317 (2008).

[46] S. Amasha, K. MacLean, I. P. Radu, D. M. Zumbuehl, M. A. Kastner, M. P. Hanson, and A. C. Gossard, Phys. Rev. Lett. **100**, 046803 (2008).

[47] V. N. Golovach, A. Khaetskii, and D. Loss, Phys. Rev. Lett. **93**, 016601 (2004).

[48] M. Borhani, V. N. Golovach, and D. Loss, Phys. Rev. B **73**, 155311 (2006).

[49] D. V. Bulaev and D. Loss, Phys. Rev. Lett. **95**, 076805 (2005).

[50] C. Kloeffel and D. Loss, Ann. Rev. of Con. Mat Phys. **4**, 51 (2013).

[51] A. Balocchi, Q. H. Duong, P. Renucci, B. L. Liu, C. Fontaine, T. Amand, D. Lagarde, and X. Marie, Phys. Rev. Lett. **107**, 136604 (2011).

[52] A. V. Khaetskii and Y. V. Nazarov, Phys. Rev. B **64**, 125316 (2001).

[53] V. N. Golovach, A. Khaetskii, and D. Loss, Phys. Rev. B **77**, 045328 (2008).

[54] I. A. Merkulov, A. L. Efros, and M. Rosen, Phys. Rev. B **65**, 205309 (2002).

[55] A. V. Khaetskii, D. Loss, and L. Glazman, Phys. Rev. Lett. **88**, 186802 (2002).

[56] J. Fischer, M. Trif, W. A. Coish, and D. Loss, Solid State Commun. **149**, 1443 (2009).

[57] W. A. Coish and J. Baugh, Phys. Stat. Sol. (b) **246**, 2203 (2009).

[58] R. J. Warburton, Nat. Mater. **12**, 483 (2013).

[59] M. Kroner, K. M. Weiss, B. Biedermann, S. Seidl, S. Manus, A. W. Holleitner, A. Badolato, P. M. Petroff, B. D. Gerardot, R. J. Warburton, and K. Karrai, Phys. Rev. Lett. **100**, 156803 (2008).

[60] B. Urbaszek, X. Marie, T. Amand, O. Krebs, P. Voisin, P. Maletinsky, A. Högele, and A. Imamoglu, Rev. Mod. Phys. **85**, 79 (2013).

[61] W. A. Coish and D. Loss, Phys. Rev. B **70**, 195340 (2004).

[62] X. Xu, W. Yao, B. Sun, D. G. Steel, A. S. Bracker, D. Gammon, and L. J. Sham, Nature (London) **459**, 1105 (2009).

[63] M. Atatüre, J. Dreiser, A. Badolato, A. Högele, K. Karrai, and A. Imamoglu, Science **312**, 551 (2006).

[64] M. Kroner, K. M. Weiss, B. Biedermann, S. Seidl, A. W. Holleitner, A. Badolato, P. M. Petroff, P. Öhberg, R. J. Warburton, and K. Karrai, Phys. Rev. B **78**, 075429 (2008).

[65] D. Press, T. D. Ladd, B. Zhang, and Y. Yamamoto, Nature (London) **456**, 218 (2008).

[66] F. H. L. Koppens, C. Buizert, K. J. Tielrooij, I. T. Vink, K. C. Nowack, T. Meunier, L. P. Kouwenhoven, and L. M. K. Vandersypen, Nature (London) **442**, 766 (2006).

[67] J. Fischer, W. A. Coish, D. V. Bulaev, and D. Loss, Phys. Rev. B **78**, 155329 (2008).

[68] C. Testelin, F. Bernardot, B. Eble, and M. Chamarro, Phys. Rev. B **79**, 195440 (2009).

[69] B. D. Gerardot, D. Brunner, P. A. Dalgarno, P. Ohberg, S. Seidl, M. Kroner, K. Karrai, N. G. Stoltz, P. M. Petroff, and R. J. Warburton, Nature (London) **451**, 441 (2008).

[70] K. De Greve, P. L. McMahon, D. Press, T. D. Ladd, D. Bisping, C. Schneider, M. Kamp, L. Worschech, S. Höfling, A. Forchel, and Y. Yamamoto, Nat. Phys. **7**, 872 (2011).

[71] A. Greilich, S. G. Carter, D. Kim, A. S. Bracker, and D. Gammon, Nat. Photonics **5**, 702 (2011).

[72] T. M. Godden, J. H. Quilter, A. J. Ramsay, Y. Wu, P. Brereton, S. J. Boyle, I. J. Luxmoore, J. Puebla-Nunez, A. M. Fox, and M. S. Skolnick, Phys. Rev. Lett. **108**, 017402 (2012).

[73] A. N. Vamivakas, Y. Zhao, C. Y. Lu, and M. Atatüre, Nat. Phys. **5**, 198 (2009).

[74] D. Heiss, S. Schaeck, H. Huebl, M. Bichler, G. Abstreiter, J. J. Finley, D. V. Bulaev, and D. Loss, Phys. Rev. B **76**, 241306 (2007).

[75] M. Trif, P. Simon, and D. Loss, Phys. Rev. Lett. **103**, 106601 (2009).

[76] P. Fallahi, S. T. Yilmaz, and A. Imamoğlu, Phys. Rev. Lett. **105**, 257402 (2010).

[77] E. A. Chekhovich, M. N. Makhonin, K. V. Kavokin, A. B. Krysa, M. S. Skolnick, and A. I. Tartakovskii, Phys. Rev. Lett. **104**, 066804 (2010).

[78] J. Fischer and D. Loss, Science **324**, 1277 (2009).

[79] H. Ribeiro, F. Maier, and D. Loss, arXiv:1403.0490 (2014).

[80] B. Alén, F. Bickel, K. Karrai, R. J. Warburton, and P. M. Petroff, Appl. Phys. Lett. **83**, 2235 (2003).

[81] K. Karrai and R. J. Warburton, Superlattice Microst. **33**, 311 (2003).

[82] T. Wilson, *Confocal Microscopy* (Academic, London, 1990).

[83] A. Högele, S. Seidl, M. Kroner, K. Karrai, C. Schulhauser, O. Sqalli, J. Scrimgeour, and R. J. Warburton, Rev. Sci. Instrum. **79**, 023709 (2008).

[84] J. Houel, A. V. Kuhlmann, L. Greuter, F. Xue, M. Poggio, B. D. Gerardot, P. A. Dalgarno, A. Badolato, P. M. Petroff, A. Ludwig, D. Reuter, A. D. Wieck, and R. J. Warburton, Phys. Rev. Lett. **108**, 107401 (2012).

[85] A. V. Kuhlmann, J. Houel, A. Ludwig, L. Greuter, D. Reuter, A. D. Wieck, , M. Poggio, and R. J. Warburton, Nat. Phys. **9**, 570 (2013).

[86] B. D. Gerardot, R. J. Barbour, D. Brunner, P. A. Dalgarno, A. Badolato, N. Stoltz, P. M. Petroff, J. Houel, and R. J. Warburton, Appl. Phys. Lett. **99**, 243112 (2011).

[87] A. V. Kuhlmann, J. Houel, D. Brunner, A. Ludwig, D. Reuter, A. D. Wieck, and R. J. Warburton, Rev. Sci. Instrum. **84**, 073905 (2013).

[88] S. Ates, S. M. Ulrich, S. Reitzenstein, A. Löffler, A. Forchel, and P. Michler, Phys. Rev. Lett. **103**, 167402 (2009).

[89] S. E. Harris, S. T. K. Nieh, and D. K. Winslow, Appl. Phys. Lett. **15**, 325 (1969).

[90] S. R. Jefferts, J. Shirley, T. E. Parker, T. P. Heavner, D. M. Meekhof, C. Nelson, F. Levi, G. Costanzo, A. D. Marchi, R. Drullinger, L. Hollberg, W. D. Lee, and F. L. Walls, Metrologia **39**, 321 (2002).

[91] E. A. Donley, T. P. Heavner, F. Levi, M. O. Tataw, and S. R. Jefferts, Review of Scientific Instruments **76**, 063112 (2005).

[92] M. Munsch, G. Wüst, A. V. Kuhlmann, F. Xue, A. Ludwig, D. Reuter, A. D. Wieck, M. Poggio, and R. J. Warburton, Nat. Nano. **9**, 671 (2014).

PART II

Studies on a coherent hole spin using optical techniques

Chapter 2

Coherent superposition of single hole spins in a semiconductor

Adapted from:

Julien Houel, Jonathan H. Prechtel, Andreas V. Kuhlmann, Daniel Brunner, Christopher E. Kuklewicz, Brian D. Gerardot, Nick G. Stoltz, Pierre M. Petroff, and Richard J. Warburton **"High resolution coherent population trapping on a single hole spin in a semiconductor"**

Phys. Rev. Lett. **112**, 107401 (2014)

We report high resolution coherent population trapping on a single hole spin in a semiconductor quantum dot. The absorption dip signifying the formation of a dark state exhibits an atomic physics-like dip width of just 10 MHz. We observe fluctuations in the absolute frequency of the absorption dip, evidence of very slow spin dephasing. We identify the cause of this process as charge noise by, first, demonstrating that the hole spin g-factor in this configuration (in-plane magnetic field) is strongly dependent on the vertical electric field, and second, by characterizing the charge noise through its effects on the optical transition frequency. An important conclusion is that charge noise is an important hole spin dephasing process.

(Experiments and results presented in this chapter were obtained in close collaboration with Dr. Julien Houel, who performed parts of the experiments in the old nano-optics laboratory in Edinburgh.)

2.1 Introduction

Coherent population trapping (CPT) is a quantum interference effect which arises in an optical Λ system [1]. Two ground states are coupled individually by "pump" and "probe" lasers to a common upper level. At the two-photon resonance when the frequency difference of the lasers matches the frequency difference of the ground states, one of the three eigenstates has zero amplitude of the upper level, the "dark" state. CPT refers to the signature of the dark state, a dip in the probe absorption spectrum as the probe is tuned through the two-photon resonance. Specifically, for probe ($\hbar\Omega_1$) and pump laser couplings ($\hbar\Omega_2$) in the perturbative regime $\hbar\Omega_1 \ll \hbar\Omega_2 \ll \hbar\Gamma_r$ (Γ_r is the spontaneous emission rate from the upper state), the dip has width $\hbar\Omega_2^2/\Gamma_r$. A sketch of the 3-level Λ-system shows Fig. 2.1.

CPT is a key effect in atomic physics. First, CPT forms the microscopic basis of electromagnetically-induced transparency which itself underpins a scheme for slowing light [2]. Secondly, the narrow dip enables the frequency separation of the ground states to be measured extremely precisely by optical means. Thirdly, the dark state of CPT can be used for quantum control [3]. Finally, the "visibility" of the quantum interference at the CPT dip is sensitive to the ground state coherence (but insensitive to the upper state coherence) [4–7]: ground state decoherence admixes the dark state with the two bright states. The dip width sets the sensitivity to the decoherence time T_2: for $1/T_2 \ll \Omega_2^2/\Gamma_r$ the signal in the dip goes to zero but for $1/T_2 \gg \Omega_2^2/\Gamma_r$ the dip is washed out. The sensitivity to the dephasing time T_2^* comes about because ground state dephasing implies a fluctuating two-photon resonance position, resulting in both an increase in dip width and a decrease in "visibility".

It is motivating to implement CPT in a semiconductor. Systems include excitons in GaAs quantum wells [8], bound excitons in GaAs [9], and spin states in InGaAs quantum dots [5–7]. The challenge is to engineer two ground states with T_2 and T_2^* times much larger than the radiative lifetime τ_r of the upper state. A single electron in an InGaAs quantum dot is an obvious candidate: the spin states represent a two-level system, and spontaneous emission is fast, $\tau_r \sim 1$ ns [10]. Unfortunately, in the presence of noisy nuclei, the hyperfine interaction limits T_2^* to just a few ns [11, 12] and the CPT dip can only be observed at large optical couplings where it is inevitably broad [5]. The situation improves either by reducing the nuclear spin noise [13] or by using a quantum dot molecule [7] at a point where the first order sensitivity to spin noise vanishes.

A hole spin is potentially simpler. A heavy hole state with spin eigenvectors $J = \frac{3}{2}, J_z = \pm\frac{3}{2}$ is predicted to become coherent in an in-plane magnetic field [14]. In that case the hole spin superposition state is maintained over a period longer than just a few ns. Conveniently, the in-plane magnetic field is exactly the field direction required to establish the Λ system, as described in the introductory chapter and in Fig. 2.1 [5, 6]. The key point is that a perfect

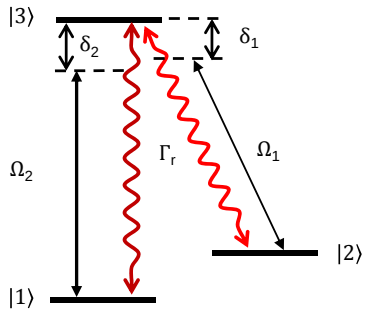

Figure 2.1 | 3-level Λ-system. The energetically split ground state levels $|1\rangle$ and $|2\rangle$ are coupled by two optical fields Ω_1 and Ω_2, respectively, to a common upper level, $|3\rangle$. δ_1 and δ_2 indicate the probe and pump detunings of the optical fields to the upper level.

heavy hole spin is sensitive to nuclear spin noise only along the vertical direction z, noise which can be suppressed by applying an external magnetic field in the (x, y)-plane [14]. The extent to which the idealized heavy hole picture applies to a real hole in a quantum dot has been explored in a number of recent optical experiments [6, 15–21]. The Hahn echo T_2 is in the µs range [20], a remarkable result bearing in mind the extremely limited hole spin coherence in quantum wells and bulk material [22, 23]. Spin dephasing times T_2^* lie in the $10 - 100$ ns regime with significant differences from experiment to experiment [6, 19–21]. CPT dips have been observed on a single hole spin [6] but these experiments used optical couplings only slightly less than the radiative decay rate, resulting in dip widths of ~ 100 MHz. This is too large for slow light, high resolution spectroscopy and quantum metrology applications. It also renders the experiment insensitive to decoherence times above about 100 ns.

2.2 Coherent population trapping experiment

We report here CPT on a single hole spin in the perturbative regime. A dip width of just 10 MHz is demonstrated. The residual absorption in the center of the dip is zero (within random error), consistent with a coherence time $T_2 \geq 1$ µs. However, we discover a scan-to-scan variation in the CPT position. We relate this to charge noise. On the one hand, we measure the dependence of the hole spin g-factor on vertical electric field. On the other hand, we quantify the fluctuations in vertical electric field through their effects on the optical transition, the dependence arising via the dc Stark effect. We identify charge noise as an important dephasing mechanism for the quantum dot hole spin. Charge-noise induced spin dephasing is potentially important for other spin qubits with an electric-field dependent g-factor and for systems with a strong spin-orbit interaction.

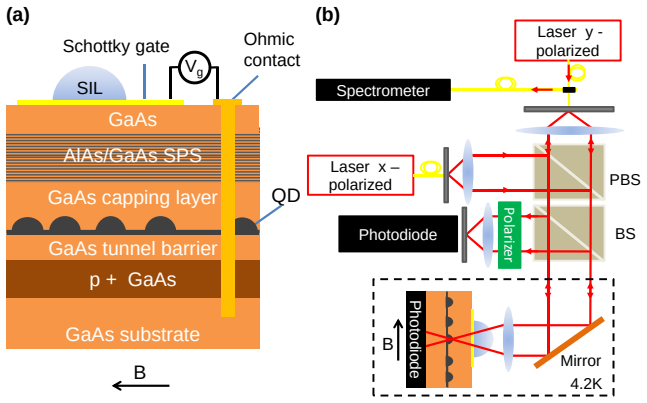

Figure 2.2 | (a) Layer sequence of the semiconductor heterostructure. The tunnel barrier is 25 nm, capping layer 10 nm and short-period superlattice 120 nm. Post-growth, Ohmic contacts along with a semi-transparent surface gate electrode are fabricated. (b) Schematic of the optical set-up.

2.2.1 Device and measurement method

The semiconductor device is a p-type charge-tunable heterostructure to which a voltage V_g is applied, Fig. 2.2(a) [6, 15, 24]. Laser spectroscopy is carried out using differential reflectivity ($\Delta R/R$) detection, Fig. 2.2(b) [25, 26]. The exciton's optical linewidth is dot dependent, typically $5-10$ μeV [24]. This is considerably larger than both the transform limit, ~ 0.8 μeV [27], and the linewidths on high quality n-type samples, ~ 1.5 μeV [25, 27], and reflects additional charge noise associated with the p-type doping [24]. A magnetic field of 0.5 T is applied in the plane, and then two-color pump-probe laser spectroscopy is carried out using two coherent lasers. The experiment is very challenging: $\Delta R/R$ is very small at the optical resonance (0.1%); at the ultra-low laser powers used here noise in the detector circuit is significant; and in the perturbative regime ($\hbar\Omega_1 \ll \hbar\Omega_2 \ll \hbar/\tau_r$), the width of the CPT dip approaches the limit set by the mutual coherence of the lasers. We meet these challenges with a solid immersion lens to boost the $\Delta R/R$ signal, a modulation technique to reject noise in the reflectivity signal, and a stabilization scheme to lock the pump-probe frequency difference to a radio frequency reference (mutual coherence of 2.0 MHz in 30 s).

2.2.2 Ultranarrow CPT dip

A CPT dip on a single hole spin in a magnetic field of 0.5 T and temperature 4.2 K is shown in Fig. 2.3. The optical couplings $\hbar\Omega_1$, $\hbar\Omega_2$ were determined by measuring an Autler-Townes splitting at high laser powers, extrapolating the couplings to low laser powers using the scaling $\hbar\Omega \propto \sqrt{P}$ (P is the laser power), Fig. 2.4(a). In the CPT experiment, $\hbar\Omega_2$ is a factor of 3 lower than the spontaneous decay rate $\Gamma_r = 1/\tau_r$. The full-width-at-half-maximum of the CPT dip

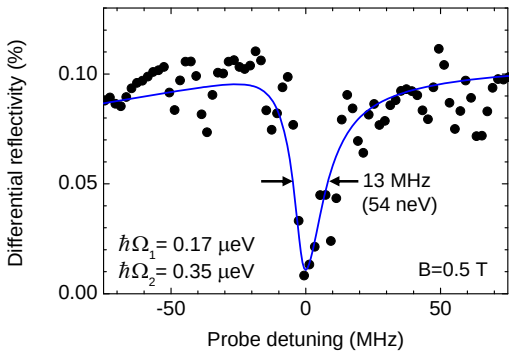

Figure 2.3 | Probe absorption in the presence of a close-to-resonant pump laser on a single InGaAs quantum dot containing a single hole spin at $B = 0.5$ T and $T = 4.2$ K, 10 s integration per point. The absorption (here, differential reflectivity $\Delta R/R$) shows an absorption dip signifying coherent population trapping. The solid line shows the result of a 3-level density matrix model ($\hbar\Omega_1 = 0.17$ μeV, $\hbar\Omega_2 = 0.35$ μeV, $\hbar\delta_2 = -2.5$ μeV, $\hbar/\tau_r = 0.8$ μeV, $T_2 \geq 1$ μs, $T_1 \gg T_2$) convoluted with a Lorentzian with FWHM $\Gamma_X = 5$ μeV (1.22 GHz) to describe slow exciton dephasing, and then with a Lorentzian with FWHM 8.3 neV (2.0 MHz) to account for the mutual coherence of the lasers.

is just 13 MHz, equivalently 54 neV, corresponding to just 10^{-7} of the frequency of the optical transitions, and just 10^{-3} of the thermal energy. Fig. 2.3 constitutes our main result: a CPT dip linewidth in the MHz regime, a spectral sensitivity usually associated with atomic physics and not a semiconductor experiment.

The solid-lines in Fig.s 2.3 and 2.4(a) correspond to the results of a 3-level density matrix (ρ) calculation [6]. The derivation and the calculations with the density matrix formalism are described in Appendix C. The resulting matrix element ρ_{13} [2] (in the case of reflectivity measurements) is convoluted with a Lorentzian distribution of width Γ_X in the energy of the upper level, $|3\rangle$, in order to describe the effects of charge noise. Γ_X is known from the one-laser characterization at $B = 0$. The result is then convoluted again, this time with a Lorentzian function of width 2.0 MHz (8.3 neV) to describe the limited mutual coherence of the lasers. In the limit of large $\hbar\Omega_2$, the Autler-Townes experiment, $\hbar\Omega_2$ is treated as a fit parameter, and the result describes the absorption envelope extremely well, Fig. 2.4(a). In the limit of small $\hbar\Omega_2$, the CPT experiment, the result describes the dip width and depth extremely well (Fig. 2.3). In the CPT limit, there are no unknowns apart from a small uncertainty in $\hbar\delta_2$, the pump-detuning (see below).

The residual signal in the CPT dip of Fig. 2.3 can be fully accounted for by the mutual coherence of the lasers: the condition $1/T_2 \ll \Omega_2^2/\Gamma_r$ is satisfied, which translates to $T_2 \geq 1$ μs. Furthermore, the width of the CPT dip in Fig. 2.3 is described with the 3-level model without ensemble averaging. This sets a lower limit on the dephasing time: from the uncertainty in the CPT width (Fig. 2.3) we determine $T_2^* \geq 100$ ns. A measurement of T_2^* on a single emitter

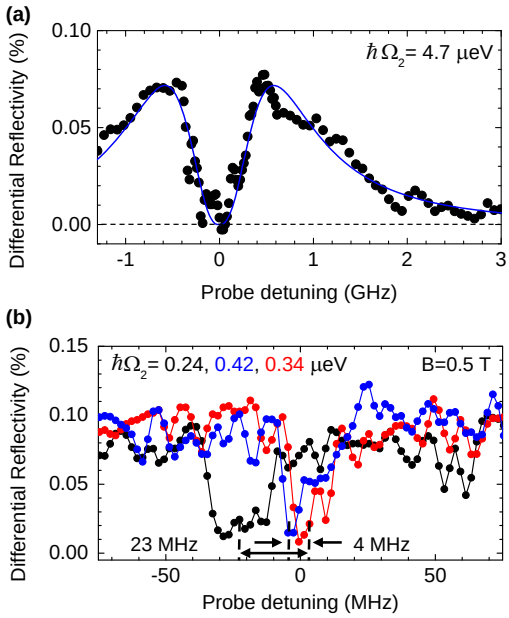

Figure 2.4 | (a) Probe absorption versus probe detuning on the same quantum dot as Fig. 2.3 in the regime $\hbar\Omega_2 \gg \hbar/\tau_r$ showing an Autler-Townes splitting. The solid curve is a fit to the data, $\hbar\Omega_2 = 4.7$ μeV, $\hbar\delta_2 = 0.0$ μeV, as fit parameters. $\Gamma_X = 7.5$ μeV is taken from $\Delta R/R$ at $B = 0$. (b) Probe absorption versus probe detuning on the same quantum dot in the regime $\hbar\Omega_2 \ll \hbar/\tau_r$. Three curves are shown under close-to-identical conditions showing a shift in the location of the dip in one case by 4 MHz (17 neV), and in another case by 23 MHz (95 neV).

involves an integration of the experiment in time, equivalently over a frequency bandwidth. The value of T_2^* deduced from Fig. 2.3 represents an integration over measurement frequencies starting at about 0.01 Hz.

2.2.3 High resolution dark state spectroscopy

We take advantage of the narrow dip to perform high resolution dark state spectroscopy. We find that the frequency of the dip fluctuates from scan to scan, Fig. 2.4(b), over a range of $\sim$ 5 MHz ($\sim$ 20 neV). Occasionally, larger frequency shifts are observed, possibly with an unusual lineshape, Fig. 2.4(b). These effects point to the presence of very slow fluctuations in the frequency separation of the hole spin ground states. In terms of T_2^*, we find that T_2^* falls to just $\sim$ 30 ns when the measurement bandwidth starts at $\sim$ 0.0001 Hz. It is unlikely that nuclear spin noise is responsible for this extra noise at very low frequencies. On the one hand, nuclear spin noise lies at higher frequencies [27]; on the other hand, we have not observed any hysteresis effects in the CPT experiment, the typical signature of the nuclear spins. The slow CPT fluctuations are reminiscent of the low frequency wanderings of the optical transition

which has a $1/f$-like noise spectrum and arises from charge noise [27]. We therefore look for a link between charge noise and the hole g-factor.

2.3 Hole spin dephasing

2.3.1 Electric field dependence of the hole g-factor

We have characterized the eigenenergies as a function of V_g by measuring the photoluminescence (PL) from the positively-charged trion X^{1+} in an in-plane magnetic field $B = 9$ T, Fig. 2.5(a). We resolve 4 lines corresponding to the two "vertical" transitions and the two "diagonal" transitions, Fig. 2.5(a),(b). Fig. 2.5 shows the V_g dependence of the electron and hole Zeeman energies. To within error, $\sim 0.25\%$, the electron Zeeman energy Z_e is independent of V_g; in contrast, the hole Zeeman energy Z_h changes by $\sim 5\%$ over the X^{1+} plateau. Defining the g_h via $Z_h = g_h \mu_B B$, we find $g_h = 0.15 + \alpha F$ with $\alpha = 8.6 \times 10^{-4}$ cm/kV (F is the vertical electric field).

The dependence of g_h on F creates a mechanism by which charge noise can result in spin dephasing: electric field fluctuations cause changes to the hole spin precession frequency. In particular, the low frequency charge noise causes both the optical transition energy and the CPT dip position to wander. Specifically, the charge noise in a bandwidth $f_{\text{scan}} \leq f \leq 1/\tau_r$ can be determined by measuring the optical linewidth at rate f_{scan}, converting the inhomogeneous broadening into electric field noise via the known Stark shift. This is easy to measure with the resonant laser spectroscopy employed here. Charge noise at lower frequencies, $f \leq f_{\text{scan}}$, results in scan-to-scan fluctuations of the resonance energy. CPT is recorded on the same quantum dot experiencing the same noise: a powerful connection can therefore be made between the optical linewidth and the CPT experiment.

The optical linewidth of the transition probed via CPT in Fig. 2.3 is 5.0 μeV. Together with the known Stark shifts, $dE/dF = 18$ μeV/kVcm^{-1} [$dE/dV_g = 1.12$ μeV/mV], this results in $\Delta F = 0.28$ kV/cm [$\Delta V_g = 4.5$ mV]. This charge noise, ΔF, results in turn in a fluctuation in g_h of $\Delta g_h = 2.4 \times 10^{-4}$, equivalently, $\Delta Z_h = 7$ neV (1.7 MHz) at 0.5 T. This broadening is comparable to the frequency resolution of the experiment and therefore plays a small role. This explains why the CPT dip in Fig. 2.3 can be explained without taking into account charge noise-induced dephasing. The effects in Fig. 2.4(b) arise when f_{scan} is reduced even further. In this case, ultralow frequency flicker noise results in wanderings of the quantum dot optical resonance typically by one or two linewidths over the course of many minutes [27]. These optical shifts induce in turn wanderings of the CPT dip, by a few MHz, as observed in Fig. 2.4(b). The larger shifts in CPT position, Fig. 2.4(b), may represent highly unlikely but more extreme changes to the electrostatic environment of the quantum dot.

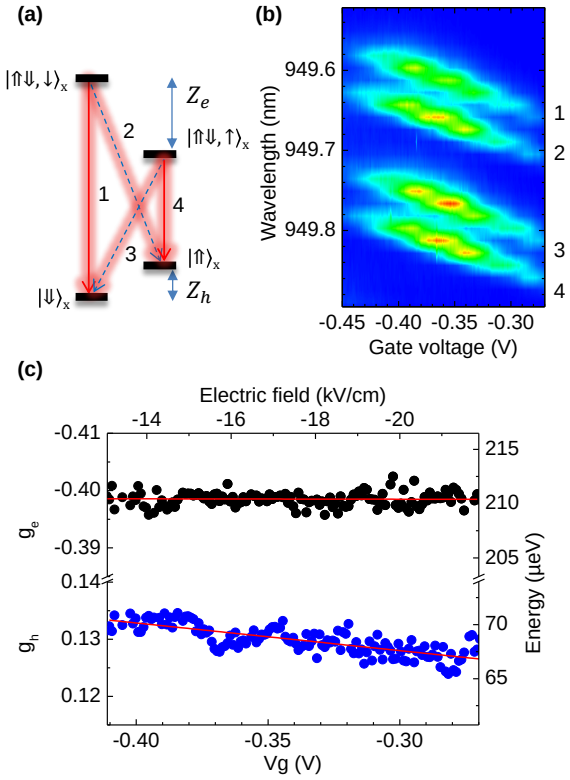

Figure 2.5 | (a) The quantum states of a single hole spin in an in-plane magnetic field. $\uparrow,\downarrow$ denotes an electron spin, $\Uparrow,\Downarrow$ a hole spin. (b) Photoluminescence on a single InGaAs quantum dot (different quantum dot from Fig. 2.3, 2.4 but from the same wafer) at $B = 9.0$ T and $T = 4.2$ K as a function of V_g over the extent of the single hole Coulomb blockade plateau. Four transitions are visible, labeled $1-4$, and identified in (a). The width of each peak is determined by the spectrometer-detector (system resolution 50 μeV). The apparent steps are an artifact arising from the pixelated detector. (c) Electron and hole g-factors, g_e and g_h, versus V_g. V_g is converted into vertical electric field F with $F = -e(V_g + V_o)/D$ with $D = 155$ nm and Schottky barrier $V_o = 0.62$ V. Under the assumption of a negative g_e, g_h is positive. The error on each point is ~ 2 μeV using a routine which corrects for the detector pixelation.

2.3.2 Charge noise as hole dephasing mechanism

Our results point to the role of charge noise in dephasing a quantum dot hole spin. In this experiment, the charge noise in Z_h implies a dephasing time of $T_2^{*,c} \simeq 100$ ns on integrating noise in a bandwidth starting around 0.01 Hz at $B = 0.5$ T. $T_2^{*,c}$ reflects an upper limit to T_2^* for a given f_{scan}: other processes could reduce T_2^* further. A consistency check is that the measured T_2^* in a similar bandwidth (Fig. 2.3) cannot be higher than $T_2^{*,c}$. This is indeed the case. Specifically, the experiment demonstrates that charge noise is the dominant dephasing mechanism at very low values of f_{scan} (Fig. 2.4(b)).

The key to increasing T_2^* is to reduce the charge noise. Some quantum dots in the sample have lower optical linewidths despite similar Stark shifts pointing to a lower level of local charge noise

and for these quantum dots we can expect $T_2^* \geq 100$ ns. Generally speaking, these resonant laser spectroscopy experiments have low charge noise, much less than in experiments with non-resonant excitation [27]. Experiments with more charge noise will therefore give smaller hole spin T_2^* values. Charge noise also results in a B-dependence of T_2^*. We find that dg_h/dF is B-independent: the fluctuations in Z_h increase linearly with increasing B for constant charge noise implying that T_2^* scales as $1/B$: $T_2^* \simeq \hbar/(|dg_h/dF|\,\Delta F\,\mu_B B)$. The B-dependence may be obscured should other dephasing mechanisms come into play at higher magnetic fields, for instance hyperfine coupling [20, 21] or the interaction with phonons [16, 28]. We note however that hole spin dynamics at magnetic fields of several Tesla reveal smaller T_2^* values [20, 21] than those at low magnetic field [6, 19], and this is consistent with charge noise-dominated spin dephasing. We stress that an advantage of the present experiment is that the charge noise is measured in situ via the laser spectroscopy.

2.4 Conclusion

In conclusion, we report 10 MHz wide CPT dips in laser spectroscopy experiments on a quantum dot hole spin. The quantum dot is embedded in a very good but imperfect device. Charge noise causes slow wanderings of the CPT dip. There are a number of mitigating strategies. First, p-type devices need to be developed with less charge noise, ideally with the low levels of charge noise associated with the best n-type devices. Secondly, the dependence of the hole g-factor on electric field, while possibly an attractive feature for electrical qubit control, can be reduced by appropriate quantum dot design.

References

[1] E. Arimondo, Prog. Opti. **35**, 257 (1996).

[2] M. Fleischhauer, A. Imamoglu, and J. P. Marangos, Rev. Mod. Phys. **77**, 633 (2005).

[3] K. Bergmann, H. Theuer, and B. W. Shore, Rev. Mod. Phys. **70**, 1003 (1998).

[4] A. Imamoglu, Phys. Stat. Sol. (b) **243**, 3725 (2006).

[5] X. Xu, B. Sun, P. R. Berman, D. G. Steel, Allan, Bracker, D. Gammon, and L. J. Sham, Nat. Phys. **4**, 692 (2008).

[6] D. Brunner, B. D. Gerardot, P. A. Dalgarno, G. Wüst, K. Karrai, N. G. Stoltz, P. M. Petroff, and R. J. Warburton, Science **325**, 70 (2009).

[7] K. M. Weiss, J. M. Elzerman, Y. L. Delley, J. Miguel-Sanchez, and A. Imamoğlu, Phys. Rev. Lett. **109**, 107401 (2012).

[8] M. C. Phillips, H. Wang, I. Rumyantsev, N. H. Kwong, R. Takayama, and R. Binder, Phys. Rev. Lett. **91**, 183602 (2003).

[9] M. Sladkov, A. U. Chaubal, M. P. Bakker, A. R. Onur, D. Reuter, A. D. Wieck, and C. H. van der Wal, Phys. Rev. B **82**, 121308 (2010).

[10] P. A. Dalgarno, M. Ediger, B. D. Gerardot, J. M. Smith, S. Seidl, M. Kroner, K. Karrai, P. M. Petroff, A. O. Govorov, and R. J. Warburton, Phys. Rev. Lett. **100**, 176801 (2008).

[11] I. A. Merkulov, A. L. Efros, and M. Rosen, Phys. Rev. B **65**, 205309 (2002).

[12] A. V. Khaetskii, D. Loss, and L. Glazman, Phys. Rev. Lett. **88**, 186802 (2002).

[13] X. Xu, W. Yao, B. Sun, D. G. Steel, A. S. Bracker, D. Gammon, and L. J. Sham, Nature (London) **459**, 1105 (2009).

[14] J. Fischer, W. A. Coish, D. V. Bulaev, and D. Loss, Phys. Rev. B **78**, 155329 (2008).

[15] B. D. Gerardot, D. Brunner, P. A. Dalgarno, P. Ohberg, S. Seidl, M. Kroner, K. Karrai, N. G. Stoltz, P. M. Petroff, and R. J. Warburton, Nature (London) **451**, 441 (2008).

[16] D. Heiss, V. Jovanov, M. Bichler, G. Abstreiter, and J. J. Finley, Phys. Rev. B **77**, 235442 (2008).

[17] A. J. Ramsay, S. J. Boyle, R. S. Kolodka, J. B. B. Oliveira, J. Skiba-Szymanska, H. Y. Liu, M. Hopkinson, A. M. Fox, and M. S. Skolnick, Phys. Rev. Lett. **100**, 197401 (2008).

[18] T. M. Godden, S. J. Boyle, A. J. Ramsay, A. M. Fox, and M. S. Skolnick, Appl. Phys. Lett. **97**, 061113 (2010).

[19] S. A. Crooker, J. Brandt, C. Sandfort, A. Greilich, D. R. Yakovlev, D. Reuter, A. D. Wieck, and M. Bayer, Phys. Rev. Lett. **104**, 036601 (2010).

[20] K. De Greve, P. L. McMahon, D. Press, T. D. Ladd, D. Bisping, C. Schneider, M. Kamp, L. Worschech, S. Höfling, A. Forchel, and Y. Yamamoto, Nat. Phys. **7**, 872 (2011).

[21] A. Greilich, S. G. Carter, D. Kim, A. S. Bracker, and D. Gammon, Nat. Photonics **5**, 702 (2011).

[22] T. C. Damen, L. Vina, J. E. Cunningham, J. Shah, and L. J. Sham, Phys. Rev. Lett. **67**, 3432 (1991).

[23] X. Marie, T. Amand, P. Le Jeune, M. Paillard, P. Renucci, L. E. Golub, V. D. Dymnikov, and E. L. Ivchenko, Phys. Rev. B **60**, 5811 (1999).

[24] B. D. Gerardot, R. J. Barbour, D. Brunner, P. A. Dalgarno, A. Badolato, N. Stoltz, P. M. Petroff, J. Houel, and R. J. Warburton, Appl. Phys. Lett. **99**, 243112 (2011).

[25] A. Högele, S. Seidl, M. Kroner, K. Karrai, R. J. Warburton, B. D. Gerardot, and P. M. Petroff, Phys. Rev. Lett. **93**, 217401 (2004).

[26] B. Alén, A. Högele, M. Kroner, S. Seidl, K. Karrai, R. J. Warburton, A. Badolato, G. Medeiros-Ribeiro, and P. M. Petroff, Appl. Phys. Lett **89**, 123124 (2006).

[27] A. V. Kuhlmann, J. Houel, A. Ludwig, L. Greuter, D. Reuter, A. D. Wieck, , M. Poggio, and R. J. Warburton, Nat. Phys. **9**, 570 (2013).

[28] M. Trif, P. Simon, and D. Loss, Phys. Rev. Lett. **103**, 106601 (2009).

PART III

High quality devices and noise reduction

Chapter 3

Charge noise suppression with a feedback scheme

Adapted from:

Jonathan H. Prechtel, Andreas V. Kuhlmann, Julien Houel, Lukas Greuter, Arne Ludwig, Dirk Reuter, Andreas D. Wieck, and Richard J. Warburton

"A frequency-stabilized source of single photons from a solid-state qubit"

Phys. Rev. X **3**, 041006 (2013)

Single quantum dots are solid-state emitters which mimic two-level atoms but with a highly enhanced spontaneous emission rate. A single quantum dot is the basis for a potentially excellent single photon source. One outstanding problem is that there is considerable noise in the emission frequency, making it very difficult to couple the quantum dot to another quantum system. We solve this problem here with a dynamic feedback technique that locks the quantum dot emission frequency to a reference. The incoherent scattering (resonance fluorescence) represents the single photon output whereas the coherent scattering (Rayleigh scattering) is used for the feedback control. The fluctuations in emission frequency are reduced to 20 MHz, just $\sim 5\%$ of the quantum dot optical linewidth, even over several hours. By eliminating the $1/f$-like noise, the relative fluctuations in resonance fluorescence intensity are reduced to $\sim 10^{-5}$ at low frequency. Under these conditions, the antibunching dip in the resonance fluorescence is described extremely well by the two-level atom result. The technique represents a way of removing charge noise from a quantum device.

3.1 Introduction

Single photons are ideal carriers of quantum information [1–3]. A quantum state stored in one of the degrees of freedom of the photon's wave packet (polarization, phase or time-bin) can be maintained over long distances. Single photons are therefore important in quantum communication [3], for coupling remote stationary qubits [4], the basis of a quantum repeater [5], or for coupling different elements in a quantum device. Furthermore, single photons are the seed for a variety of quantum optics experiments [6, 7].

Key parameters for a single photon source are fidelity of the antibunching, flux, wavelength and photon indistinguishability [8]. Remarkably, solid-state emitters are presently better able to meet these demands than atomic systems [6, 7]. In particular, spontaneous emission from individual quantum dots embedded in an inorganic semiconductor is a very promising source of highly antibunched, high flux, indistinguishable photons [7, 9, 10]. The antibunching, particularly with resonant excitation, is very high [11]. The radiative lifetime is very short, typically just less than 1 ns [12]. The flux is usually limited by the poor collection efficiency: most of the light is internally reflected at the GaAs-vacuum interface. However, this problem can be solved by nano-structuring the photonic modes to create a micro-cavity [13] or a photonic nanowire [14]. In the latter case, collection efficiencies of $\sim 70\%$ have been achieved. The photon indistinguishability is very high for successive photons [10]. Based on the optical linewidth, typically a factor of two above the transform limit when measured with resonant excitation [15–18], the indistinguishability is also reasonably high for photons emitted widely separated in time. Furthermore, a single quantum dot has also been developed as a spin qubit [19], facilitating an interface between stationary qubits and photons [20–22].

Unlike a real atom, the exact transition wavelength of a quantum dot is not locked to any particular wavelength and varies considerably from quantum dot to quantum dot. However, the host semiconductor can be designed so that considerable possibilities for tuning the emission wavelength exist. Electric field tuning [23, 24] and strain tuning [25, 26] allow the emission wavelength to be tuned over several nanometres. A major problem remains. The emission wavelength is not constant: it varies randomly over time, even in very controlled environments at low temperature. The culprit at low frequency is electrical noise in the semiconductor which shifts the emission wavelength via the Stark effect [18]. This noise has a $1/f$-like power spectrum resulting in, first, large and uncontrolled drifts at low frequencies and second, an undefined mean value. This noise, while poorly understood, is ubiquitous in semiconductors and makes it very difficult to couple an individual quantum dot to another quantum system, another quantum dot for instance, or an ensemble of cold atoms. We present here a new scheme which solves this problem: we create a stream of single photons with a wavelength which remains constant even over several hours.

The output of our quantum device is a stream of single photons generated by resonance fluorescence (RF) from a single quantum dot. RF has considerable advantages over non-resonant excitation of photoluminescence: the linewidth is much lower [17, 18] and the antibunching is much better. We lock the wavelength of the quantum device to a stable reference. We generate an error signal, a signal with large slope at its zero-crossing, by measuring the differential transmission, $\Delta T/T$, simultaneously [15, 27, 28]. The control variable is the voltage V_g applied to a surface gate which influences the quantum dot frequency via the Stark effect. The performance of the feedback scheme is characterized by, first, measuring a series of snap-shots of the optical resonance to assess the residual frequency jitter; and second, by carrying out a full analysis of the noise in the RF.

Our scheme goes well beyond previous attempts at single emitter stabilization in the solid-state [29, 30]. The first experiment on frequency stabilization locked a non-standard quantum dot at 780 nm to the atomic resonance of Rb [29]. We are not limited to any "magic" wavelengths, and in particular we can stabilize the emission wavelengths of high-quality InGaAs quantum dots which typically emit in the $900 - 1000$ nm range. The second advance of our scheme is a 100 times better frequency stabilization relative to ref. [29]. Here, the absolute frequency of the quantum dot emission is locked with an uncertainty of just 20 MHz. We observe a reduction in the noise power up to a frequency of ~ 100 Hz, a bandwidth high enough to eliminate the substantial drifts at low frequency.

3.2 Feedback scheme

3.2.1 The Concept

A sketch of the experimental concept is shown in Fig. 3.1(a). A linearly-polarized resonant laser is focused onto the sample surface and drives the optical transition. The resonance fluorescence of the quantum dot is collected with a polarization-based dark field technique [17, 20, 31], described in detail elsewhere [32]. Simultaneously, the optical resonance is detected in transmission by superimposing a sub-linewidth modulation to the gate. The transmission signal arises from an interference of quantum dot scattering with the driving laser [28]. The incoherent part, i.e. the resonance fluorescence, averages to zero in transmission; what is detected instead is the coherent scattering, i.e. the Rayleigh scattering. In this way, the experiment utilizes both incoherent and coherent parts of the scattered light, for the single photon output and control, respectively. With a small modulation, the transmission signal has a large slope with zero crossing at zero detuning and is therefore ideal for the generation of an error signal. $\Delta T/T$, the error signal, is recorded with a lock-in amplifier to reject noise and the lock-in output is fed into a classical feedback scheme. The feedback output is, like the modulation, applied to

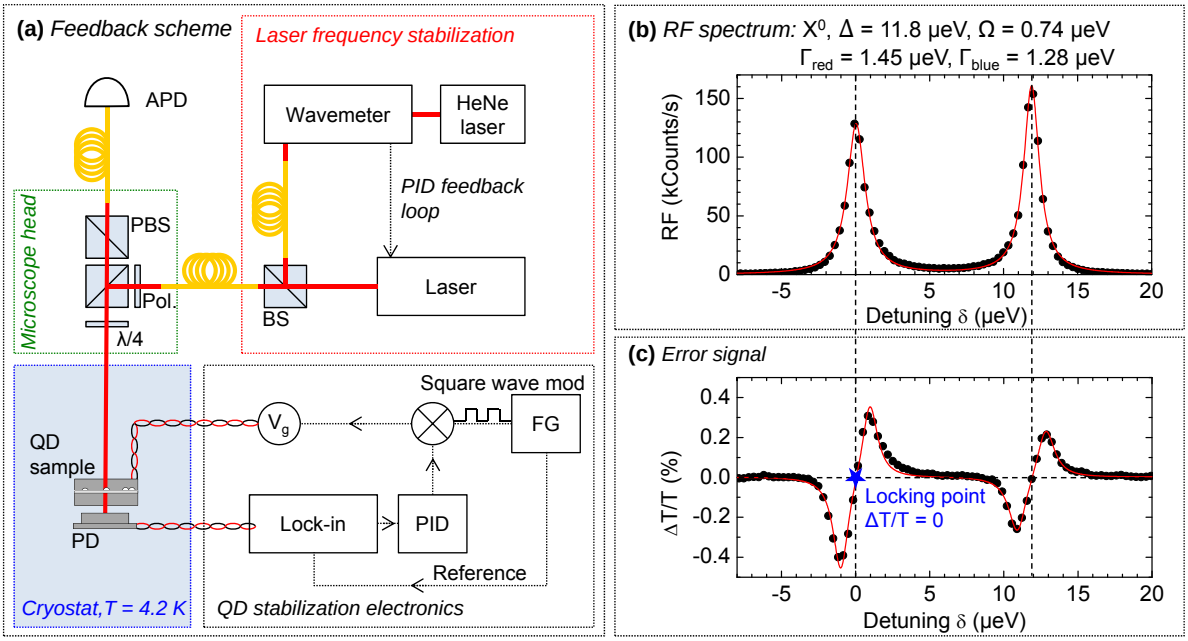

Figure 3.1 | (a) Schematic view of the experiment. The narrowband laser is stabilized to a fixed frequency by a wavemeter which in turn is stabilized to a HeNe laser. Laser light is guided through optical fibres (yellow) and microscope optics before it is focused onto the sample, driving the X^0 transition resonantly (BS = beam-splitter, PBS = polarizing BS, Pol. = linear polarizer). Two simultaneous measurements of X^0 scattering are performed: resonance fluorescence (RF), detected with an avalanche photodiode (APD) and absorption with a photodiode (PD) underneath the sample. The dynamic stabilization is realized with an active PID feedback loop which corrects for fluctuations in the transition energy using the gate voltage V_g and the square wave modulation of a function generator (FG). (b) RF signal of the fine-structure split X^0 emission of a single quantum dot at wavelength 936.5 nm, a power corresponding to a Rabi energy Ω of 0.74 µeV and a temperature of 4.2 K. A detuning is achieved by sweeping the gate voltage. The solid red line is a Lorentzian fit to the data with linewidth $\Gamma = 1.28$ µeV (309 MHz) and $\Gamma = 1.45$ µeV (350 MHz) and with a fine structure splitting $\Delta = 11.8$ µeV. (c) The differential transmission ($\Delta T/T$) signal on the same quantum dot with integration time 100 ms per point. The red curve is a fit to the derivative of the two Lorentzians. The signal around the zero crossing point ($\Delta T/T = 0$) is used to generate an error signal for the feedback scheme.

the gate electrode of the device. The set-point of the control loop is the zero crossing with the goal of locking the peak of the quantum dot RF spectrum to the laser. The laser itself is locked to a HeNe laser reference.

3.2.2 The quantum dot sample

The self-assembled InGaAs quantum dots, grown by molecular beam epitaxy, are integrated into a semiconductor charge-tunable heterostructure [33]. The quantum dots are located 25 nm above a heavily n-doped GaAs back contact ($n = 1.7 \times 10^{18}$ cm^{-3}). The intermediate layer, undoped GaAs (25 nm), acts as a tunneling barrier. A 150 nm GaAs layer caps the quantum dots and an AlAs/GaAs superlattice (68 periods of AlAs/GaAs 3 nm/1 nm) completes the heterostructure. A Ti/Au (5 nm/10 nm) Schottky gate is deposited on the sample surface; Ohmic contacts are prepared to the back contact. Bias V_g is applied between the Schottky gate and the back contact. The sample is placed in a liquid helium bath cryostat at 4.2 K with a residual magnetic field of 10 mT.

3.2.3 Single quantum dot laser spectroscopy

The single quantum dot spectroscopy is performed with a confocal microscope. The continuous wave laser has a short-term linewidth of 1 MHz. Long-term wavelength stability of ~ 2 MHz is achieved by locking the laser to a high resolution wavemeter, itself locked to a low linewidth (25 MHz) HeNe laser. The size of the focal spot and the collection efficiency of the single quantum dot RF are both enhanced with a half-sphere zirconia solid immersion lens positioned on top of the Schottky gate. Fig. 3.1(b) shows a RF signal from the neutral exciton transition, $|0\rangle \leftrightarrow |X^0\rangle$, where $|X^0\rangle$ represents an electron-hole complex and $|0\rangle$ the crystal ground state. The RF is detected with a silicon avalanche photodiode (APD) in single photon counting mode and the detuning of the quantum dot resonances relative to the constant frequency laser is achieved in this case with the Stark shift induced by the bias V_g. The X^0 exhibits a fine structure splitting of 11.8 µeV, the two lines having linewidths $\Gamma = 1.45$, 1.28 µeV close to the transform limit of $\Gamma_0 = \hbar/\tau_r = 0.93$ µeV (220 MHz) where τ_r is the radiative lifetime of the exciton transition ($\tau_r = (0.71 \pm 0.01)$ ns here).

3.2.4 Feedback loop

A sub-linewidth square-wave modulation at 527 Hz is applied to the Schottky gate. This broadens both X^0 transitions slightly, here the "red" transition from $\Gamma = 1.45$ to $\Gamma = 2.58$ µeV. The transmitted light is detected with an in situ photodiode connected to a room temperature current-voltage preamplifier. Lock-in detection of the $\Delta T/T$ signal is shown in Fig. 3.1(c).

With the sub-linewidth modulation, the $\Delta T/T$ resonance is proportional to the derivative of the RF spectrum [27]. There are two points which cross with high slope through zero, one for each X^0 transition. Both crossing points enable a feedback scheme: $\Delta T/T$ provides the error signal, V_g the control parameter. For instance, if the transition energy increases due to electric fluctuations in the sample, $\Delta T/T$ moves away from zero. Once this is detected, a modified V_g is applied to the gate to bring the resonance back to the set point. For the feedback circuit we use a PID loop. The proportional factor $P = 0.1$ is chosen with respect to the slope of the error signal, while the integral $I = 0.06$ and the derivative constant $D = 6 \times 10^{-5}$ were obtained by tuning methods. The signal:noise ratio in the $\Delta T/T$ circuit allows us to run the feedback scheme with a bandwidth up to ~ 50 Hz. The "red" X^0 transition was used for the subsequent feedback experiments because it has a higher $\Delta T/T$ contrast than the "blue" X^0 transition.

The noise in the device consists of charge noise and spin noise [18]. The charge noise power spectrum consists of $1/f$-like noise and Lorentzian noise, the latter with a characteristic frequency of ~ 10 Hz [18]. This means that the feedback bandwidth is sufficient to eliminate the low frequency drift and most of the Lorentzian noise. The spin noise power spectrum has a smaller amplitude but higher characteristic frequency, ~ 10 kHz [18], exceeding the bandwidth of the feedback.

3.3 Performance

3.3.1 Residual frequency jitter

The performance of the single quantum dot frequency stabilization is put to the test in a stroboscopic experiment. The X^0 transition energy is mapped with a second laser (linewidth also 1 MHz). The first laser stabilizes the transition with the feedback scheme at a power corresponding to a Rabi energy Ω of 0.74 µeV. A second laser of identical power is tuned with triangular function back and forth through the same transition with a rate of 8.0 µeV/s. The sum of the power of both lasers was selected to lie below the power at which power broadening becomes significant. The RF spectrum is fitted to a constant (to describe RF from the first laser) plus Lorentzian function (to describe RF from the second laser) in order to determine the center position of the resonance. In this way, a "snap-shot" of the resonance position is recorded every 5 s with "exposure time" 100 ms for a total of 1,000 s. The distribution of the peak position can be seen in the histogram in Fig. 3.2. In Fig. 3.2(a) and (b), the scanning laser results in an asymmetry: the resonance frequency is more likely to lie at positive detunings on sweeping from negative to positive detunings, and vice versa. This is probably related to the so-called "dragging" effect [34] which is very pronounced on this quantum dot at high

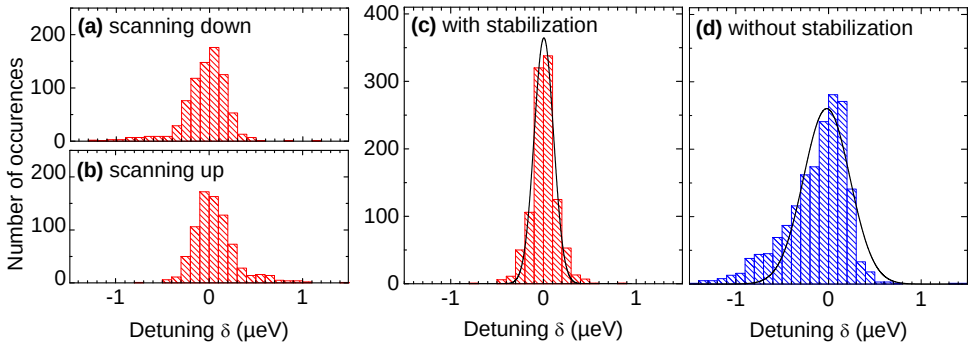

Figure 3.2 | Histogram of the RF peak position with (a, b, c) and without (d) the stabilization scheme. A triangle V_g is applied. The scanning rate of the laser is 8.0 μeV/s with period 10 s. Histograms of the RF peak position for up-sweeps (a) and down-sweeps (b) recorded with feedback. (c) shows the histogram with feedback, negative detunings from the up-sweeps, positive detunings from the down-sweeps. A histogram without feedback is shown in (d). The standard deviation σ is reduced from (d) 0.250 μeV (61 MHz) without active stabilization to (c) 0.089 μeV (22 MHz) with active stabilization.

magnetic fields (above 0.1 T) [32]: the nuclear spins polarize in such a way as to maintain the resonance with the laser over large detunings. In other words, it is likely that the asymmetries in Fig. 3.2(a) and (b) are first hints of dragging. The histogram in Fig. 3.2(c) is a combination of the data sets of (a) and (b) which are influenced least by dragging (up-sweeps at negative detuning, down-sweeps at positive detuning). Without the stabilizing loop, the long term drift, i.e. the $1/f$-like noise, results in a broader distribution, Fig. 3.2(d). This drift also leads to the asymmetry in Fig. 3.2(d), reflecting a trend to the red in this particular case. The fluctuations in resonance positions are quantified with the standard deviation σ_E of the peak positions. Without stabilization Fig. 3.2(d), $\sigma_E^{\mathrm{OFF}} = 0.250$ μeV (61 MHz). With active stabilization, $\sigma = 0.102$ μeV (25 MHz). This value is small enough to be influenced by shot noise in each data point which results in an energy uncertainty on fitting each spectrum to a Lorentzian. The shot noise results in an energy jitter of $\sigma_{E,\mathrm{shot}} = 0.049$ μeV, giving $\sigma_E^{\mathrm{ON}} = \sqrt{\sigma^2 - \sigma_{E,\mathrm{shot}}^2}$ =0.089 μeV (22 MHz), 36% of σ_E^{OFF}. The measurement of σ_E represents a measurement of the noise in a bandwidth from ~ 1 mHz to ~ 3.1 Hz. (Noise at higher frequencies is reflected in the linewidth Γ.) The ratio $\sigma_E^{\mathrm{OFF}} : \sigma_E^{\mathrm{ON}}$ would increase if lower frequencies were included on account of the $1/f$-like noise: σ_E^{ON} would remain the same but σ_E^{OFF} would increase.

The ultimate operation capability of the stabilization system is limited by the random noise in the output of the PID electronics. In Fig. 3.1(c) the noise in the $\Delta T/T$ signal is $\sigma_{\Delta T/T} = 1.45 \times 10^{-4}$. In the ideal case, this determines the energy jitter of the quantum dot resonance position [35],

$$\sigma_{E,\mathrm{min}} = \frac{d\delta}{d\Delta T}\sigma_{\Delta T/T} \simeq 0.013 \text{ μeV (3 MHz)} \tag{3.1}$$

where δ is the detuning. This limit, ~ 100 times smaller than the linewidth, illustrates the power of this technique. We have not yet reached this limit in practice. Nevertheless, stabilization with a residual jitter down to just $\sigma_E/h = 22$ MHz is achieved.

3.3.2 Noise analysis and long-term behaviour

The frequency locking feedback scheme was also tested regarding its long term behaviour and bandwidth. The RF signal was recorded over several hours, Fig. 3.3(a), without (blue) and with (red) the stabilizing loop. The measurements are accomplished by tuning the X^0 of the quantum dot via the Stark effect into resonance with the excitation laser ($\delta = 0$ µeV) and then recording the arrival time of each single photon detected by the APD over the duration of the entire experiment T. Post-experiment, the data are analyzed by setting a binning time, $t_{\text{bin}} = 100$ ms in this case. For a fixed V_g, the RF counts show large fluctuations up to a factor of 2 (blue curve). The origin are slow electrical fluctuations in the sample which cause the transition to drift out of resonance with the laser. With the feedback on, these fluctuations disappear and the RF remains at a constant level (red curve). The fluctuations in the red curve arise almost entirely from shot noise in the detector, Fig. 3.3(b). The average RF signal is a little smaller with feedback because the applied modulation broadens slightly the resonance.

Insight into the bandwidth of the stabilization mechanism is revealed by a fast Fourier transform (FFT) of the time trace. Although the shot noise dominates, the shot noise can be independently measured with a small amount of reflected laser light as a source, allowing us to determine the noise coming solely from the quantum dot. The FFT of the normalized RF signal $S(t)/\langle S(t)\rangle$ provides a noise spectrum [18]:

$$N_{\text{RF}}(f) = |\text{FFT}[S(t)/\langle S(t)\rangle]|^2 (t_{\text{bin}})^2/T. \tag{3.2}$$

For $N_{\text{RF}}(f)$, $t_{\text{bin}} = 1$ µs and $T = 2$ hours. The noise spectrum of the quantum dot $N_{\text{QD}}(f)$ is obtained by correcting the RF noise by the noise of the experiment $N_{\text{exp}}(f)$ [$N_{\text{QD}}(f) = N_{\text{RF}}(f) - N_{\text{exp}}(f)$]. $N_{\text{QD}}(f)$ corresponding to the time traces of Fig. 3.3(a) are shown in Fig. 3.3(c). Without feedback, $N_{\text{QD}}(f)$ has a $1/f$-like dependence on f as a consequence of charge noise in the device. With feedback, $N_{\text{QD}}(f)$ is reduced by up to a factor of 20 at the lowest frequencies, and is constant: the $1/f$-like noise is eliminated. The two curves meet at $f \simeq 130$ Hz once the bandwidth of the PID circuit has been exceeded. At higher frequency the noise spectrum is dominated by spin noise [18].

The two experiments, intensity noise and energy jitter measurements, can be linked to add weight to our analysis. Specifically, we forge a relationship between the RF noise under feedback and the jitter in the energy detuning, σ_E, connecting a measurement of noise in a time-trace to a separate measurement of a fluctuation in an energy detuning. The detuning jitter is much

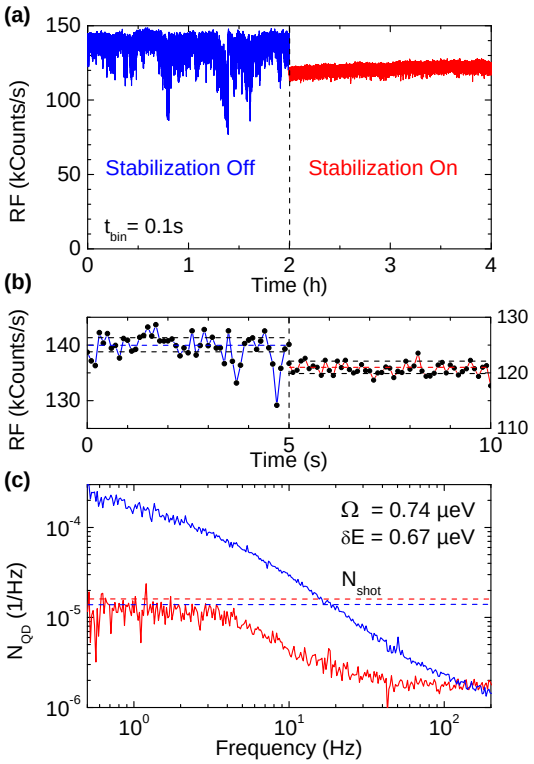

Figure 3.3 | (a) Time trace of the resonance fluorescence (RF) of a single quantum dot (the one from Fig. 3.1) with $\delta = 0$ µeV recorded over several hours. The binning time was $t_{\mathrm{bin}} = 100$ ms. The time trace is plotted with (red) and without (blue) the dynamic stabilization scheme. (b) 5 s excerpts of the unstabilized (blue) and stabilized (red) time traces with the dashed lines representing the shot noise limits. (c) Noise spectra of the normalized RF signal, $S(t)/\langle S(t)\rangle$, corresponding to the time traces of (a) after correction for external noise sources. The shot noise in the experiment is shown with the dashed lines.

less than the linewidth such that the change in the RF signal (ΔRF) is related quadratically to the detuning for fluctuations around $\delta = 0$. The variance of the RF noise, σ^2_{RF}, is related to an integral of the noise curve, $\sigma^2_{\mathrm{RF}} = \int N_{\mathrm{QD}}(f)df$ [36]. Integrating up to frequency Δf in the regime where $N_{\mathrm{QD}}(f)$ is approximately constant,

$$\sigma_E^{\mathrm{ON}} = \frac{\Gamma}{2}\left(\frac{N_{\mathrm{QD}}(0)\Delta f}{3}\right)^{\frac{1}{4}}. \tag{3.3}$$

With $\Delta f = 3.1$ Hz, $N_{\mathrm{QD}}(0) = 1.0 \times 10^{-5}$, $\Gamma = 2.58$ µeV this predicts $\sigma_E^{\mathrm{ON}} = 0.073$ µeV, in excellent agreement with the measurement from the stroboscopic experiment (0.089 µeV).

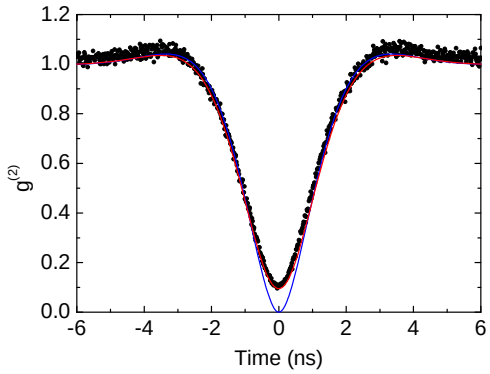

Figure 3.4 | Second-order correlation $g^2(t)$ for the stabilized RF from the X^0 (black points). The red curve shows a convolution of the two-level atom result with a Gaussian distribution which describes the timing jitter of the detectors. The blue curve shows the two-level atom response alone.

3.3.3 Single Photon Source

An intensity correlation measurement $g^{(2)}(t)$ was performed with a Hanbury Brown-Twiss interferometer. Low noise $g^{(2)}(t)$ can only be determined at these count rates (50 kHz per APD) by integrating over several hours and the feedback is therefore important to ensure that the detuning of the quantum dot with respect to the laser remains constant. $g^{(2)}(t)$ is shown in Fig. 3.4 from X^0 of the same quantum dot with zero detuning. $g^{(2)}(t)$ falls to 10% at $t = 0$. This does not reflect $g^{(2)}(0)$ of the quantum dot but rather the timing jitter of the detectors which is comparable to the radiative lifetime. We attempt to describe $g^{(2)}(t)$ with a convolution of $g^{(2)}(t)$ for an ideal two-level atom, $g^{(2)}_{\mathrm{atom}}(t)$, and the response of the detectors $G(t)$:

$$g^{(2)}(t) = g^{(2)}_{\mathrm{atom}}(t) \otimes G(t). \tag{3.4}$$

The detector response is a Gaussian function,

$$G(t) = \frac{1}{\sqrt{2\pi}\sigma_D} \exp\left(-\frac{t^2}{2\sigma_D^2}\right). \tag{3.5}$$

$g^{(2)}_{\mathrm{atom}}(t)$ of a 2-level system with resonant excitation is [37],

$$g^{(2)}_{\mathrm{atom}}(t) = 1 - \left[\cos(\lambda t) + \frac{3}{4\tau_r}\lambda \sin(\lambda t)\right] \exp\left(-\frac{3t}{4\tau_r}\right) \tag{3.6}$$

with $\lambda = (\Omega^2 - (1/4\tau_r)^2)^{1/2}$ [37].

The temporal jitter of the detector $\tau_D = 0.40$ ns is measured independently. Ω and τ_r are known from other experiments to within $10 - 20\%$ and are allowed to vary in these windows

by a fit routine. The convolution provides an excellent description of the measured $g^{(2)}(t)$ with $\Omega = (0.99 \pm 0.1)$ μeV and $\tau_r = (0.78 \pm 0.05)$ ns. In particular, with low systematic error we can set an upper bound to the quantum dot $g^{(2)}(0)$ of 1-2%.

3.4 Conclusion and Outlook

In conclusion, we have developed a dynamic method of locking the optical resonance of a single quantum dot to a stabilized laser in order to produce a stream of frequency-stabilized single photons via resonance fluorescence. Generally speaking, the scheme represents a way to reduce the local charge noise in a semiconductor.

Now that the basic principle is established, there are options for improving the feedback scheme. First, the remaining jitter in the quantum dot resonance position can be reduced by reducing the noise in the transmission detection. Presently, we are far from the limit defined by the shot noise in the detector current. With lower noise, the feedback bandwidth can also be increased. The tantalizing prospect is to create transform-limited linewidths routinely with high bandwidth feedback. A bandwidth of about 50 kHz is required [18]. Secondly, the modulation required here to generate the error signal could be eliminated in a number of ways. For instance, a dispersive lineshape can arise naturally in reflectivity via weak coupling to a cavity [38]; or the Faraday effect in a small magnetic field [39] could be used.

References

[1] C. H. Bennett and G. Brassard, in *Proceedings of IEEE International Conference on Computers, Systems & Signal Processing* (Bangalore, India, 1984) pp. 175 – 179.

[2] A. K. Ekert, Phys. Rev. Lett. **67**, 661 (1991).

[3] N. Gisin, G. Ribordy, W. Tittel, and H. Zbinden, Rev. Mod. Phys. **74**, 145 (2002).

[4] H. Bernien, B. Hensen, W. Pfaff, G. Koolstra, M. S. Blok, L. Robledo, T. H. Taminiau, M. Markham, D. J. Twitchen, L. Childress, and R. Hanson, Nature (London) **497**, 86 (2013).

[5] N. Sangouard, C. Simon, H. de Riedmatten, and N. Gisin, Rev. Mod. Phys. **83**, 33 (2011).

[6] S. Buckley, K. Rivoire, and J. Vučković, Rep. Prog. Phys. **75**, 126503 (2012).

[7] A. J. Shields, Nat. Photonics **1**, 215 (2007).

[8] B. Lounis and M. Orrit, Rep. Prog. Phys. **68**, 1129 (2005).

[9] P. Michler, A. Kiraz, C. Becher, W. V. Schoenfeld, P. M. Petroff, L. Zhang, E. Hu, and A. Imamoğlu, Science **290**, 2282 (2000).

[10] C. Santori, D. Fattal, J. Vučković, G. S. Solomon, and Y. Yamamoto, Nature (London) **419**, 594 (2002).

[11] A. Muller, E. B. Flagg, P. Bianucci, X. Y. Wang, D. G. Deppe, W. Ma, J. Zhang, G. J. Salamo, M. Xiao, and C. K. Shih, Phys. Rev. Lett. **99**, 187402 (2007).

[12] P. A. Dalgarno, J. M. Smith, J. McFarlane, B. D. Gerardot, K. Karrai, A. Badolato, P. M. Petroff, and R. J. Warburton, Phys. Rev. B **77**, 245311 (2008).

[13] K. J. Vahala, Nature (London) **424**, 839 (2003).

[14] J. Claudon, J. Bleuse, N. S. Malik, M. Bazin, P. Jaffrennou, N. Gregersen, C. Sauvan, P. Lalanne, and J.-M. Gérard, Nat. Photonics **4**, 174 (2010).

[15] A. Högele, S. Seidl, M. Kroner, K. Karrai, R. J. Warburton, B. D. Gerardot, and P. M. Petroff, Phys. Rev. Lett. **93**, 217401 (2004).

[16] M. Atatüre, J. Dreiser, A. Badolato, A. Högele, K. Karrai, and A. Imamoglu, Science **312**, 551 (2006).

[17] J. Houel, A. V. Kuhlmann, L. Greuter, F. Xue, M. Poggio, B. D. Gerardot, P. A. Dalgarno, A. Badolato, P. M. Petroff, A. Ludwig, D. Reuter, A. D. Wieck, and R. J. Warburton, Phys. Rev. Lett. **108**, 107401 (2012).

[18] A. V. Kuhlmann, J. Houel, A. Ludwig, L. Greuter, D. Reuter, A. D. Wieck, , M. Poggio, and R. J. Warburton, Nat. Phys. **9**, 570 (2013).

[19] R. J. Warburton, Nat. Mater. **12**, 483 (2013).

[20] S. T. Yilmaz, P. Fallahi, and A. Imamoğlu, Phys. Rev. Lett. **105**, 033601 (2010).

[21] K. De Greve, L. Yu, P. L. McMahon, J. S. Pelc, C. M. Natarajan, N. Y. Kim, E. Abe, S. Maier, C. Schneider, M. Kamp, S. Höfling, R. H. Hadfield, A. Forchel, M. M. Fejer, and Y. Yamamoto, Nature (London) **491**, 421 (2012).

[22] W. B. Gao, P. Fallahi, E. Togan, J. Miguel-Sanchez, and A. Imamoglu, Nature (London) **491**, 426 (2012).

[23] R. J. Warburton, C. Schulhauser, D. Haft, C. Schäflein, K. Karrai, J. M. Garcia, W. Schoenfeld, and P. M. Petroff, Phys. Rev. B **65**, 113303 (2002).

[24] A. J. Bennett, M. A. Pooley, R. M. Stevenson, M. B. Ward, R. B. Patel, A. B. de la Giroday, N. Sköld, I. Farrer, C. A. Nicoll, D. A. Ritchie, and A. J. Shields, Nat. Phys. **6**, 947 (2010).

[25] S. Seidl, M. Kroner, A. Högele, K. Karrai, R. J. Warburton, A. Badolato, and P. M. Petroff, Appl. Phys. Lett. **88**, 203113 (2006).

[26] K. D. Jöns, R. Hafenbrak, R. Singh, F. Ding, J. D. Plumhof, A. Rastelli, O. G. Schmidt, G. Bester, and P. Michler, Phys. Rev. Lett. **107**, 217402 (2011).

[27] B. Alén, F. Bickel, K. Karrai, R. J. Warburton, and P. M. Petroff, Appl. Phys. Lett. **83**, 2235 (2003).

[28] K. Karrai and R. J. Warburton, Superlattice Microst. **33**, 311 (2003).

[29] N. Akopian, R. Trotta, E. Zallo, S. Kumar, P. Atkinson, A. Rastelli, O. G. Schmidt, and V. Zwiller, arXiv:1302.2005 (2013).

[30] V. M. Acosta, C. Santori, A. Faraon, Z. Huang, K.-M. C. Fu, A. Stacey, D. A. Simpson, K. Ganesan, S. Tomljenovic-Hanic, A. D. Greentree, S. Prawer, and R. G. Beausoleil, Phys. Rev. Lett. **108**, 206401 (2012).

[31] C. Matthiesen, A. N. Vamivakas, and M. Atatüre, Phys. Rev. Lett. **108**, 093602 (2012).

[32] A. V. Kuhlmann, J. Houel, D. Brunner, A. Ludwig, D. Reuter, A. D. Wieck, and R. J. Warburton, Rev. Sci. Instrum. **84**, 073905 (2013).

[33] R. J. Warburton, C. Schäflein, D. Haft, F. Bickel, A. Lorke, K. Karrai, J. M. Garcia, W. Schoenfeld, and P. M. Petroff, Nature (London) **405**, 926 (2000).

[34] C. Latta, A. Högele, Y. Zhao, A. N. Vamivakas, P. Maletinsky, M. Kroner, J. Dreiser, I. Carusotto, A. Badolato, D. Schuh, W. Wegscheider, M. Atature, and A. Imamoglu, Nat. Phys. **5**, 758 (2009).

[35] W. Nagourney, *Quantum Electronics for Atomic Physics* (Oxford University Press, 2010).

[36] S. Kogan, *Electronic Noise and Fluctuations in Solids* (Cambridge University Press, London, 1996).

[37] R. Loudon, *The Quantum Theory of Light* (Oxford University Press, 2010) p. 358.

[38] B. Alén, A. Högele, M. Kroner, S. Seidl, K. Karrai, R. J. Warburton, A. Badolato, G. Medeiros-Ribeiro, and P. M. Petroff, Appl. Phys. Lett **89**, 123124 (2006).

[39] M. Atatüre, J. Dreiser, A. Badolato, and A. Imamoglu, Nat. Phys. **3**, 101 (2007).

Chapter 4

The positively charged exciton X^{1+}

Adapted from:

Jonathan H. Prechtel, Andreas V. Kuhlmann, Julien Houel, Arne Ludwig, Andreas D. Wieck, and Richard J. Warburton

"The positively charged exciton in a low-noise InGaAs quantum dot heterostructure"

Unpublished manuscript

Positively charged excitons X^{1+} in individual quantum dots (QDs) in a low-noise environment are probed by resonance fluorescence spectroscopy. We characterize an inverted charge tunable heterostructure design, with ultra-clean carbon doping combined with a high resolution measurement method. In this chapter we report high performance results for the single positively charged exciton, comparable to n-doped devices. More precisely, we demonstrate ultra-narrow linewidth down to 0.67 ± 0.13 μeV, reaching the transform-limit, in combination with high count rates. However, all properties are dependent on the position in the Coulomb blockade plateau. In contrast to the neutral exciton, autocorrelation measurements of the X^{1+} exhibit a bunching behaviour corresponding to on-off blinking. We model this blinking with a 3-level density matrix system, taking the on and off rates from the autocorrelation data and reproduce the noise-broadened optical linewidth and intensity variations. The results strengthen the case for implementing p-doped structures with single hole spins as qubits in quantum information processing.

4.1 Introduction

The positively charged exciton X^{1+} in a semiconductor quantum dot (QD) is formed by two heavy hole spins and one electron spin. There are many prospects for holes, primarily using the single hole spin as a spin qubit [1–4]. The main advantage that makes holes more attractive candidates than electrons is the weak hyperfine interaction with the nuclear spins [5, 6] resulting long decoherence times in the microsecond regime [7, 8].

Still, the performances of devices with holes as carriers are limping behind comparable samples with electrons [9]. So far the devices which target the investigation of the singly hole charged excitons were constructed either with holes as majority carriers, including a p-doping (C, Si or Be) in a p-i-Schottky sequence structure [7, 9] or with electrons as majority carriers in a n-i-p sequence as in Chapter 6. The QDs in these samples exhibit large linewidths, several μeV, far from the transform-limit, and low count rates. In the transform-limit the exciton linewidth is only determined by the radiative decay ($\Gamma_r = \hbar/\tau_r$ [10–12]). We introduce here a new inverted device design which enables us to have a low-noise environment, very clean quantum dots even with p-doping, and high QD emission.

In this chapter we show transform-limited linewidth for the X^{1+} combined with high resonance fluorescence emission rates. We discover and explain a voltage dependency of the charged exciton. The QD exhibits a blinking behaviour, caused by spin pumping effects. We connect the resulting on and off lifetimes with the QD emission and linewidth by a 3-level density matrix approach.

4.2 Inverted p-doped low-noise device

A main problem in highly p-doped devices is the degradation of the subsequently grown GaAs layer by the carbon dopands. The idea is to design an inverted structure, growing the p-doped layer last and therefore creating a clean region around the QDs with low fluctuations in the QD emission.

The InGaAs QDs are grown by molecular beam epitaxy in the intrinsic region of a charge tunable heterostructure device, using an In-flush technique [13]. The epitaxial gates of the n-i-p diode structure allow the control of the QD charge states [14]. Unlike previous devices [7, 9, 11], the sequence structure of the sample is inverted (see Fig. 4.1(a)). The QDs are embedded between the n-doped layer (100 nm with Si-doping level of $\sim 2.0 \times 10^{18}\,\mathrm{cm}^{-3}$) at the bottom and a p-doped layer (102 nm with C-doping level of $\sim 1.7 \times 10^{18}\,\mathrm{cm}^{-3}$, plus delta doping 10 nm $\sim 1.0 \times 10^{10}\,\mathrm{cm}^{-3}$) on top of the device. A highly opaque blocking barrier, an AlAs/GaAs short-period superlattice (71 periods of AlAs/GaAs 3 nm/1 nm), prevents the electrons from tunnelling into the active layer. The coupling between the the dots and the p-

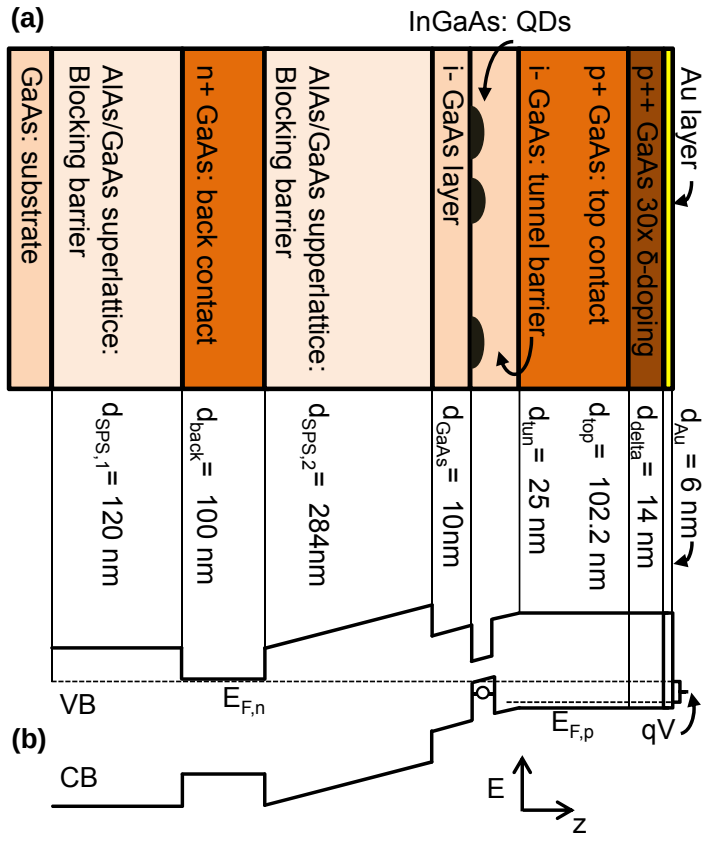

Figure 4.1 | Sample n-i-p sequence structure (a) and the corresponding energy diagram (b). The Fermi energies of the n- and the p-type niveaus are labelled.

contact is generated through a 25 nm GaAs tunnelling barrier. The top p+ GaAs is contacted with a plain 6 nm Au film, whereas an etch as deep as the n+layer with subsequent annealing of Ni/Ge/Au deposit establishes the n-contact. The background doping of as-grown GaAs is p $\sim 2.5 \times 10^{13}\,\mathrm{cm}^{-3}$; two-dimensional electron gases grown under similar conditions at 4.2 K have mobilities $> 5 \times 10^{6}\,\mathrm{cm}^{2}/\mathrm{Vs}$. The first superlattice above the substrate is deposited to lay the foundation for a pure and favourable growth of the rest of the device. The band structure of the device is illustrated in Fig. 4.1(b). The charges in the QD are controlled by the electric field. The field is generated and tuned by the voltage V, applied to the top Au layer and the electrical ground of the n+ contact.

This sample design yields several advantages. Devices can be grown in one single run: there is no need stop during the growth process after the C-doped layer to prevent diffusion and contamination of the tunnelling barrier and the active QD layer with impurities. The growing procedure bypasses the formation of trapped charges and therefore charge noise. Hence the prospect is that we have the same ultra-clean and low-noise material as in n-type samples, but

with holes as charge carriers. Furthermore the design of the device makes the top metal gate of the Schottky structures obsolete, fostering high QD emission.

High resolution resonant fluorescence spectroscopy is performed to characterize the QDs, using a homebuilt confocal microscope inside a He bath cryostat at 4.2 K. The coherent continuous wave laser with a narrow linewidth (1 MHz) addresses the individual transitions of the single QDs. The anti-bunched emission, the resonance fluorescence (RF) of the optical transitions, is separated from the reflected and scattered laser light by a polarization-based dark-field technique [15]. With a hemispherical solid immersion lens (SIL) on top of the sample the QD signal is enhanced. A single avalanche photo diode (APD) and a grating based spectrometer (resolution ~ 40 µeV) are employed for signal detection. A photodiode below the sample detects the transmitted laser light and indicates the laser power.

4.3 Characterisation of the X^{1+}

4.3.1 Photoluminescene and voltage dependence

In the beginning the charging behaviour of the QDs is investigated, by means of nonresonant (excitation laser with 830 nm) photoluminescence (PL) spectroscopy. In Fig. 4.2(a) the contour plot of a single QD illustrates the charging steps on tuning the applied bias. Every charge added or removed from the QD corresponds to an individual emission energy of the exciton due to different Coulomb interactions [12]. The overlaps in bias of the charge states are a consequence of the large hole tunnelling times, relative to the radiative emission lifetime [4]. The sophisticated and accurate method of RF spectroscopy is used to characterize the emission of the individual charging plateaus. Fig. 4.2(b) shows the narrow emission signal of the X^{1+} exciton with a transition linewidth of 2.2 µeV at plateau position of the red dashed line in Fig. 4.2(d). The linewidth of the transition Γ is determined by tuning the optical transition through a fixed excitation laser frequency. This is done via the dc-Stark effect by changing the voltage and integrating the counts with the APD for 100 ms per point. The X^{1+} linewidth is $\Omega/\Gamma_r = 0.61$ a factor of 3.3 larger than the transform-limit ($\Gamma_r^{1+} = 0.67 \pm 0.1$ µeV with $\Gamma_r = \hbar/\tau_r$ [10–12] and the Rabi energy Ω). Although the achieved linewidth is a factor of 2-3 smaller than in previous experiments [4] we are still above the transform-limit. The inhomogeneous broadening is a result of charge and spin noise [16]. The use of high quality material and resonant spectroscopy implies that spin noise, i.e. fluctuations in the Overhauser field, is the main reason for the broadening (see Chapter 5). The supposition is supported by the linewidth of the neutral exciton with 1.5 µeV ($\Omega/\Gamma_r = 0.32$) which is comparable to the high quality n-type devices in Chapter 5 and Ref. [16].

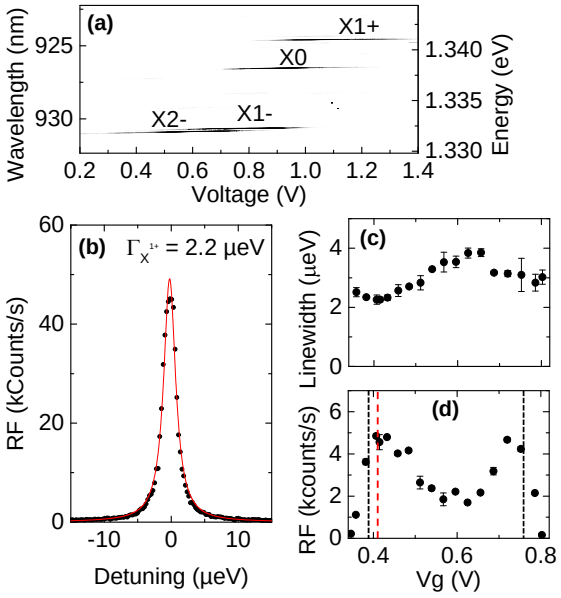

Figure 4.2 | (a) Photoluminescence contour plot of the QD as a function of the applied voltage. (b) Resonance fluorescence signal of the positively charged exciton X^{1+}, with a optical transition linewidth of 2.2 μeV, at the plateau position of the red dashed line in (d). (c) Resonant characterisation of the full X^{1+} voltage plateau, in terms of the linewidth (c) and the RF emission at the maximum of the signal (d). Dashed lines indicate the extent of the voltage plateau.

In Fig. 4.2(c) and (d) the linewidth and the maximum RF count rate are shown versus the applied voltage for the X^{1+}. The X^{1+} voltage plateau is mapped with $\Omega/\Gamma_r = 0.61$ (below the power broadening) and with the CCD camera of the spectrometer which results in a reduction of the RF counts by a factor of 10 compared to measurements with the APD. There are hints of an increase of the linewidth Γ at the edges of the plateau simultaneously with the vanishing count rate, a known feature caused by the co-tunnelling of the holes with the Fermi sea [17]. The interesting new characteristic are the two minima of the linewidth close to the edges and a maximum in the middle of the plateau. The RF signal shows the inverse behaviour. High emission is complementary to small linewidth and vice versa. This behaviour of the X^{1+} was observed on several QDs, as well as with the p-i-Schottky sample. In the following we study this behaviour and search for the connection between the emission rate and the optical linewidth.

4.3.2 Power dependence of linewidth and count rate

Further information about the single hole charged exciton (X^{1+}) is gained from the power dependencies of the linewidth and the RF count rate, shown in Fig. 4.3(a) and (b), as well as for the X^0 in (d) and (e). The measurements are performed at the favourable point of the X^{1+}

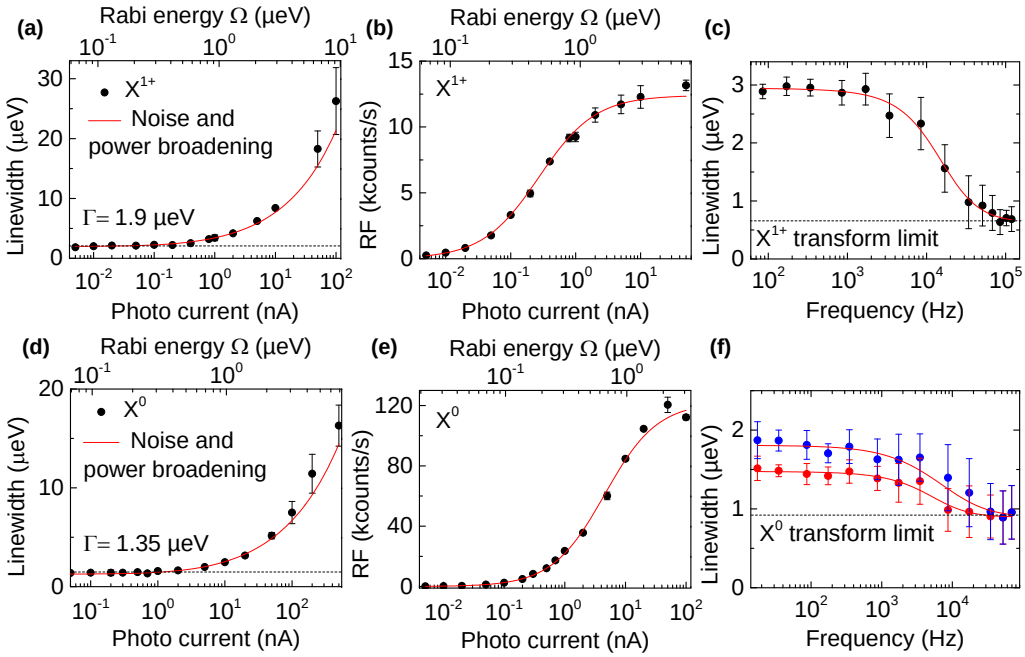

Figure 4.3 | The effect of power broadening and noise on X^{1+} and on X^0. (a) and (d) show the power dependence of the linewidth for X^{1+} and X^0, respectively. (b) and (e) depict the power dependence of the RF emission rate for X^{1+} and X^0. The data are fitted by a 2-level model including power broadening and spectral diffusion. In (c) and (f) the scanning frequency is increased, reducing the time spent on the transition itself and reducing therefore the sensitivity to the noisy environment. At high frequencies the transform-limit is reached, Γ_r, 0.92 ± 0.03 μeV and 0.68 ± 0.14 μeV for X^0 and X^{1+} respectively. The two colours in (f) correspond to the two fine-structure split transitions of the X^0.

plateau near 0.4 V to achieve the smallest possible linewidth. The data is fitted by an ideal 2-level system, including power broadening for the homogeneous broadening and the spectral diffusion term γ for the inhomogeneous broadening. Neglecting the dephasing of the upper level γ_2, the linewidth of the optical transition Γ follows [18]

$$\Gamma = \sqrt{\Gamma_r^2 + 2\Omega^2} + \gamma. \tag{4.1}$$

The population of the upper level ρ_{22} specifies the RF count rate and is derived from the density matrix formalism [18]

$$\rho_{22} = \frac{\Omega^2}{(\Gamma_r^2 + 2\Omega^2)} \cdot \frac{\Gamma - \gamma}{\Gamma}. \tag{4.2}$$

Scanning in time scales of seconds over the transition means integrating over all noise components including low frequencies. The smallest linewidth with an integration time of 100

ms/point on the transition and very low power is 1.9 ± 0.2 µeV for the X^{1+} and almost transform-limited for the X^0 with 1.35 ± 0.15 µeV. The RF emission in saturation for the X^0 is at the same Rabi coupling a factor of 3 higher than for the X^{1+}. For this p-type device, the photon emission rate of the excitonic transition, the X^0, has the same order of magnitude as for n-type devices (see Chapter 3 and Chapter 5 and [16]). Scanning the optical resonance very quickly results in reaching the transform-limit Γ_r, 0.92 ± 0.03 µeV and 0.68 ± 0.14 µeV for X^0 and X^{1+} respectively, Fig. 4.3(c) and (f). The fast scanning minimizes the time on the resonance and the charge and spin fluctuations are frozen for that period [16]. The blue and the red data correspond the two fine-structure split transitions of the neutral exciton [19].

4.3.3 Voltage dependence of the autocorrelation

The voltage dependency of the X^{1+} in Fig. 4.2 (c,d) is explored with a Hanbury Brown and Twiss interferometer, measuring the autocorrelation $g^2(t)$ of the emitted photons. At eight points of the voltage plateau (Fig. 4.4(a)) the laser frequency is stabilized onto the resonance and the anti-bunched output of single photons is measured for one hour. In Fig. 4.4(c-j) the normalized $g^2(t)$-correlations are plotted with colours matching the applied voltage in (a). The data is corrected ($g^2(t \gg 1\text{ns}) \to 1$) for the different count rates on the APDs, arising from the different plateau positions, despite the same resonant excitation power (X^{1+} with Ω/Γ_r=0.97). Correlation measurements were performed at two plateau positions for the neutral exciton as well (Fig. 4.4(b)). The striking difference is the bunching behaviour close to $\tau = \pm 1$ ns for the X^{1+} g^2 autocorrelation functions, but not for the X^0. We attribute this result to fluorescence blinking of the X^{1+}, caused by the free hole.

We consider a random two-level emitter, with an "on" and an "off" state. The emitter has an on lifetime τ_{on}, in our case the X^{1+}, and an off lifetime τ_{off}, when the emission is switched off. The part of the autocorrelation function describing the blinking behaviour is [20, 21]

$$g^2_{\text{on:off}}(\tau) = 1 + \frac{\tau_{\text{off}}}{\tau_{\text{on}}} \exp\Big[- \Big(\frac{1}{\tau_{\text{on}}} + \frac{1}{\tau_{\text{off}}} \Big) \tau \Big]. \tag{4.3}$$

A complete model of the autocorrelation function $g^2(\tau)$ consists of two parts: the antibunching of a 2-level atom under resonant excitation $g^2_{\text{atom}}(\tau)$ [18] and the additional modulation by the fluctuating function $g^2_{\text{on:off}}(\tau)$. The resulting $g^2(\tau) = g^2_{\text{atom}}(\tau) \cdot g^2_{\text{on:off}}(\tau)$ is convoluted with the Gaussian function of the detector response, which represents the detector jitter and has a FWHM of 500 ps response time on each detector. $g^2(\tau)$ fits the measurements in Fig. 4.4(c-j), taking a Rabi energy $\Omega = 0.41 \pm 0.05$ µeV and a life time of $\tau_{X^{1+}} = 0.95 \pm 0.02$ ns. The fits yield the on and off times according to Eq. 4.3, leading to the probability of being in the "on" state $\tau_{\text{on}}/(\tau_{\text{on}} + \tau_{\text{off}})$. The lower part of Fig. 4.4(a)) reveals the strong correlation between the

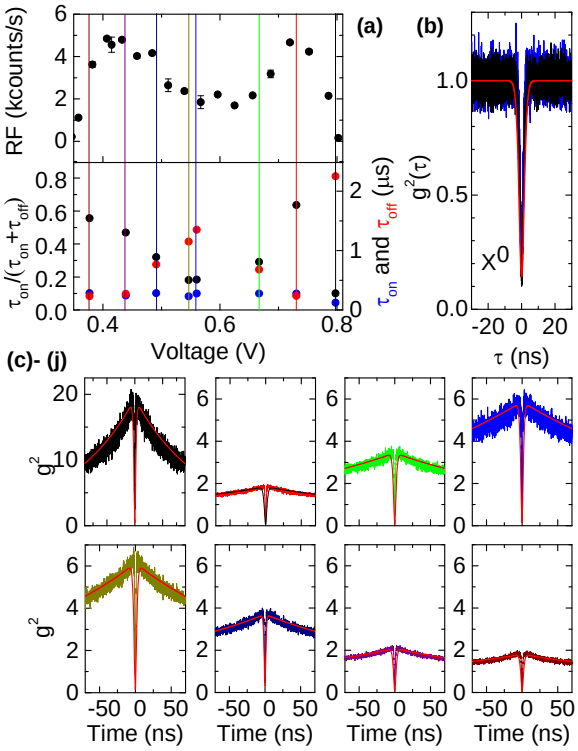

Figure 4.4 | (a) RF emission of the X^{1+} at different voltages V with the corresponding τ_{on}, τ_{off} and the on:off ratio. (b) Second order correlation function g^2 for the neutral exciton at two different voltages. The red curve describes the two level atom solution convoluted with the detector response. (c)-(j) $g^2(\tau)$-functions at discrete points over the whole plateau, with a Rabi energy $\Omega = 0.41 \pm 0.05$ µeV, a life time of $\tau_{X^{1+}} = 0.95 \pm 0.02$ ns and the FWHM of the detector response 500 ps. The colours correspond to the different voltages in (a). The fits describe the two level atom solution multiplied by an additional function to describe the bunching behaviour of the X^{1+}.

"on" probability and high X^{1+} emission. The charged exciton fluorescence is reduced, as soon as the hole has a higher probability of being lost through tunnelling at the very edges or the QD is "turned off" in the middle of the plateau. In the case of the neutral exciton the system is always in "on" state explaining the higher RF counts in saturation, as shown in Fig. 4.3(b) and (e).

4.4 Model of the blinking behaviour

The "on" and "off" state probabilities describe the RF emission along the plateau quantitatively as shown in Fig. 4.4(a). A possible consequence of the blinking on the linewidth occurs when the X^{1+} is decaying and during the spontaneous emission process the emitter turns abruptly off.

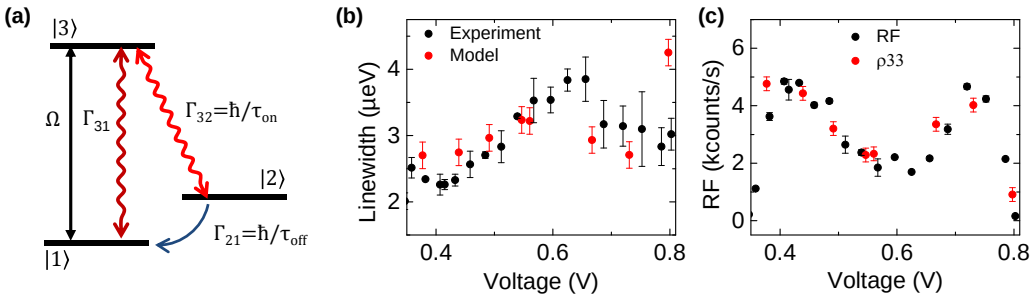

Figure 4.5 | (a) The 3-level system, connecting τ_{on} and τ_{off} with the decay rates. Linewidth (b) and RF counts (c) along the voltage plateau of the X^{1+} . The theoretical results of the density matrix formalism in red match the experimental data. The 3 level model uses a Rabi energy $\Omega = 0.61 \pm 0.1$ µeV, an exciton life time of $\Gamma_{31} = \hbar/1.05$ ms and spectral fluctuations of 1.5 µeV.

This means that this photon's wave packet is truncated leading to a wider spread in frequencies. If this happens often enough the linewidth of the emission will increase. We implement a 3-level density matrix system to demonstrate that the additional linewidth broadening is connected to the off times. The level system is shown in Fig. 4.5(a). The X^{1+} transition with the radiative decay rate Γ_{31} is described by level $|3\rangle$ (2 holes, 1 electron) and level $|1\rangle$ (one hole). The additional level $|2\rangle$ represents the "off" state. This new decay channel can be described by two decays. The decay rate $\Gamma_{32} = \hbar/\tau_{on}$ to the "off" state and the decay rate $\Gamma_{21} = \hbar/\tau_{off}$ from the "off" to the ground state. τ_{on} and τ_{off} are extracted from the fits of the autocorrelation functions. τ_{on} is voltage independent and has a value around 250 ns, whereas τ_{off} rises up to 1 µs in the middle of the plateau and decreases roughly symmetrically to the plateau edges (see Fig. 4.3(a)).

The 3-level model provides information regarding of the expected linewidth and count rate. The theoretical results (red) are in good agreement with the experimental data (black) for the linewidth and the RF signal, Fig. 4.5(b) and (c). We added a voltage independent spectral fluctuation of 1.5 µeV to the pure linewidth resulting from the model to account for the inhomogeneous broadening, which is assumed constant.

The nature of the off state is not yet explained in detail. However it is likely that the dark state is a spin-related effect. The resonant excitation pumps the system into a dark state, either an eigenstate in the x-axis (the polarization of the excitation) or a CPT-related dark state [22]. Additional experiments in an applied magnetic field and with two lasers are required to probe this further.

4.5 Conclusion and outlook

In conclusion we have shown transform-limited positively charged excitons in a high quality charge tunable structure. The narrow linewidth paves the way to use the hole spin as a highly sensitive probe for further coherent population trapping experiments. We were able to explain the voltage dependency of the emission plateau by a blinking behaviour of the X^{1+} extracting the on and off times. Finally we use a density matrix theory to connect the on and off times to the RF emission and the linewidth of the X^{1+}.

References

[1] R. J. Warburton, Nat. Mater. **12**, 483 (2013).

[2] D. V. Bulaev and D. Loss, Phys. Rev. Lett. **95**, 076805 (2005).

[3] D. V. Bulaev and D. Loss, Phys. Rev. Lett. **98**, 097202 (2007).

[4] B. D. Gerardot, D. Brunner, P. A. Dalgarno, P. Ohberg, S. Seidl, M. Kroner, K. Karrai, N. G. Stoltz, P. M. Petroff, and R. J. Warburton, Nature (London) **451**, 441 (2008).

[5] J. Fischer, W. A. Coish, D. V. Bulaev, and D. Loss, Phys. Rev. B **78**, 155329 (2008).

[6] P. Fallahi, S. T. Yilmaz, and A. Imamoğlu, Phys. Rev. Lett. **105**, 257402 (2010).

[7] D. Brunner, B. D. Gerardot, P. A. Dalgarno, G. Wüst, K. Karrai, N. G. Stoltz, P. M. Petroff, and R. J. Warburton, Science **325**, 70 (2009).

[8] K. De Greve, P. L. McMahon, D. Press, T. D. Ladd, D. Bisping, C. Schneider, M. Kamp, L. Worschech, S. Höfling, A. Forchel, and Y. Yamamoto, Nat. Phys. **7**, 872 (2011).

[9] B. D. Gerardot, R. J. Barbour, D. Brunner, P. A. Dalgarno, A. Badolato, N. Stoltz, P. M. Petroff, J. Houel, and R. J. Warburton, Appl. Phys. Lett. **99**, 243112 (2011).

[10] A. Högele, S. Seidl, M. Kroner, K. Karrai, R. J. Warburton, B. D. Gerardot, and P. M. Petroff, Phys. Rev. Lett. **93**, 217401 (2004).

[11] J. Houel, A. V. Kuhlmann, L. Greuter, F. Xue, M. Poggio, B. D. Gerardot, P. A. Dalgarno, A. Badolato, P. M. Petroff, A. Ludwig, D. Reuter, A. D. Wieck, and R. J. Warburton, Phys. Rev. Lett. **108**, 107401 (2012).

[12] P. A. Dalgarno, J. M. Smith, J. McFarlane, B. D. Gerardot, K. Karrai, A. Badolato, P. M. Petroff, and R. J. Warburton, Phys. Rev. B **77**, 245311 (2008).

[13] Z. Wasilewski, S. Fafard, and J. McCaffrey, J.Cryst. Growth **201 - 202**, 1131 (1999).

[14] R. J. Warburton, C. Schäflein, D. Haft, F. Bickel, A. Lorke, K. Karrai, J. M. Garcia, W. Schoenfeld, and P. M. Petroff, Nature (London) **405**, 926 (2000).

[15] A. V. Kuhlmann, J. Houel, D. Brunner, A. Ludwig, D. Reuter, A. D. Wieck, and R. J. Warburton, Rev. Sci. Instrum. **84**, 073905 (2013).

[16] A. V. Kuhlmann, J. Houel, A. Ludwig, L. Greuter, D. Reuter, A. D. Wieck, , M. Poggio, and R. J. Warburton, Nat. Phys. **9**, 570 (2013).

[17] J. M. Smith, P. A. Dalgarno, R. J. Warburton, A. O. Govorov, K. Karrai, B. D. Gerardot, and P. M. Petroff, Phys. Rev. Lett. **94**, 197402 (2005).

[18] R. Loudon, *The Quantum Theory of Light* (Oxford University Press, 2010) p. 358.

[19] M. Bayer, G. Ortner, O. Stern, A. Kuther, A. A. Gorbunov, A. Forchel, P. Hawrylak, S. Fafard, K. Hinzer, T. L. Reinecke, S. N. Walck, J. P. Reithmaier, F. Klopf, and F. Schäfer, Phys. Rev. B **65**, 195315 (2002).

[20] S. Machlup, J. Appl. Phys. **25**, 341 (1954).

[21] I. Sychugov, R. Juhasz, J. Linnros, and J. Valenta, Phys. Rev. B **71**, 115331 (2005).

[22] J. Hansom, C. H. H. Schulte, C. Le Gall, C. Matthiesen, E. Clarke, M. Hugues, J. M. Taylor, and M. Atatüre, Nat. Phys. **10**, 725 (2014).

Chapter 5

Transform-limited linewidth

Adapted from:

Andreas V. Kuhlmann, Jonathan H. Prechtel, Julien Houel, Arne Ludwig, Dirk Reuter, Andreas D. Wieck and Richard J. Warburton

"Transform-limited single photons from a single quantum dot"

Submitted manuscript, arXiv:1307.7109v2

Developing a quantum photonics network requires a source of very high fidelity single photons. An outstanding challenge is to produce a transform-limited single photon emitter to guarantee that single photons emitted far apart in the time domain are truly indistinguishable. This is particularly difficult in the solid-state as the complex environment is the source of noise over a wide bandwidth. A quantum dot is a robust, fast, bright and narrow-linewidth emitter of single photons; layer-by-layer growth and subsequent nano-fabrication allow the electronic and photonic states to be engineered. This represents a set of features not shared by any other emitter but transform-limited linewidths have been elusive. We report here transform-limited linewidths measured on second timescales, primarily on the neutral exciton but also on the charged exciton close to saturation. The key feature is control of the nuclear spins which dominate the exciton dephasing via the Overhauser field.

(Experiments and results presented in this chapter were obtained in close collaboration with Dr. Andreas Kuhlmann, who performed the noise experiments and the noise characterisation.)

5.1 Introduction

A single quantum dot mimics a two-level atom and single photons are generated either by spontaneous emission from the upper level [1–3] or by coherent scattering of a resonant laser [4–6]. The radiative lifetime is typically $\tau_r = 800$ ps [7]. There is evidence that on this timescale and at low temperature, there is negligible pure upper level decoherence [4–6, 8]. Photons emitted subsequently are close to indistinguishable [2, 9]. (At higher temperatures [10, 11], equivalently at low temperature but at high Rabi couplings [12, 13], phonons dephase the upper level.) A key remaining issue concerns the wandering of the centre frequency over times much longer than τ_r (Chapter 3 and [14, 15]). This wandering is highly problematic in any quantum photonics network: the emitter detunes from the common optical frequency and becomes dark; equivalently, the indistinguishability of single photons generated far apart in the time domain is reduced. Active single emitter stabilization is possible but is presently limited to correcting for very slow drifts and in any case comes at the expense of complexity (Chapter 3 and [16]). The spectral wanderings can be conveniently probed simply by measuring the optical linewidth. Measured on second time-scales, the linewidth Γ is larger than the transform-limit $\Gamma_r = \hbar/\tau_r$ [14, 15, 17, 18]. In fact single quantum dot linewidths have remained stubbornly $50 - 100\%$ above the transform-limit even under the most favourable conditions (high quality material, low temperature, charge control via Coulomb blockade, resonant excitation). We report here two regimes in which we observe transform-limited quantum dot optical linewidths even when measured on second timescales. One regime applies to the neutral exciton, X^0, the other to the charged exciton, X^{1-}.

5.2 The linewidth of the neutral and the negatively charged exciton

The X^0 transition is split into two linearly-polarized transitions by the electron-hole exchange, the so-called fine-structure, corresponding to an admixture of the spin ± 1 states, Fig. 5.1(a). The splitting between the two lines increases in an applied magnetic field, quadratically initially, Fig. 5.1(b). The magnetic field is applied externally or it arises from a net polarization in the nuclear spins which acts on the electron spin via the Overhauser field, B_N. The X^{1-} exhibits a single line at zero magnetic field, Fig. 5.1(c), splitting linearly in magnetic field, again via an external field or Overhauser field, Fig. 5.1(d). Both excitons exhibit large and similar dc Stark shifts (dependence on energy with electric field F), ~ 25 μeVcm/kV [19]. Charge noise leads to an inhomogeneous broadening of both X^0 and X^{1-} transitions via the dc Stark shift. This determines the inhomogeneous broadening for quantum dots in poor quality material or quantum dots in high quality material but with non-resonant excitation. Additionally, both excitons are sensitive to spin noise, i.e. fluctuations in the Overhauser field, but with different

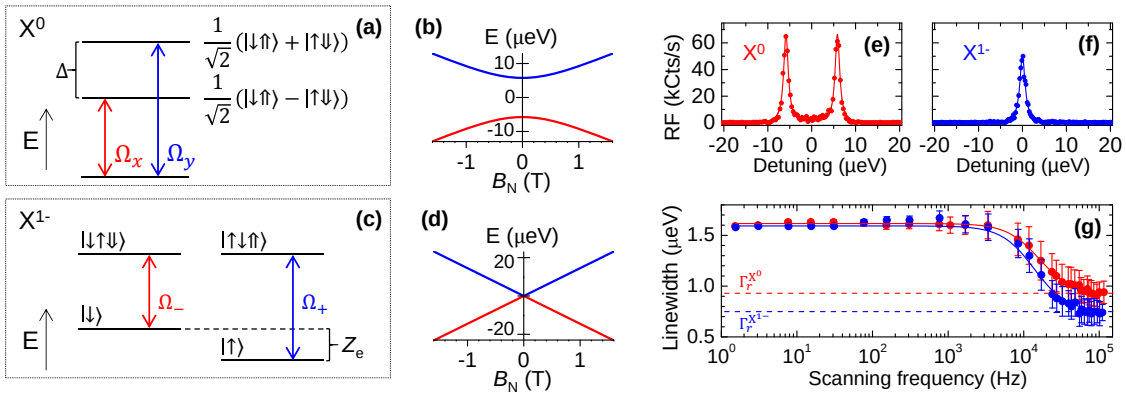

Figure 5.1 | (a) Energy levels of neutral exciton X^0 at zero magnetic field, $B = 0$, showing fine structure splitting Δ. (c) Energy levels of charged exciton X^{1-} in an Overhauser field B_N, introducing an electron Zeeman splitting Z_e. (b), (d) X^0, X^{1-} energy levels versus B_N with $\Delta = 11.5$ μeV and electron g-factor $g = -0.5$. (e), (f) X^0, X^{1-} resonance fluorescence spectra at 4.2 K, $B = 0.0$ mT with 100 ms integration time per point. The solid lines are Lorentzian fits to the data. The linewidths are $\Gamma^{X^0} = 1.29$ μeV, $\Gamma^{X^{1-}} = 1.49$ μeV; the Rabi energies $\Omega/\Gamma_r = 0.5$ (X^0), 0.4 (X^{1-}); and transform-limits $\Gamma_r^{X^0} = 0.92 \pm 0.10$ μeV, $\Gamma_r^{X^{1-}} = 0.75 \pm 0.10$ μeV. (g) RF linewidth against scanning frequency $d\delta/dt/\Gamma_r$. Γ approaches Γ_r for scanning frequencies above 50 kHz. For each scanning frequency, the error bar represents the standard deviation of several hundred linewidth scans. Solid lines represent a Lorentzian fit of the data with linewidth 30 ± 3 kHz.

sensitivities. For X^0, the sensitivity is second order as the hole "shields" the electron from the spin noise; for X^{1-} the sensitivity is first order on account of the unpaired electron in the X^{1-} ground state (See slopes in Fig. 5.1 (b) and (d)). For instance, a typical Overhauser field of 20 mT [20] (arising from incomplete cancellation of the $\sim 10^5$ nuclear spins [21, 22]) leads to a linewidth contribution in the case of X^{1-} of $\sim 0.5 - 1.0$ μeV. Experimentally, there is strong evidence that in this cold, clean limit, spin noise and not charge noise is responsible for the X^{1-} inhomogeneous broadening (see Chapter 3, Appendix A and [18]). Despite the different sensitivity to spin noise the X^0 and X^{1-} linewidths are very similar [14, 15, 18]. The approach here is to suppress the effects of charge noise by working in the ideal limit (high quality material at low temperature, resonant excitation on a quantum dot in the Coulomb blockade regime), to compare X^0 and X^{1-} on the same quantum dot, and to suppress the effects of spin noise by a search of the available parameter space.

5.2.1 Methods

The quantum dots are self-assembled using InGaAs in high purity GaAs and are embedded between an n^+ back contact (25 nm tunnel barrier) and a surface gate (see Appendix A) [15, 18]. The gate voltage V_g determines the electron occupation via Coulomb blockade [23].

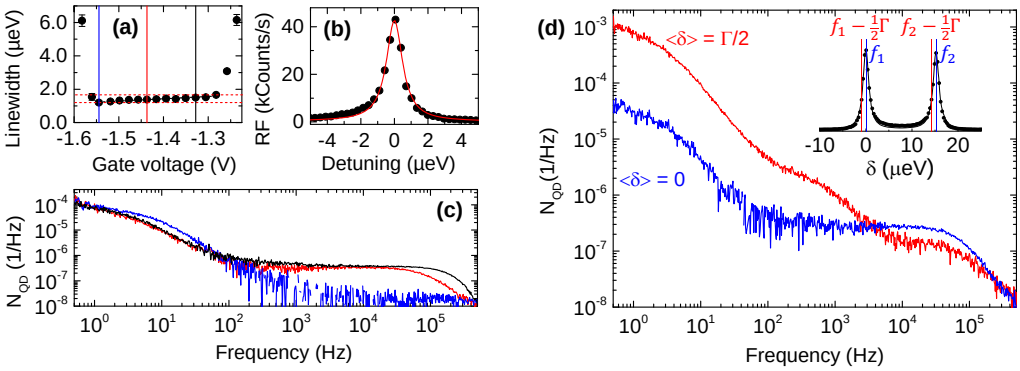

Figure 5.2 | (a) X^0 optical linewidth measured at Rabi energies $\Omega/\Gamma_r = 0.50$ for different gate voltages by sweeping the laser frequency through the resonance and integrating 100 ms per point. Γ decreases from 1.66 μeV to 1.19 μeV with decreasing gate voltage. (b) X^0 spectrum with $\Gamma = 1.15$ μeV. (c) X^0 noise spectra recorded at Rabi energies $\Omega/\Gamma_r = 0.65$ for different voltages, indicated in (a) by solid lines. Maximum/minimum spin noise (black/blue) is correlated with the largest/smallest Γ. (d) $N_{\rm QD}(f)$ on X^0 recorded with two lasers of frequencies f_1 and f_2 and a frequency splitting $f_1 - f_2$ equal to the fine structure splitting for $\langle\delta\rangle = 0$ (blue) and $\langle\delta\rangle = \Gamma/2$ (red). Inset shows the laser frequency detuning relative to the optical resonance.

We drive the optical resonance of a single quantum dot at low temperature, 4.2 K, detecting the resonance fluorescence (RF) (see Appendix A) [18, 24]. Γ is determined by sweeping the laser frequency through the resonance, integrating the counts, typically 100 ms per point. Typical X^0 and X^{1-} spectra are shown in Fig.s 5.1(e) and (f), respectively, with $\Omega/\Gamma_r = 0.5$ (X^0), 0.4 (X^{1-}). The linewidths are very similar, and are a factor of 1.4 (X^0), 2.0 (X^{1-}) larger than the transform-limit ($\Gamma_r^{X^0} = 0.92 \pm 0.10$ μeV, $\Gamma_r^{X^{1-}} = 0.75 \pm 0.10$ μeV). The transform limit Γ_r is measured by scanning the optical resonance very quickly such that the fluctuations are frozen during the measurement [18], Fig. 5.1(g).

5.2.2 Transform-limited neutral exciton

Fig. 5.2(a) shows Γ versus V_g on the neutral exciton, X^0, measured below but close to saturation, $\Omega/\Gamma_r = 0.5$. At the edges of the Coulomb blockade plateau, Γ rises rapidly on account of fast electron spin dephasing via co-tunneling with the Fermi sea [25]. This process slows down as V_g moves away from the plateau edges. The new feature is that a "sweet-spot" exists close to the negative V_g-end of the plateau with minimum linewidth 1.19 ± 0.13 μeV. Accounting for the small power broadening, the ideal limit is $\Gamma(\Omega) = \Gamma_r\sqrt{1 + 2\left(\frac{\Omega}{\Gamma_r}\right)^2} = 1.10 \pm 0.10$ μeV. Within the measurement uncertainties of 10%, the transform limit is therefore achieved. As V_g raised to the positive side of the sweet-spot, Γ increases beyond the ideal limit, Fig. 5.2(a).

5.2.3 Noise characteristics

It is instructive to investigate the sources of noise. A diagnostic is a noise spectrum $N_{\mathrm{QD}}(f)$, a Fourier transform of the RF time-trace (normalized with respect to the time-averaged signal (see Appendix A) [18]). From the known relationships between RF signal, detuning δ, Rabi coupling Ω, electric field F and the Overhauser field B_N, the variances F_{rms} and $B_{N,\mathrm{rms}}$ can be determined from the noise spectrum (see Appendix A) [18]. The increase in linewidth above the transform-limit represents a sum over all noise sources from the scanning frequency, about 1 Hz, to Γ_r, about 1 GHz. The noise spectra at the low-bias end (the sweet-spot), the centre of the plateau and the positive-bias end are shown in Fig. 5.2(c). There is a Lorentzian feature with linewidth 30 Hz (noise correlation time 30 ms) and a second Lorentzian feature at higher frequencies with linewidth 200 kHz (correlation time 5µs). The origin of the two features in the noise spectrum can be identified by exploiting the different X^0 response to charge noise and spin noise: charge noise moves both X^0 peaks rigidly together; spin noise moves them apart or closer together, a "breathing" motion. A two-laser experiment enables us to distinguish between these two possibilities. Specifically, we record X^0 noise spectra with two lasers with frequencies separated in frequency by the fine structure. On detuning both lasers from $\delta = 0$ to $\delta = \Gamma/2$, the sensitivity to charge noise increases (changing from second order to first order) yet the sensitivity to spin noise decreases (remaining second order but with a reduced pre-factor, see Appendix A). In the experiment, switching from $\langle\delta\rangle = 0$ to $\langle\delta\rangle = \Gamma/2$ causes the noise power of the low frequency component to increase markedly, Fig. 5.2(d), identifying it as charge noise. However, the frequency-sum over the charge noise gives a contribution to Γ of < 0.05 µeV (see Appendix A), a negligible value. We note that both the dc Stark coefficient and Γ vary from quantum dot to quantum dot yet there is no correlation between the two (see Appendix A), pointing also to the unimportance of charge noise in the optical linewidth. Conversely, the noise power of the high frequency component decreases on detuning both lasers from $\delta = 0$ to $\delta = \Gamma/2$, identifying it as spin noise, Fig. 5.2(d). Furthermore, noise spectra measured at $\langle\delta\rangle = 0$ but with a single laser tuned to one of the X^0 transitions show that the low frequency noise, the charge noise, is similar for all three biases yet the high frequency noise, the spin noise, increases with increasing bias, Fig. 5.2(c). This confirms that the high frequency noise, the spin noise, is responsible for the inhomogeneous linewidth: the integrated spin noise is vanishingly small at the sweet-spot, increasing at the centre of the plateau, and increasing further at the positive bias edge.

The X^0 Γ versus Ω curve does not follow exactly the text-book result for a 2-level system (see Appendix A). The Ω-dependence of $N_{\mathrm{QD}}(f)$ is highly revealing, Fig. 5.3(a). In the centre of the plateau, as Ω increases the X^0 spin noise also increases, Fig. 5.3(a). $B^{X^0}_{N,\mathrm{rms}}$ increases roughly linearly with Ω reaching at the highest couplings extremely high values, 300 mT, Fig.

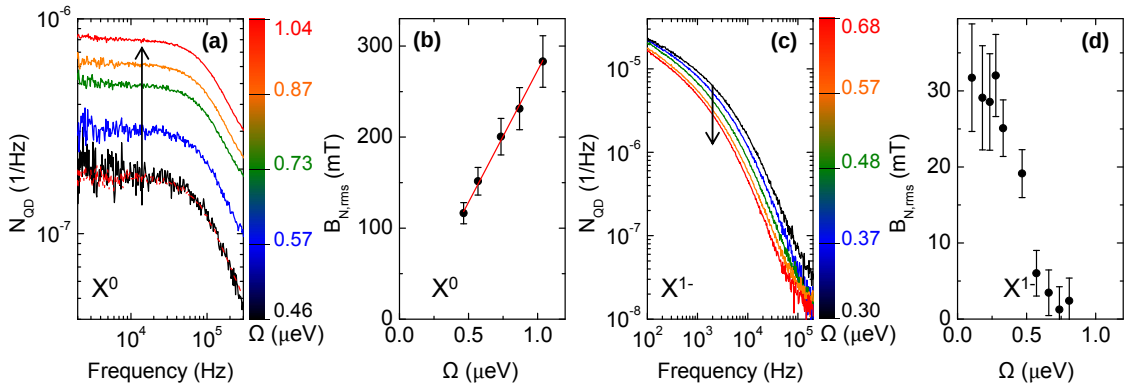

Figure 5.3 | (a) $N_{\mathrm{QD}}(f)$ on X^0 for a series of Rabi couplings Ω with V_g at the centre of the Coulomb blockade plateau at $B = 10.0$ mT. The experimental data for $\Omega = 0.46$ μeV (black curve) is accompanied by the Monte Carlo fit (red dashed curve). (c) $N_{\mathrm{QD}}(f)$ on X^{1-} for a series of Rabi couplings Ω (taken at $B = 10.0$ mT to enhance the sensitivity to spin noise [18]). (b),(d) $B_{N,\mathrm{rms}}$ versus Ω for X^0, X^{1-}.

5.3(b). ($B^{X^0}_{N,\mathrm{rms}}$ is determined by a Monte Carlo simulation of $N_{\mathrm{QD}}(f)$ including an ensemble of fluctuating nuclei – this is robust as X^0 is sensitive only to the vertical component of B_N (see Appendix A). The large $B^{X^0}_{N,\mathrm{rms}}$ would appear to prohibit transform-limited linewidths on X^0 at all but the very lowest optical couplings. However, at the sweet-spot, this mechanism is clearly suppressed: $B^{X^0}_{N,\mathrm{rms}}$ reduces to < 50 mT and approaches the value for a quantum dot in the ground-state.

We turn now to X^{1-}. In this case, it is clear that the nuclear spins are a significant source of inhomogeneous broadening. We investigate the spin noise and in particular its Ω-dependence via the noise spectra. Fig. 5.3(c) shows that the X^{1-} spin noise *decreases* as Ω increases, corresponding to a decrease in $B^{X^{1-}}_{N,\mathrm{rms}}$, Fig. 5.3(d). (The distinction between charge noise and spin noise can be made in the case of X^{1-} simply by changing the detuning from $\langle\delta\rangle = 0$ to $\langle\delta\rangle = \Gamma/2$ in a one-laser experiment [18]. X^{1-} responds to all three components of B_N, a more complex problem than that for X^0, and instead $B^{X^{1-}}_{N,\mathrm{rms}}$ is determined, Fig. 5.3(d) with lower systematic error from the 2-laser experiment described below.)

5.3 Spin noise control via a two laser experiment

We address whether the spin noise reduction in the case of X^{1-} is sufficient to achieve transform-limited optical linewidths. The Ω-dependence of $\Gamma^{X^{1-}}$ can be described extremely well with the two-level result including an inhomogeneous broadening γ, Fig. 5.4(b) (see Appendix A). At low Ω, Γ is determined by Γ_r and γ; at higher Ω, Γ increases ("power broadening") and γ becomes irrelevant. We can therefore determine the ideal limit (Γ versus Ω with $\gamma = 0$) and below saturation, the inhomogeneous broadening is clearly significant, Fig. 5.4(b). However,

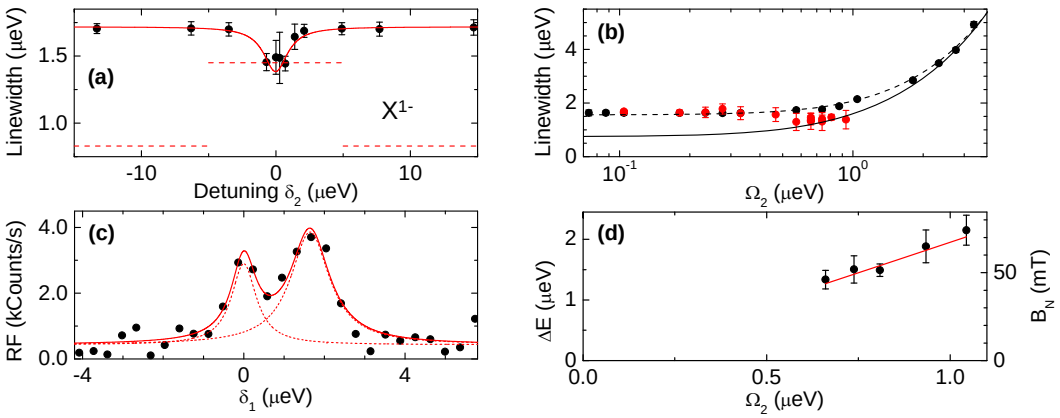

Figure 5.4 | The two-laser experiment ($B = 0.0$ mT, $T = 4.2$ K) on X^{1-}. (a) Optical linewidth measured with the probe laser ($\Omega_1 = 0.23$ μeV) versus detuning of the pump laser δ_2 for $\Omega_2 = 0.80$ μeV. The dashed lines show the ideal case (zero inhomogeneous broadening) in two limits, $\Omega = \Omega_1$ and $\Omega = \Omega_1 + \Omega_2$, appropriate for large δ_2 and $\delta_2 = 0.0$ μeV, respectively, the difference arising from power broadening. (b) Optical linewidth in one-laser experiment (black points) versus Ω with fit to 2-level model ($\gamma = 1.35$ μeV, black curve). The optical linewidth in two-laser experiment ($\Omega_1 = 0.23$ μeV, $\delta_2 = 0$) versus Ω_2 (red points). (c) Probe spectrum with $\Omega_1 = 0.23$ μeV, $\Omega_2 = 0.80$ μeV and $\delta_2 = 0.0$ μeV (points) with a two Lorentzian fit (solid line, energy separation 1.6 μeV, linewidths 0.8 ± 0.3, 1.2 ± 0.3 μeV). (e) Splitting from (d) versus Ω_2.

this relatively simple linewidth measurement is complex to interpret as the spin noise is a function of both Rabi energy and detuning. To simplify matters, we performed the experiment with two lasers. The concept is that the stronger, constant frequency pump laser (Ω_2, δ_2) determines the spin noise, and the weaker probe laser (Ω_1, δ_1) measures the optical linewidth. Fig. 5.4(a) shows $\Gamma^{X^{1-}}$ measured by sweeping δ_1 versus δ_2 for $\Omega_1 = 0.23, \Omega_2 = 0.80$ μeV. For large δ_2, the pump laser has no effect on Γ; power broadening is irrelevant and Γ is far from the transform-limit. For small δ_2 however, Γ decreases, despite the power broadening induced by Ω_2. Taking into account power broadening, Γ reduces to the ideal limit. Fig. 5.4(b) shows the results as Ω_2 increases: for $\Omega/\Gamma_r > 0.75$, transform-limited optical linewidths are achieved. The spin noise reduction on driving X^{1-} with the pump laser is accompanied by a profound change in the probe spectrum: the optical resonance now splits into two resonances, Fig. 5.4(c). The splitting reflects a static electron Zeeman splitting in the single electron ground-state, $B_N = 58$ mT in Fig. 5.4(c), with B_N increasing with Ω_2, Fig. 5.4(d). Equivalently, even without an applied magnetic field [26], a nuclear spin polarization is created by the optical coupling. This demonstrates that the laser locks the nuclear spins into an eigenstate of the ΣI_z operator. The experiments reveal a remarkable dependence of the spin noise on charge. In the centre of the plateaus, resonant excitation of X^0 enhances spin noise yet resonant optical excitation of X^{1-} suppresses spin noise. Concomitant with the different $B_{N,\mathrm{rms}}$ values are the associated B_N-correlation times, much shorter for X^0 (5 μs) than for X^{1-} (100 μs) [18, 27]. We

note that the scanning frequency dependence, Fig. 5.1(g), reveals a 100 µs noise correlation time for both X^0 and X^{1-}: at higher enough scanning frequencies, X^0 is driven too briefly for the nuclear noise process to be effective. This points to the fact that the reduced correlation time and increased amplitude of the spin noise as measured on X^0 is related to the constant optical driving. Fortunately, at a particular bias, the nuclear spin "shake-up" on driving X^0 can be turned off and transform-limited linewidths can be achieved: the charge noise is too small to matter and the electron-hole exchange shields the exciton from the remaining nuclear spin noise.

The mechanisms by which the nuclear spin noise respond to resonant optical excitation are unknown. For X^{1-}, the data are compatible with a "narrowing" of the nuclear spin distribution, perhaps caused by continuous weak measurement via the narrowband laser [28]. The correlation time is compatible with the nuclear spin dipole-dipole interaction. For X^0 it is unlikely that the standard electron spin-nuclear spin contact hyperfine interaction can offer an explanation; it is also unlikely that the bare dipole-dipole interaction can account for the short correlation time. One possibility is that the hole in the X^0 is important: a hole has a complex hyperfine interaction, containing a term $(I_+J_z + I_-J_z)$, exactly the structure required to shake-up the nuclear spins on creation of a hole (I is the nuclear spin, J the hole spin) [29]. While the coefficient of this term is likely to be small, it can have significant consequences should the dark X^0 state be occupied for times far exceeding the radiative lifetime [29]. Experimentally, dark X^0 state occupation is conceivable here, and the dark state lifetime is suppressed at the edges of the Coulomb blockade plateau [25], possibly accounting for the observed quenching of the nuclear spin shake-up. We hope that our results will stimulate a refinement in understanding of the exciton-nuclear spin interaction.

5.4 Conclusion

In conclusion, we report transform-limited optical linewidths from a single semiconductor quantum dot even when measured on second time-scales on both X^0 and X^{1-}. Generally speaking, controlling spin noise is key to operating a quantum dot-based spin qubit [21, 22, 30–32]. The same factor turns out also to be a key feature in creating a quantum dot-based high fidelity single photon source.

References

[1] P. Michler, A. Kiraz, C. Becher, W. V. Schoenfeld, P. M. Petroff, L. Zhang, E. Hu, and A. Imamoğlu, Science **290**, 2282 (2000).

[2] C. Santori, D. Fattal, J. Vučković, G. S. Solomon, and Y. Yamamoto, Nature (London) **419**, 594 (2002).

[3] A. J. Shields, Nat. Photonics **1**, 215 (2007).

[4] H. S. Nguyen, G. Sallen, C. Voisin, P. Roussignol, C. Diederichs, and G. Cassabois, Appl. Phys. Lett. **99**, 261904 (2011).

[5] C. Matthiesen, A. N. Vamivakas, and M. Atatüre, Phys. Rev. Lett. **108**, 093602 (2012).

[6] C. Matthiesen, M. Geller, C. H. H. Schulte, C. Le Gall, J. Hansom, Z. Li, M. Hugues, E. Clarke, and M. Atatüre, Nat. Commun. **4**, 1600 (2013).

[7] P. A. Dalgarno, J. M. Smith, J. McFarlane, B. D. Gerardot, K. Karrai, A. Badolato, P. M. Petroff, and R. J. Warburton, Phys. Rev. B **77**, 245311 (2008).

[8] W. Langbein, P. Borri, U. Woggon, V. Stavarache, D. Reuter, and A. D. Wieck, Phys. Rev. B **70**, 033301 (2004).

[9] O. Gazzano, S. Michaelis de Vasconcellos, C. Arnold, A. Nowak, E. Galopin, I. Sagnes, L. Lanco, A. Lemaître, and P. Senellart, Nat. Commun. **4**, 1425 (2013).

[10] M. Bayer and A. Forchel, Phys. Rev. B **65**, 041308 (2002).

[11] M. Kroner, S. Remi, A. Hoegele, S. Seidl, A. W. Holleitner, R. J. Warburton, B. D. Gerardot, P. M. Petroff, and K. Karrai, Physica E **40**, 1994 (2008).

[12] A. J. Ramsay, A. Gopal, E. M. Gauger, A. Nazir, B. W. Lovett, A. M. Fox, and M. S. Skolnick, Phys. Rev. Lett. **104**, 017402 (2010).

[13] S. M. Ulrich, S. Ates, S. Reitzenstein, A. Löffler, A. Forchel, and P. Michler, Phys. Rev. Lett. **106**, 247402 (2011).

[14] A. Högele, S. Seidl, M. Kroner, K. Karrai, R. J. Warburton, B. D. Gerardot, and P. M. Petroff, Phys. Rev. Lett. **93**, 217401 (2004).

[15] J. Houel, A. V. Kuhlmann, L. Greuter, F. Xue, M. Poggio, B. D. Gerardot, P. A. Dalgarno, A. Badolato, P. M. Petroff, A. Ludwig, D. Reuter, A. D. Wieck, and R. J. Warburton, Phys. Rev. Lett. **108**, 107401 (2012).

[16] J. Hansom, C. H. H. Schulte, C. Matthiesen, M. J. Stanley, and M. Atatüre, Appl. Phys. Lett. **105**, 172107 (2014).

[17] M. Atatüre, J. Dreiser, A. Badolato, A. Högele, K. Karrai, and A. Imamoglu, Science **312**, 551 (2006).

[18] A. V. Kuhlmann, J. Houel, A. Ludwig, L. Greuter, D. Reuter, A. D. Wieck, , M. Poggio, and R. J. Warburton, Nat. Phys. **9**, 570 (2013).

[19] R. J. Warburton, C. Schulhauser, D. Haft, C. Schäflein, K. Karrai, J. M. Garcia, W. Schoenfeld, and P. M. Petroff, Phys. Rev. B **65**, 113303 (2002).

[20] P. F. Braun, X. Marie, L. Lombez, B. Urbaszek, T. Amand, P. Renucci, V. K. Kalevich, K. V. Kavokin, O. Krebs, P. Voisin, and Y. Masumoto, Phys. Rev. Lett. **94**, 116601 (2005).

[21] I. A. Merkulov, A. L. Efros, and M. Rosen, Phys. Rev. B **65**, 205309 (2002).

[22] A. V. Khaetskii, D. Loss, and L. Glazman, Phys. Rev. Lett. **88**, 186802 (2002).

[23] R. J. Warburton, C. Schäflein, D. Haft, F. Bickel, A. Lorke, K. Karrai, J. M. Garcia, W. Schoenfeld, and P. M. Petroff, Nature (London) **405**, 926 (2000).

[24] A. V. Kuhlmann, J. Houel, D. Brunner, A. Ludwig, D. Reuter, A. D. Wieck, and R. J. Warburton, Rev. Sci. Instrum. **84**, 073905 (2013).

[25] J. M. Smith, P. A. Dalgarno, R. J. Warburton, A. O. Govorov, K. Karrai, B. D. Gerardot, and P. M. Petroff, Phys. Rev. Lett. **94**, 197402 (2005).

[26] E. A. Chekhovich, M. N. Makhonin, K. V. Kavokin, A. B. Krysa, M. S. Skolnick, and A. I. Tartakovskii, Phys. Rev. Lett. **104**, 066804 (2010).

[27] M. J. Stanley, C. Matthiesen, J. Hansom, C. Le Gall, C. H. H. Schulte, E. Clarke, and M. Atatüre, Phys. Rev. B **90**, 195305 (2014).

[28] D. Klauser, W. A. Coish, and D. Loss, Phys. Rev. B **78**, 205301 (2008).

[29] H. Ribeiro, F. Maier, and D. Loss, arXiv:1403.0490 (2014).

[30] X. Xu, B. Sun, P. R. Berman, D. G. Steel, Allan, Bracker, D. Gammon, and L. J. Sham, Nat. Phys. **4**, 692 (2008).

[31] D. Press, K. De Greve, P. L. McMahon, T. D. Ladd, B. Friess, C. Schneider, M. Kamp, S. Höfling, A. Forchel, and Y. Yamamoto, Nat. Photonics **4**, 367 (2010).

[32] R. J. Warburton, Nat. Mater. **12**, 483 (2013).

PART IV

Hole spin interaction with the environment

Chapter 6

Electric field dependence of the hole g-factor

Adapted from:

Jonathan H. Prechtel, Franziska Maier, Julien Houel, Andreas V. Kuhlmann, Arne Ludwig, Andreas D. Wieck, Daniel Loss and Richard J. Warburton

"Electrically-tunable hole g-factor of an optically-active quantum dot for fast spin rotations"

Phys. Rev. B **91**, 165304 (2015)

We report a large g-factor tunability of a single hole spin in an InGaAs quantum dot via an electric field. The magnetic field lies in the in-plane direction x, the direction required for a coherent hole spin. The electrical field lies along the growth direction z and is changed over a large range, 100 kV/cm. Both electron and hole g-factors are determined by high resolution laser spectroscopy with resonance fluorescence detection. This, along with the low electrical-noise environment, gives very high quality experimental results. The hole g-factor g_h^x depends linearly on the electric field F_z, $dg_h^x/dF_z = (8.3 \pm 1.2) \cdot 10^{-4}$ cm/kV, whereas the electron g-factor g_e^x is independent of electric field, $dg_e^x/dF_z = (0.1 \pm 0.3) \cdot 10^{-4}$ cm/kV (results averaged over a number of quantum dots). The dependence of g_h^x on F_z is well reproduced by a 4×4 k·p model demonstrating that the electric field sensitivity arises from a combination of soft hole confining potential, an In concentration gradient and a strong dependence of material parameters on In concentration. The electric field sensitivity of the hole spin can be exploited for electrically-driven hole spin rotations via the g-tensor modulation technique and based on these results, a hole spin coupling as large as ~ 1 GHz can be envisaged.

6.1 Introduction

A single electron spin in a self-assembled quantum dot (QD) is a promising candidate for a solid-state qubit [1]. In particular, the large optical dipole enables the electron spin to be initialized [2, 3], manipulated [4, 5] and read-out [6, 7] using fast optical techniques. However, the coupling of the electron spin to the nuclear spin bath of the QD via the hyperfine interaction leads to rapid spin dephasing [1, 8, 9]. A hole spin represents an alternative [1, 3, 10–13]. For a heavy-hole spin, the coefficient describing the hyperfine interaction is about one tenth that of the electron spin [14–16], and, owing to the spin $\pm\frac{3}{2}$ Bloch states, highly anisotropic such that dephasing via the nuclear spins can be suppressed with an in-plane magnetic field [14, 17]. Hole spin dephasing times T_2^* in InGaAs QDs in excess of 100 ns have been measured in small in-plane magnetic fields, Chapter 2 and [11], (although they appear to be smaller at high magnetic fields [12, 18]) and the decoherence time T_2 is in the microsecond regime [11, 12].

Electrical control of the hole spin is a tantalizing possibility. This has been pursued in the context of quantum dot molecules where a strong dependence of the hole g-factor has been discovered in the tunneling regime where bonding and anti-bonding states form [19–21]. The dependence arises from the amplitude of the hole wave function in the barrier [19, 22]. This is potentially a powerful route to developing a fully-functional spin qubit [23]. A quantum dot molecule introduces both material and spectroscopic complexity and one might wonder how far a hole spin in a single quantum dot can be developed. Theoretically there has been already extensive work on single quantum dot hole spins [14, 17, 24, 25], a proposal for fast electrical hole spin manipulation [26] and studies of the electrical tunability of the g-tensor [27–29]. Electrical control of the g-factor tensor has been explored optically via electric field control [30, 31]. However, most of the experimental studies focus on the hole g-factor with magnetic fields in growth direction.

We demonstrate here that the hole g-factor in a quantum dot is very sensitive to an electric field F (along the growth direction, z) when the magnetic field B is applied in-plane, the magnetic field direction required to generate a coherent hole spin. On the one hand, the sensitivity to electric field implies that charge noise results in hole spin dephasing (see second part of Chapter 2 and [18]). However, with quiet electrical devices, for instance the ones used here, this limitation can be overcome. On the other hand, the result enables fast electrical control of the hole spin by the g-tensor modulation technique [32, 33]: the x- and z-dependencies are different. The predicted hole spin coupling via ac electric field modulation of the g-tensor with a SiGe quantum dot is ~ 100 MHz [34]. Even larger couplings are predicted based on the results presented here.

In this paper we present a measurement method for determining the g-factor using resonant laser spectroscopy with resonance fluorescence (RF) detection [35, 36]. The method has

higher resolution than the detection of photoluminescence following non-resonant excitation. Furthermore, non-resonant excitation introduces not only electrical noise [35, 37] and hole spin dephasing (see Chapter 2) but also creates space charge which screens the applied electric field. These problems are resolved with resonant excitation. We are able to combine our high resolution resonance fluorescence experiment with a k·p theory to support our experimental results. The k·p analysis demonstrates that the origin of the large dependence of g_h^x on F_z arises from the soft hole confinement potential (allowing the "center of gravity" of the hole spin wave function to shift in a vertical electric field), an indium concentration gradient (the effective hole "composition" depends on electric field), and a strong dependence of the material parameters (notably the Luttinger parameter κ and q) on indium concentration.

6.2 Experiment

6.2.1 Sample

The quantum dots are embedded in the intrinsic region of a p-i-n device. The intrinsic region consists of a layer of self-assembled InGaAs quantum dots located between two highly opaque blocking barriers, in each case an AlAs/GaAs short-period superlattice (16 periods of AlAs/GaAs 3 nm/1 nm). An electric field F_z of more than 120 kV/cm can be applied to the QDs [38]. An etch as deep as the n^+ layer is followed by annealing Ni/Ge/Au in order to contact the n^+ GaAs; 60 nm of Au deposited directly onto the surface without annealing makes a reasonable contact to the p^+ GaAs. The n^+ layer is earthed and the electric field is controlled by applying voltage V to the top Au layer, Fig. 6.1(a). A split-coil magnet inside a He bath cryostat (4.2 K) provides a magnetic field of 3.00 T in the in-plane direction.

6.2.2 Methods

Our experimental scheme involves measuring the frequencies of the optical resonances on single QDs with high resolution laser spectroscopy. We drive the optical transitions with a coherent continuous wave laser (linewidth 1 MHz), collecting the resonance fluorescence (RF). The RF is separated from reflected and scattered laser light by a polarization-based dark-field technique [36]. RF detection is carried out with a charge-coupled device (CCD) at the output of a grating-based spectrometer (resolution $\sim$ 40 µeV). Energy tuning is performed by sweeping the transitions through the constant frequency laser, exploiting the dc Stark shift (dependence of QD optical frequency on vertical electric field). The typical linewidths are $\sim$ 5 µeV and in the spectra presented here, we can determine the peak positions with a resolution of $\pm$0.2 µeV. We study the negatively charged exciton, the X^{1-}. This is advantageous with respect to the neutral exciton, X^0, in that it exhibits no additional fine-structure splitting due to the

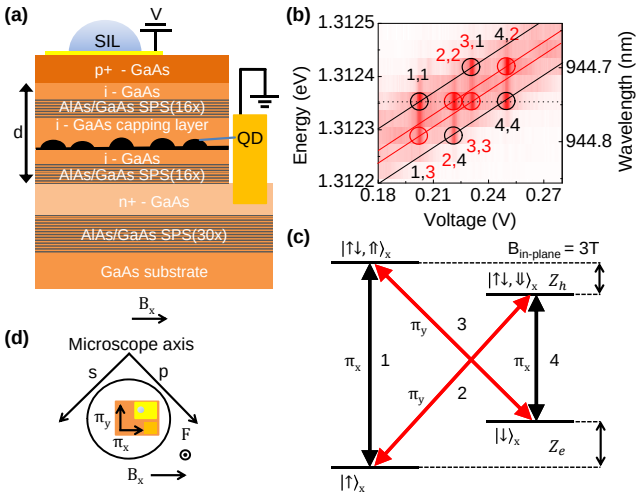

Figure 6.1 | (a) Layer sequence of the device. On top of the substrate a short-period superlattice (SPS) of AlAs/GaAs periods is grown, followed by an n^+-doped layer, an intrinsic region with a second SPS, the quantum dot layer and a third SPS, completed with a p^+ doped layer on top. On the sample surface a semi-transparent electrode is fabricated, with a hemispherical solid-immersion lens (SIL) positioned on top. (b) Contour plot of the resonance fluorescence (RF) signal as a function of the applied voltage. The charged exciton X^{1-} in an in-plane magnetic field exhibits four transitions. The four energy versus voltage dependencies are sketched with the solid lines. The dashed line represents the resonant laser frequency. RF peaks are assigned to the energy transitions with two numbers. The first number indicates the excited transition and the second the recombination channel for the emission. The transitions are indicated in (c). Red and black correspond to the diagonal and vertical transitions, respectively. The color scale is a linear representation of the CCD camera output from background counts (white) to maximum counts 1,200 cts/s (red). (c) The quantum states of a single electron spin in an in-plane magnetic field. $\uparrow$,$\downarrow$ indicate an electron spin, $\Uparrow$,$\Downarrow$ a hole spin. (d) Schematic of the sample orientation in the microscope and of the applied fields.

electron-hole exchange interaction [39]: the trion spectrum gives direct access to the electron and hole Zeeman energies, and hence g-factors. The device does not operate in the Coulomb blockade regime where the charge is precisely controlled. However, we find that X^{1-} dominates the optical spectrum in the presence of a small amount of non resonant laser light ($P_{\mathrm{NR}} = 0.75$ nW). The in-plane magnetic field along x creates a "double" Λ-system: the spin-split ground states are both coupled to the spin-split optically-excited states. The "vertical" transitions in Fig. 6.1(c) are linearly-polarized along x; the "diagonal" transitions are linearly-polarized along y. x corresponds to the [100] crystal direction. The laser is polarized along the "microscope axis" (s/p) and this corresponds closely to $\pi/4$ with respect to the x-axis such that the Rabi couplings of all four transitions are similar. Fig. 6.1(b) shows a contour plot of the RF signal, a plot of RF versus energy and V at a fixed laser frequency. The backscattered resonant laser is perfectly suppressed and is indicated via the dotted line. The applied voltage (electric field) is scanned in 0.2 mV (0.011 kV/cm) steps; the maximum count rate is 1,200 Hz in this case.

The QD emits as soon as the voltage and the laser match the energetic resonance condition. Depending on the voltage, two transitions always emit together, (1 and 3) or (2 and 4). This is the experimental signature of the "double" Λ-system. If for instance the resonant laser drives the "1"-transition (π_x-polarized), spontaneous emission takes place via the "1" recombination channel and also via the "3" recombination channel (π_y-polarized). In Fig. 6.1(b) the RF peaks are assigned to the energy transitions with two numbers. The first number indicates the excited transition and the second the recombination channel for the emission. Energy separations between peaks 1 and 3, likewise 2 and 4, determine the electron Zeeman energy; energy separations between 1 and 2, likewise 3 and 4, determine the hole Zeeman energy. These energy separations are measured at different electric fields. The applied voltage V is converted into an electric field F_z by calculating the energy band diagram of the entire p-i-n device with a one-dimensional Poisson solver [40]. To a very good approximation, $F_z = (-V + V_{bi})/d$ where d is the width of the intrinsic region and $V_{bi} = 1.52$ V is the built in potential. A positive F_z points in the positive z direction.

We should justify our assignments of the splittings which are ambiguous from the data set in Fig. 6.1 alone. We make use of the fact that the electron g-factor g_e is well known to us, both in magnitude [41] and in sign [42]: for these quantum dots it lies typically between $g_e = -0.4$ and -0.7 with no significant dependence on the direction of the magnetic field. This confirms the assignment of the $1-3$ energy splitting to the electron Zeeman energy. The corollary is that the $1-2$ splitting corresponds to the hole Zeeman energy. We find that the hole g-factor has a positive sign with values $g_h^x \simeq 0.1 - 0.3$. (The hole Zeeman energy is defined as $g_h \mu_B B$ where μ_B is the Bohr magneton, a description which assigns a pseudo spin of $\pm\frac{1}{2}$ to the hole spin.) These values are consistent with our previous measurements on similar samples with coherent population trapping (see Chapter 2 and 7 and [11]), and also measurements from other groups [12, 13, 43]. The small value of g_h^x is also consistent with simple theoretical considerations: in an in-plane magnetic field, the heavy hole g-factor is small on account of the strong valence band spin-orbit interaction [44]. We note that over the range of electric field probed here, there are no crossings or anti-crossings of the transitions.

6.3 Results

6.3.1 Electric field dependence of the g-factor

The RF spectra are recorded at different laser energies (and therefore at different electric fields) in steps of 30 μeV for high energies (1.314 eV) and 130 μeV for smaller energies (1.310 eV). Four examples are illustrated in Fig. 6.2(a-d), with laser energies at the end (a), in the middle (b,c) and at the beginning (d) of the X^{1-} emission energy range Fig. 6.2(e). Each RF-spectrum

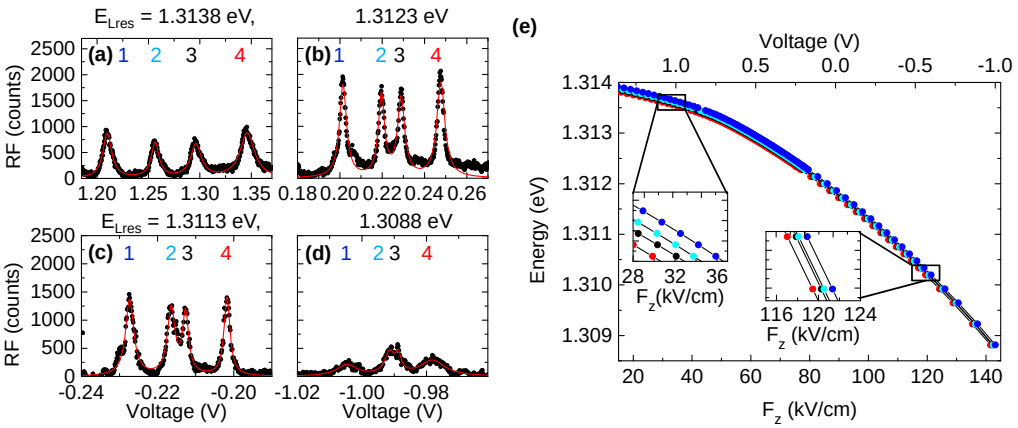

Figure 6.2 | (a)-(d) Resonance fluorescence (RF) spectra of the exciton transitions of QD1 at four fixed resonant laser energies. Detuning is achieved by tuning the voltage applied to the device. The 4 spectra are taken at different electric fields spanning the working area of the device and at an in-plane magnetic field of 3.00 T. Each of the four peaks corresponds to one of the four transitions in the quantum system (1-4, Fig. 6.1(c)). With the help of a quadruple Lorentzian function (red) the peak positions can be determined with a precision of ±0.2 µeV. (e) All RF peak positions (resonant excitation energy) versus electric field. The energies can be described in each case by a quadratic function of electric field consistent with the dc-Stark effect. The insets, both with a field extent of 9 kV/cm and an energy extent of 200 µeV, highlight the electric field dependence of the energy splittings (The colors match to the respective RF peaks (a)-(d).).

consists of four peaks corresponding to the four transitions of the quantum system (1-4). As in Fig. 6.1(b) we label the peaks 1-4 with decreasing energy and assign them to the corresponding transitions. A quadruple Lorentzian function (red) is used to fit each peak and to determine the peak position. The "fingerprint" of the spectrum changes from (a) to (d) indicating that there is a strong change in the g-factors. To convert the RF spectra versus V into a plot of g_h^x and g_e^x versus F_z, we use an intermediate step, Fig. 6.2(e). Here we plot all resonance peak positions, 1 to 4, gained from the RF spectra, as a function of F_z. Each transition is fitted to a quadratic function of F_z, $E = E_0 - pF_z + \beta F_z^2$ [45]. This corresponds to the behaviour of an electric dipole with permanent dipole moment p and polarizability β in an applied electric field. We find here $p/e = (0.033 \pm 0.002)$ nm and $\beta = -(0.234 \pm 0.002)$ µeV/(kV/cm)^2 for all four transitions. These values are compatible with the ones reported for similar devices [46]. This procedure enables us to determine E_1, E_2, E_3 and E_4 at all F_z. At a particular F_z, the energy differences enable us to make a precise measurement of the electron and the hole g-factors. With the relations $g_h^x \mu_B B = E_1 - E_2 = E_3 - E_4$ and $g_e^x \mu_B B = E_1 - E_3 = E_2 - E_4$ we determine the in-plane hole and electron g-factors, g_h^x and g_e^x, for two chosen quantum dots at different in-plane magnetic fields, Fig. 6.3.

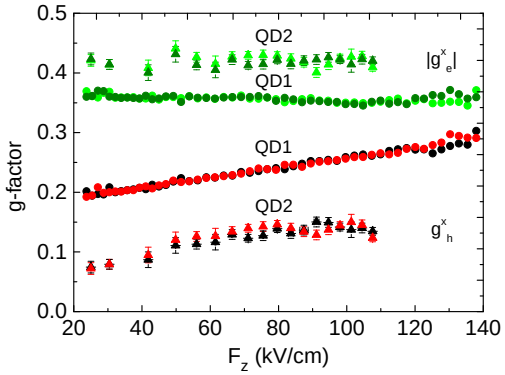

Figure 6.3 | In-plane electron g_e^x and hole g_h^x g-factors of two QDs as a function of a perpendicular electric field F_z. The electron g-factor (green and olive, $E_1 - E_3$ and $E_2 - E_4$), with a mean value of $g_e^x = -0.39 \pm 0.03$ is not influenced by the external electric field. The in-plane hole g-factor (red and black, $E_1 - E_2$ and $E_3 - E_4$) can be tuned with voltage at a rate of $dg_h^x/dF_z = (8.3 \pm 0.1) \cdot 10^{-4}$ cm/kV for QD1 (circle) and $dg_h^x/dF_z = (7.9 \pm 0.9) \cdot 10^{-4}$ cm/kV for QD2 (triangle).

We find that the electron g-factor g_e^x does not depend on the applied electric field within the sensitivity of the experiment, $dg_e/dF_z = (0.1 \pm 0.3) \cdot 10^{-4}$ cm/kV, and has an mean value of $g_e^x = -0.39 \pm 0.03$ in our sample. This is true for both quantum dots and magnetic fields up to 3.00 T. The hole g-factor g_h^x behaves completely differently: there is an approximately linear dependence on F_z. The data in Fig. 6.3 show that g_h^x of QD2 can be tuned by as much as 40% by changing the applied electric field by 120 kV/cm. A noteworthy fact is that g_h^x at any one field is highly QD-dependent yet the dependence on field, dg_h^x/dF_z, only changes slightly ($\sim$ 10%) from QD to QD. We find $dg_h^x/dF_z = (8.3 \pm 1.2) \cdot 10^{-4}$ cm/kV, a value consistent with previous estimates/measurements (see Chapter 2 and [31, 43]) where g_h^x is extracted from the energy splitting of polarization-dependent photoluminescence (Chapter 2 and [31]) and time-resolved photo-current measurements [43].

6.3.2 Theory

The electric field displaces the electron and the hole wave functions inside the QD, by values up to about 0.6 nm in this experiment. The electron wave function is more delocalized than the hole largely on account of its smaller effective mass. The electron averages over a relatively large extent and this averaging does not change significantly on displacing the electron wave function. This is likely to be the explanation for the small value of dg_e/dF_z observed experimentally [47]. However, the hole is more strongly localized and even sub-nm displacements have important consequences for g_h^x. An important point is that the QDs have an indium concentration gradient [48]. It is well known that one of the key parameters describing the hole g-factor, the Luttinger

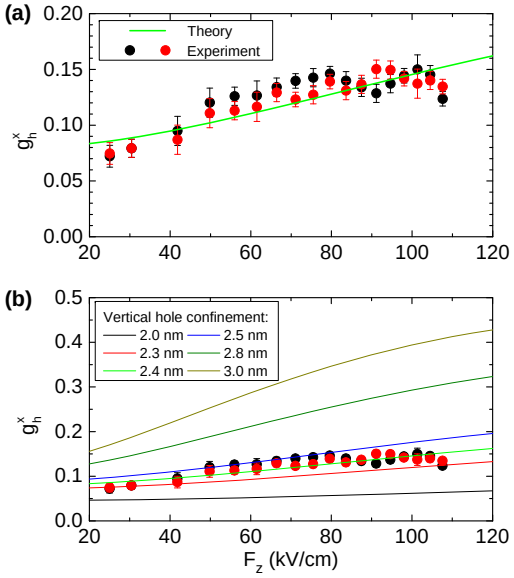

Figure 6.4 | (a) The in-plane hole g-factor for QD2 at 3.00 T. For a vertical hole confinement length of 2.4 nm the theoretical description matches the experimental data (solid green line). (b) Theoretical analysis of the electric field dependence of the in-plane hole g-factor for different values of the vertical hole confinement length.

κ-parameter, is highly dependent on indium concentration, changing from 1.1 for GaAs to 7.6 for InAs [49]. In the simplest approximation, a pure heavy-hole state has a close-to-zero in-plane g-factor: the spin is locked to the angular momentum vector which lies in the z direction by the strong spin-orbit interaction [44]. However, both the quantum dot confinement potential and the in-plane magnetic field admix the heavy-hole and light-hole states such that there is no simple result for g_h^x. Calculations with a four-band k·p theory include all the most important sources of heavy-hole, light-hole admixture and provide a quantitative explanation of our experimental results. The confinement induces coupling between the heavy-hole and light-hole states. Strain fields are of considerable strength and are taken into account. The indium content in the quantum dot is taken to be 40% at the bottom and 60% at the top. The external electric and magnetic fields are included perturbatively and the g-factor is derived from the lowest, Zeeman-split hole states. Technical details are described in the Appendix. In Fig. 6.4(a),(b) the calculated hole g-factor in a magnetic field of 3.00 T is shown as a function of vertical electric field. The results in Fig. 6.4(b) show that dg_h^x/dF_z is a strong function of the vertical confinement length of the hole and therefore the height of the quantum dot. Independent of material considerations, the lack of useful quantization limits the maximum confinement length, taken as 5 nm here. Significantly, for a realistic quantum dot confinement length of a few nm, the calculations are in good agreement with the experimental results. In fact agreement is excellent for a confinement length of 2.4 nm which is realistic for these QDs

(green line), Fig. 6.4(a). The model is very dependent on the indium concentration gradient. For realistic confinement lengths a and L, a large dg_h^x/dF_z only arises in the presence of a large In concentration gradient: this identifies the key mechanism.

6.3.3 g-tensor modulation

Additional measurements in Faraday geometry (magnetic field in growth direction) complete the picture of the hole g-factor tensor. The values we extract are $g_h^z = 1.22 \pm 0.02$ at zero electric field for the hole g-factor with an electric field dependence of $dg_h^z/dF_z = (4.1 \pm 1.0) \cdot 10^{-3}$ cm/kV. A similar slope can be found also in previous reports [30]. The dependency of the g-tensor on electric field allows the spin-up and spin-down states to be coupled by applying an ac voltage V_{ac} with a frequency equal to the Larmor frequency. The resulting coupling f_R [34] is,

$$\begin{aligned} f_R &= \frac{\mu_B V_{\mathrm{ac}}}{2h} \left[\frac{1}{g_\parallel} \left(\frac{\partial g_\parallel}{\partial V_g} \right) - \frac{1}{g_\perp} \left(\frac{\partial g_\perp}{\partial V_g} \right) \right] \\ &\quad \times \frac{g_\parallel g_\perp B_\parallel B_\perp}{\sqrt{\left(g_\parallel B_\parallel\right)^2 + \left(g_\perp B_\perp\right)^2}}. \end{aligned} \tag{6.1}$$

We estimate a value for the Rabi frequency f_R based on our results for the hole g-factor. We consider an oscillating voltage of 1 V (67 kV/cm) and a maximum driving frequency of f_{Larmor}= 20 GHz. The spin rotation is fastest when the magnetic field is applied at the "magic" angle

$$\theta_{\max} = \arctan\left(\sqrt{\frac{g_\parallel}{g_\perp}} \right), \tag{6.2}$$

in this case at 20.7° (QD1) and 14.5° (QD2) with respect to the (x, y) plane. The total magnetic field corresponds to 3.2 (4.6) T. These parameters are very reasonable in the sense that the magnetic field is not particularly high and that it lies predominantly in-plane, as required to decouple the heavy-hole spin from the nuclear spins. We obtain resulting Rabi frequencies of 350 MHz (QD1) and 1.1 GHz (QD2), the result depending strongly on the magnitude of the in-plane hole g-factor g_h^x. These very promising values exceed the ones reported for electrons in InSb nanowires [50] and holes in SiGe QDs [34].

6.4 Conclusion and Outlook

We have shown the tunability of the hole g-factor of an optically active QD in the key geometry of an in-plane magnetic field (to suppress the coupling of the hole spin to the nuclear spins) and a vertical electric field (experimentally straightforward to apply large fields, here up to 100 kV/cm). We derived the hole and electron g-factors by laser spectroscopy with res-

onance fluorescence detection. Within the resolution of the experiment, the electron g-factor is independent of the vertical electric field. Conversely, the in-plane hole g-factor is strongly dependent on the vertical electric field with $dg_h^x/dF_z = (8.3 \pm 1.2) \cdot 10^{-4}$ cm/kV. This result is explained quantitatively with a theoretical model which describes heavy-hole light-hole admixture. The origin of the strong electric field dependence arises from a combination of the softness of the hole confining potential, an indium concentration gradient and a strong dependence of material parameters on indium concentration.

A quantum dot hole spin becomes coherent in an in-plane magnetic field (see Chapter 2 and 7). On the one hand, the large dg_h^x/dF_z implies that charge noise results in hole spin dephasing. This can be minimized of course by working in the clean-material, low-temperature, resonant-excitation limit [35]. Another option, as shown by the theoretical calculations, is to work with shallow quantum dots for which dg_h^x/dF_z is small. On the other hand, the large dg_h^x/dF_z is useful: g-tensor modulation via an ac electric field can be used to drive spin rotations. With the present quantum dots we predict that the spin can be rotated at frequencies up to ~ 1 GHz. An overriding point is that the calculations show the overwhelming influence of the dot height on dg_h^x/dF_z, a powerful route to designing the hole spin properties according to the application.

References

[1] R. J. Warburton, Nat. Mater. **12**, 483 (2013).

[2] M. Atatüre, J. Dreiser, A. Badolato, A. Högele, K. Karrai, and A. Imamoglu, Science **312**, 551 (2006).

[3] B. D. Gerardot, D. Brunner, P. A. Dalgarno, P. Ohberg, S. Seidl, M. Kroner, K. Karrai, N. G. Stoltz, P. M. Petroff, and R. J. Warburton, Nature (London) **451**, 441 (2008).

[4] D. Press, T. D. Ladd, B. Zhang, and Y. Yamamoto, Nature (London) **456**, 218 (2008).

[5] D. Press, K. De Greve, P. L. McMahon, T. D. Ladd, B. Friess, C. Schneider, M. Kamp, S. Höfling, A. Forchel, and Y. Yamamoto, Nat. Photonics **4**, 367 (2010).

[6] A. N. Vamivakas, C. Y. Lu, C. Matthiesen, Y. Zhao, S. Falt, A. Badolato, and M. Atatüre, Nature (London) **467**, 297 (2010).

[7] A. Delteil, W. B. Gao, P. Fallahi, J. Miguel-Sanchez, and A. Imamoğlu, Phys. Rev. Lett. **112**, 116802 (2014).

[8] I. A. Merkulov, A. L. Efros, and M. Rosen, Phys. Rev. B **65**, 205309 (2002).

[9] A. V. Khaetskii, D. Loss, and L. Glazman, Phys. Rev. Lett. **88**, 186802 (2002).

[10] D. Heiss, S. Schaeck, H. Huebl, M. Bichler, G. Abstreiter, J. J. Finley, D. V. Bulaev, and D. Loss, Phys. Rev. B **76**, 241306 (2007).

[11] D. Brunner, B. D. Gerardot, P. A. Dalgarno, G. Wüst, K. Karrai, N. G. Stoltz, P. M. Petroff, and R. J. Warburton, Science **325**, 70 (2009).

[12] K. De Greve, P. L. McMahon, D. Press, T. D. Ladd, D. Bisping, C. Schneider, M. Kamp, L. Worschech, S. Höfling, A. Forchel, and Y. Yamamoto, Nat. Phys. **7**, 872 (2011).

[13] T. M. Godden, J. H. Quilter, A. J. Ramsay, Y. Wu, P. Brereton, S. J. Boyle, I. J. Luxmoore, J. Puebla-Nunez, A. M. Fox, and M. S. Skolnick, Phys. Rev. Lett. **108**, 017402 (2012).

[14] J. Fischer, W. A. Coish, D. V. Bulaev, and D. Loss, Phys. Rev. B **78**, 155329 (2008).

[15] P. Fallahi, S. T. Yilmaz, and A. Imamoğlu, Phys. Rev. Lett. **105**, 257402 (2010).

[16] E. A. Chekhovich, A. B. Krysa, M. S. Skolnick, and A. I. Tartakovskii, Phys. Rev. Lett. **106**, 027402 (2011).

[17] C. Testelin, F. Bernardot, B. Eble, and M. Chamarro, Phys. Rev. B **79**, 195440 (2009).

[18] A. Greilich, S. G. Carter, D. Kim, A. S. Bracker, and D. Gammon, Nat. Photonics **5**, 702 (2011).

[19] M. F. Doty, M. Scheibner, I. V. Ponomarev, E. A. Stinaff, A. S. Bracker, V. L. Korenev, T. L. Reinecke, and D. Gammon, Phys. Rev. Lett. **97**, 197202 (2006).

[20] M. F. Doty, M. Scheibner, A. S. Bracker, I. V. Ponomarev, T. L. Reinecke, and D. Gammon, Phys. Rev. B **78**, 115316 (2008).

[21] M. F. Doty, J. I. Climente, A. Greilich, M. Yakes, A. S. Bracker, and D. Gammon, Phys. Rev. B **81**, 035308 (2010).

[22] J. I. Climente, M. Korkusinski, G. Goldoni, and P. Hawrylak, Phys. Rev. B **78**, 115323 (2008).

[23] S. E. Economou, J. I. Climente, A. Badolato, A. S. Bracker, D. Gammon, and M. F. Doty, Phys. Rev. B **86**, 085319 (2012).

[24] J. I. Climente, J. Planelles, M. Pi, and F. Malet, Phys. Rev. B **72**, 233305 (2005).

[25] J. Fischer and D. Loss, Phys. Rev. Lett. **105**, 266603 (2010).

[26] D. V. Bulaev and D. Loss, Phys. Rev. Lett. **98**, 097202 (2007).

[27] C. E. Pryor and M. E. Flatté, Phys. Rev. Lett. **96**, 026804 (2006).

[28] J. Pingenot, C. E. Pryor, and M. E. Flatté, Appl. Phys. Lett. **92**, 222502 (2008).

[29] J. van Bree, A. Y. Silov, P. M. Koenraad, M. E. Flatté, and C. E. Pryor, Phys. Rev. B **85**, 165323 (2012).

[30] V. Jovanov, T. Eissfeller, S. Kapfinger, E. C. Clark, F. Klotz, M. Bichler, J. G. Keizer, P. M. Koenraad, G. Abstreiter, and J. J. Finley, Phys. Rev. B **83**, 161303 (2011).

[31] A. J. Bennett, M. A. Pooley, Y. Cao, N. Sköld, I. Farrer, D. A. Ritchie, and A. J. Shields, Nat. Commun. **4**, 1522 (2013).

[32] G. Salis, Y. Kato, K. Ensslin, D. C. Driscoll, A. C. Gossard, and D. D. Awschalom, Nature (London) **414**, 619 (2001).

[33] Y. Kato, R. C. Myers, D. C. Driscoll, A. C. Gossard, J. Levy, and D. D. Awschalom, Science **299**, 1201 (2003).

[34] N. Ares, G. Katsaros, V. N. Golovach, J. J. Zhang, A. Prager, L. I. Glazman, O. G. Schmidt, and S. De Franceschi, Appl. Phys. Lett. **103**, 263113 (2013).

[35] A. V. Kuhlmann, J. Houel, A. Ludwig, L. Greuter, D. Reuter, A. D. Wieck, , M. Poggio, and R. J. Warburton, Nat. Phys. **9**, 570 (2013).

[36] A. V. Kuhlmann, J. Houel, D. Brunner, A. Ludwig, D. Reuter, A. D. Wieck, and R. J. Warburton, Rev. Sci. Instrum. **84**, 073905 (2013).

[37] J. Houel, A. V. Kuhlmann, L. Greuter, F. Xue, M. Poggio, B. D. Gerardot, P. A. Dalgarno, A. Badolato, P. M. Petroff, A. Ludwig, D. Reuter, A. D. Wieck, and R. J. Warburton, Phys. Rev. Lett. **108**, 107401 (2012).

[38] A. J. Bennett, M. A. Pooley, R. M. Stevenson, M. B. Ward, R. B. Patel, A. B. de la Giroday, N. Sköld, I. Farrer, C. A. Nicoll, D. A. Ritchie, and A. J. Shields, Nat. Phys. **6**, 947 (2010).

[39] M. Bayer, G. Ortner, O. Stern, A. Kuther, A. A. Gorbunov, A. Forchel, P. Hawrylak, S. Fafard, K. Hinzer, T. L. Reinecke, S. N. Walck, J. P. Reithmaier, F. Klopf, and F. Schäfer, Phys. Rev. B **65**, 195315 (2002).

[40] 1D Poisson/Schrödinger solver program developed by Dr. Gregory Snider, http://www.nd.edu/ gsnider/.

[41] M. Kroner, K. M. Weiss, B. Biedermann, S. Seidl, S. Manus, A. W. Holleitner, A. Badolato, P. M. Petroff, B. D. Gerardot, R. J. Warburton, and K. Karrai, Phys. Rev. Lett. **100**, 156803 (2008).

[42] A. Högele, M. Kroner, S. Seidl, K. Karrai, M. Atatüre, J. Dreiser, A. Imamoğlu, R. J. Warburton, A. Badolato, B. D. Gerardot, and P. M. Petroff, Appl. Phys. Lett. **86**, 221905 (2005).

[43] T. M. Godden, J. H. Quilter, A. J. Ramsay, Y. Wu, P. Brereton, I. J. Luxmoore, J. Puebla, A. M. Fox, and M. S. Skolnick, Phys. Rev. B **85**, 155310 (2012).

[44] R. W. Martin, R. J. Nicholas, G. J. Rees, S. K. Haywood, N. J. Mason, and P. J. Walker, Phys. Rev. B **42**, 9237 (1990).

[45] R. J. Warburton, C. Schulhauser, D. Haft, C. Schäflein, K. Karrai, J. M. Garcia, W. Schoenfeld, and P. M. Petroff, Phys. Rev. B **65**, 113303 (2002).

[46] A. J. Bennett, R. B. Patel, J. Skiba-Szymanska, C. A. Nicoll, I. Farrer, D. A. Ritchie, and A. J. Shields, Appl. Phys. Lett. **97**, 031104 (2010).

[47] J. Pingenot, C. E. Pryor, and M. E. Flatté, Phys. Rev. B **84**, 195403 (2011).

[48] V. Mlinar, M. Bozkurt, J. M. Ulloa, M. Ediger, G. Bester, A. Badolato, P. M. Koenraad, R. J. Warburton, and A. Zunger, Phys. Rev. B **80**, 165425 (2009).

[49] N. J. Traynor, R. T. Harley, and R. J. Warburton, Phys. Rev. B **51**, 7361 (1995).

[50] J. W. G. van den Berg, S. Nadj-Perge, V. S. Pribiag, S. R. Plissard, E. P. A. M. Bakkers, S. M. Frolov, and L. P. Kouwenhoven, Phys. Rev. Lett. **110**, 066806 (2013).

Chapter 7

The decoupling of the hole spin from the nuclear spins

Adapted from:

Jonathan H. Prechtel, Andreas V. Kuhlmann, Julien Houel, Arne Ludwig, Andreas D. Wieck and Richard J. Warburton

"The hole spin qubit: decoupling from the nuclear spins"

Submitted manuscript

A huge effort is underway to develop semiconductor nanostructures as low noise hosts for qubits. The main source of dephasing of an electron spin qubit in GaAs is the nuclear spin bath. A hole spin may circumvent the nuclear spin noise. In principle, the nuclear spins can be switched off for a pure heavy-hole spin. In practice, it is unknown to what extent this ideal limit can be achieved. A major hindrance is that p-type devices are often far too noisy. We investigate here a single hole spin in an InGaAs quantum dot embedded in a new generation of low-noise p-type device. We measure the hole Zeeman energy in a transverse magnetic field with 10 neV resolution by dark state spectroscopy as we create a large transverse nuclear spin population. The hole hyperfine interaction is highly anisotropic: the transverse coupling is $< 1\%$ of the longitudinal coupling. For unpolarized, randomly fluctuating nuclei, the ideal heavy-hole limit is achieved down to neV energies; equivalently dephasing times up to a µs. The combination of large T_2^* and strong optical dipole make the single hole spin in GaAs an attractive quantum platform.

7.1 Hole spin hyperfine interaction

The electron states in a self-assembled quantum dot, Fig. 7.1(a), are constructed from atomic s orbitals, Fig. 7.1(b). The large amplitude of the s orbital at the location of each nucleus i results in a Fermi contact hyperfine interaction for an electron spin $\mathbf{S}$ with N nuclear spins $\mathbf{I}_i$

$$\hat{H}_{\text{contact}} = \sum_{i=1}^{N} A_i^e |\psi_i|^2 \mathbf{I}_i \cdot \mathbf{S} = \sum_{i=1}^{N} A_i^e |\psi_i|^2 \left[I_i^z S^z + \frac{1}{2} \left(I_i^+ S^- + I_i^- S^+ \right) \right]. \tag{7.1}$$

A_i^e is the coupling coefficient and ψ_i the envelope function. This interaction dominates the electron spin dephasing. The nuclei create an effective magnetic field, the Overhauser field B_N, which fluctuates in time resulting in spin dephasing [1, 2]. For self-assembled quantum dots, $N \sim 10^5$, $B_N \sim 20$ mT resulting in an energy fluctuation in the electron Zeeman energy of $\delta Z_e \simeq 0.6$ µeV and $T_2^* \sim 1$ ns. This dephasing can only be suppressed by "narrowing" the nuclear spin distribution, ideally preparing the nuclei in a z-eigenstate.

A hole is the absence of an electron in an otherwise occupied valence level. A hole spin has a fundamentally different hyperfine interaction to the electron spin. The valence states are constructed from atomic p orbitals with zero wavefunction amplitude at the location of the nuclei, Fig. 7.1(b). The Fermi contact hyperfine interaction is therefore suppressed [3, 4]. The dipole-dipole part of the hyperfine interaction remains [3, 5, 6]. For a *pure* heavy-hole (HH) state the hyperfine interaction has an Ising-form

$$\hat{H}_{\text{dipole}}^{HH} = \sum_{i=1}^{N} A_i^{HH,z} |\psi_i|^2 I_i^z J^z. \tag{7.2}$$

Such that the heavy-hole spin J experiences just the z-component of the noisy Overhauser field. Furthermore, the coupling coefficients are reduced: $A_i^{HH,z}/A_i^e \sim -10\%$ [3, 6]. The most important consequence of the Ising-form is that application of a transverse magnetic field suppresses hole spin dephasing by the nuclear spins [3]. This is so effective that the hyperfine interaction is to all intents and purposes switched off for a *pure* heavy hole spin [7].

In practice, a *real* hole state is inevitably an admixture of heavy-hole, light-hole, spin-orbit split-off and conduction states such that the hyperfine interaction is no longer purely Ising-like:

$$\hat{H}_{\text{dipole}}^{h} = \sum_{i=1}^{N} |\psi_i|^2 \left[A_i^{h,z} I_i^z J^z + \frac{1}{2} A_i^{h,\perp} \left(I_i^+ J^- + I_i^- J^+ \right) \right]. \tag{7.3}$$

$A_i^{h,\perp}$ is the transverse part and arises from the admixture of both conduction [7, 8] and light-hole states [6–8]. Furthermore, in this 2-fold pseudo spin-basis for the hole, admixture of the

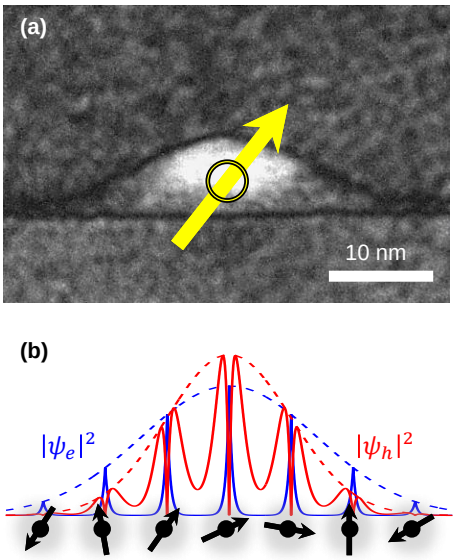

Figure 7.1 | Electron and hole wavefunctions. (a) TEM image of a self-assembled quantum dot (TEM performed by Jean-Michel Chauveau and Arne Ludwig). (b) Schematic of the electron and hole states. The electron state is constructed largely from atomic s orbitals, each localized to a unit cell (blue line) modulated by the envelope function that extends over the quantum dot (dashed line). In contrast, the hole state is constructed largely from atomic p orbitals (red line). The probability density for an electron to reside at the location of the nuclei (black circles) is therefore large for an electron, small for a hole. ψ_e and ψ_h denotes the envelope function for the electron, hole respectively.

light-holes leads in addition to "non-colinear" terms $(I_i^+ + I_i^-)J_z$ [9, 10] and to terms with form $(I_i^+ J^+ + I_i^- J^-)$ [10].

Experiments have established long hole spin relaxation times [11, 12], coherence times T_2 in the µs range [13, 14], fast spin rotations [14–16] and control of two tunnel-coupled hole spin qubits [15]. The existence of the dipole-dipole hyperfine interaction has been established [5]. Experimentally, $A_i^{h,z}$ has been measured to be -10% of A_i^e on self-assembled quantum dots by dynamically polarizing the nuclear spins along the z-direction and measuring the changes to the electron and hole Zeeman energies [17–19], confirming theoretical expectations [3, 6] albeit with some interesting discussion on the sign [20]. However, the full topology of the hole hyperfine interaction has not yet been determined: it is presently unclear if the heavy-hole limit can be reached with available quantum dots. We stress that the anisotropy (rather than the magnitude of $A_i^{h,z}$) is the crucial question in the development of a hole spin qubit.

Two difficulties are encountered in probing the hole spin hyperfine interaction optically. First, optical excitation of a hole spin populates an exciton state consisting of two holes in a singlet state but an unpaired electron spin. In this situation it is not trivial to assign any nuclear spin effects unambiguously to the hole spin given the strong hyperfine interaction of

the electron spin. Secondly, p-type devices tend to be considerably noisier than n-type devices yet the hole g-factor is very sensitive to an electric field (Chapter 2, Chapter 6 and [21]) such that charge noise results in spin dephasing (Chapter 2, Chapter 6 and [14]): in noisy devices this effect can completely obscure the hyperfine couplings.

7.2 Coherent population trapping experiment

7.2.1 Method

Here we determine the topology of the hole hyperfine interaction in a self-assembled quantum dot and uncover an extremely high anisotropy, i.e. close-to-Ising-like, $|A_i^{h,\perp}| \ll |A_i^{h,z}|$. We polarize the nuclear spins along a transverse direction, monitoring the polarization via the lone electron spin in the exciton, and measure the hole Zeeman splitting Z_h ultra-precisely by means of dark-state spectroscopy, i.e. coherent population trapping (CPT) (see Chapter 2 and [13, 22–24]). We exploit the coherence of the hole spin, resonance fluorescence detection (RF) [25] and low-noise samples to achieve a spectral resolution in Z_h of just 10 neV (2.4 MHz).

CPT is a quantum interference in a Λ-system where two ground states are coupled individually by "pump" and "probe" optical fields to a common upper level, Fig. 7.2(a). Here, the two ground states correspond to the Zeeman-split hole spin states, $|\Uparrow\rangle_x$ and $|\Downarrow\rangle_x$, and the upper level to an exciton, $|\Uparrow\Downarrow,\downarrow\rangle_x$ or $|\Uparrow\Downarrow,\uparrow\rangle_x$ (where $|\uparrow\rangle_x, |\downarrow\rangle_x$ refer to the electron spin states), Fig. 7.2(a). A transverse magnetic field (in the x-direction) establishes the quantization axis and the Λ-system, Fig. 7.2(a). The interference occurs when the frequency difference of the lasers matches the hole Zeeman splitting, the two-photon resonance. A dark state results, revealed by a dip in the probe spectrum. The spectral position of the dip measures Z_h. Specifically, when $\hbar\Omega_1 \ll \hbar\Omega_2 \ll \hbar\Gamma_r$ ($\hbar\Omega_1$, $\hbar\Omega_2$ are the probe and pump couplings, Γ_r the spontaneous emission rate) the CPT dip has width $\hbar\Omega_2^2/\Gamma_r$. The depth of the dip is sensitive to the hole spin coherence: for $1/T_2 \ll \Omega_2^2/\Gamma_r$ the emission in the dip goes to zero. Therefore, provided the hole spin coherence is high enough, the width of the CPT dip can be much less than the optical linewidth, enabling a highly accurate measurement of Z_h. Furthermore, the location of the CPT dip is determined only by the two-photon resonance. CPT is therefore an ideal technique to extract Z_h. Fluctuations in exciton energy (via charge noise and the Overhauser field acting on the electron spin) modify the emission envelope [13, 22] but not the location of the CPT dip.

7.2.2 Ultra-narrow and high signal:noise CPT dip

CPT on a single quantum dot containing a single hole is shown in Fig. 7.2(b). The results are recorded on a new generation of low-noise p-type devices. The low noise is revealed in

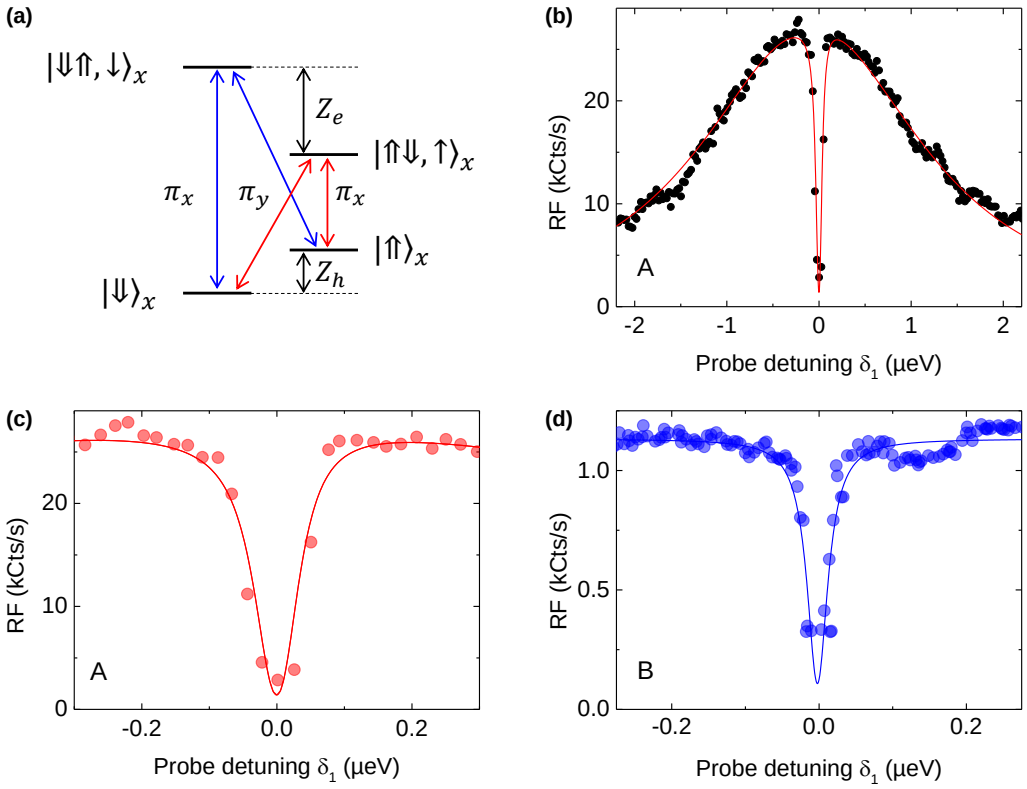

Figure 7.2 | (a) The quantum states. Two optical Λ-systems (blue and red lines) are established in a magnetic field along the x-direction: $|\Uparrow\rangle_x$ and $|\Downarrow\rangle_x$ are the hole spin eigenstates in the x-basis, split by the Zeemann energy Z_h; the upper levels are the X^{1+} excitons consisting of two holes in a singlet state and an unpaired electron with spin $\pm\frac{1}{2}$, again in the x-basis. The optical transitions are linearly polarized, either π_x or π_y, with equal optical dipoles, at wavelengths close to 950 nm. (b) RF spectrum on a single quantum dot QDA containing a single hole in sample A using the "blue" Λ-system (pump on higher energy "vertical" transition). The pronounced dip signifies CPT. The frequency of the probe laser is scanned and is plotted with respect to the CPT dip. The solid line shows the result of a 3-level density matrix model (probe coupling $\hbar\Omega_1 = 0.06$ μeV, pump coupling $\hbar\Omega_2 = 0.40$ μeV, spontaneous emission rate $\Gamma_r = 0.68$ μeV, $T_2 > 1$ μs, $T_1 \gg T_2$) convoluted with a Lorentzian with FWHM $\Gamma = 2.5$ μeV to describe slow exciton dephasing, and then with a Lorentzian with FWHM 8.3 neV (2.0 MHz) to account for the mutual coherence of the lasers (see Supplementary Information). The data were recorded with 0.1 s integration time per point at a magnetic field $B_x = 3.00$ T and temperature $T = 4.2$ K. (c),(d) Two exemplary CPT dips from a quantum dot in sample A and in sample B, respectively. The dip from sample A has FWHM of 80 neV (19.3 MHz) and is modelled with the parameters of (b). The limited mutual coherence of the lasers is the main reason that the signal in the dip centre does not go down completely to zero. The dip from sample B has FWHM 33 neV (8.0 MHz), 5 s integration per point. The CPT simulation uses $\hbar\Omega_1 = 0.1$ μeV, $\hbar\Omega_2 = 0.49$ μeV, and, as in (b), $\Gamma_r = 0.68$ μeV, $T_2 > 1$ μs, $T_1 \gg T_2$. In this case, the remaining signal in the dip centre is likely to be a consequence of the small value of Z_h: the dark state can be destroyed by the weak coupling of the pump to the probe transition.

the single quantum dot optical linewidths which are the same in sample A as those on high quality n-type devices [26]. More importantly, the low-noise environment removes the charge-noise-induced fluctuations of the CPT dip position which have plagued earlier experiments in Chapter 2. The occupation of the upper level is monitored with high signal:noise by detecting the resonance fluorescence [25, 26], Fig. 7.2(b),(c). The resonance fluorescence exhibits a Lorentzian envelope with full-width-at-half-maximum (FWHM) 2.5 μeV and a pronounced dip with FWHM 80 neV (19.3 MHz). A zoom-in of the CPT dip is shown in Fig. 7.2(c) along with CPT from a quantum dot in sample B with CPT dip width 33 neV (8.0 MHz). These spectra enable the determination of Z_h with a resolution of ~ 10 neV. This is 10^8-times smaller than the optical transition energy, 250-times smaller than the optical linewidth, and 70-times smaller than the optical transform limit.

7.2.3 Highly decoupled hole spin from nuclear spins

The transverse hole hyperfine interaction is measured by combining CPT and dynamic nuclear polarization (DNP). The exciton resonance is locked to the pump laser frequency via the dragging effect [17, 27, 28] resulting in DNP. The Overhauser field is thereby controlled via the detuning δ_2 of the pump laser with respect to the bare transition frequency. A strong constant frequency pump laser defines the nuclear spin state and a weak probe laser ($\Omega_1 \ll \Omega_2$) measures both Z_h and the electron Zeeman splitting Z_e. The probe laser is scanned across the vertical and diagonal transitions, Fig. 7.3(a),(b). A pronounced dip in the spectrum indicates CPT and measures Z_h with ultra-high resolution. For zero pump detuning (zero DNP), the probe response at much lower frequencies than the pump laser (factor of 10 less) determines Z_e: we observe an increase in RF when the probe comes into resonance with the lower energy "vertical" transition. As the pump is detuned, Z_e changes by ΔZ_e via DNP. The shifts in this low frequency resonance monitor the DNP and determine ΔZ_e, Fig. 7.3(a),(b). Importantly, the probe coupling is lowered in these experiments until the probe itself is too weak to induce DNP, i.e. the frequency of the low energy resonance does not depend on Ω_1. Fig. 7.3(c),(d) plots Z_h versus ΔZ_e. Although Z_e changes by almost 20 μeV, Z_h remains constant to within 20 neV for both samples. This is the main result of the experiment: large values of I_x do not result in a measurable change in Z_h even when Z_h is measured with high resolution.

Quantitatively, our experiment shows that $\Delta Z_h/\Delta Z_e < 0.1\%$ in the presence of a transverse DNP. This is equivalent to $|A_i^{h,\perp}/A_i^e| < 0.1\%$. Furthermore, with $|A_i^{h,z}/A_i^e| = 10\%$ [17–19] (a ratio we have confirmed on quantum dots in these samples), we can quantify the anisotropy of the hole spin hyperfine interaction $|A_i^{h,\perp}/A_i^{h,z}| < 1\%$. This is consistent with a generic theoretical estimate [7]; we are not aware of a calculation specific to an InGaAs quantum dot. In terms of energies, $A_i^{h,\perp} < 0.1$ μeV. This implies a very small energy broadening δZ_h in

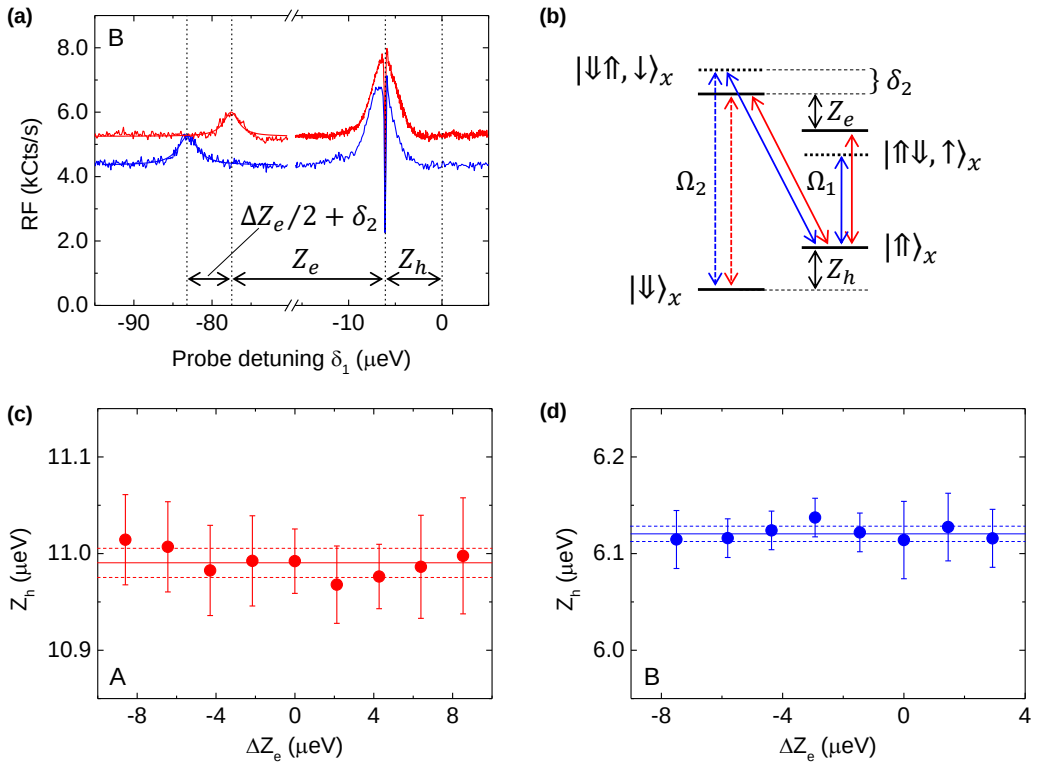

Figure 7.3 | (a) Measured probe resonance fluorescence spectrum on sample B in the presence of a much stronger, constant frequency pump laser, red: $\delta_2 = 0$; blue: $\delta_2 = 3.4$ μeV. The frequency of the probe laser is scanned across the "vertical" and "diagonal" transitions and is plotted with respect to the pump frequency in both cases. The pronounced dip signifies CPT and occurs when $\delta_1 = Z_h$. The peak at large and negative δ_1 arises when the probe is in resonance with the lower energy "vertical" transition. At $\delta_2 = 0$ the separation between this resonance and the CPT dip determines Z_e, the Zeeman energy of the exciton (determined by the lone electron spin). The shift in this resonance signifies a dynamic nuclear polarization (DNP): Z_e changes in response to the change in pump detuning. The measured Rabi energies are $\hbar\Omega_1 = 0.049$ μeV and $\hbar\Omega_2 = 0.49$ μeV; hole g-factor 0.034; magnetic field 3.00 T; integration time per point 5 s; temperature 4.2 K. (b) The quantum states of the system: the red arrows indicate the optical transitions addressed by scanning the probe laser for $\delta_2 = 0$, blue for $\delta_2 > 0$. (c),(d) Z_h versus the change of the electron Zeeman energy ΔZ_e for samples A and B, respectively. The solid line represents the average value, the dashed lines represent $\pm\sigma$ where σ is the standard deviation. At the one-σ level, $dZ_h/d\Delta Z_e = 0.1\%$.

the presence of un-polarized but noisy nuclei ($\delta Z_e = 600$ neV): $\delta Z_h^{\text{spin}} < 0.6$ neV. The energy broadening arising from the longitudinal coupling, i.e. A_h^z, is sub-neV for all transverse fields above about 500 mT.

Charge noise-induced spin dephasing should also be considered (Chapter 2 and 6). We estimate the charge noise from the optical linewidth and RF noise spectra [26]. Charge noise is particularly small on sample A contributing < 0.1 µeV to the optical linewidth (see Appendix A). We measure the bias dependence of Z_h and find that charge noise results in a fluctuation $\delta Z_h^{\text{charge}} = 0.3$ neV at $B_x = 3.00$ T. The final conclusion is that $\delta Z_h < 0.67$ neV, resulting in a $T_2^* \simeq 1$ µs. These long values of the hole spin T_2^* arise from the application of an in-plane magnetic field to suppress the longitudinal hyperfine interaction, a highly suppressed transverse hyperfine interaction and low levels of charge noise to reduce charge-noise-induced-dephasing.

References

[1] I. A. Merkulov, A. L. Efros, and M. Rosen, Phys. Rev. B **65**, 205309 (2002).

[2] A. V. Khaetskii, D. Loss, and L. Glazman, Phys. Rev. Lett. **88**, 186802 (2002).

[3] J. Fischer, W. A. Coish, D. V. Bulaev, and D. Loss, Phys. Rev. B **78**, 155329 (2008).

[4] R. J. Warburton, Nat. Mater. **12**, 483 (2013).

[5] B. Eble, C. Testelin, P. Desfonds, F. Bernardot, A. Balocchi, T. Amand, A. Miard, A. Lemaître, X. Marie, and M. Chamarro, Phys. Rev. Lett. **102**, 146601 (2009).

[6] C. Testelin, F. Bernardot, B. Eble, and M. Chamarro, Phys. Rev. B **79**, 195440 (2009).

[7] J. Fischer and D. Loss, Phys. Rev. Lett. **105**, 266603 (2010).

[8] F. Maier and D. Loss, Phys. Rev. B **85**, 195323 (2012).

[9] X. Xu, W. Yao, B. Sun, D. G. Steel, A. S. Bracker, D. Gammon, and L. J. Sham, Nature (London) **459**, 1105 (2009).

[10] H. Ribeiro, F. Maier, and D. Loss, arXiv:1403.0490 (2014).

[11] D. Heiss, S. Schaeck, H. Huebl, M. Bichler, G. Abstreiter, J. J. Finley, D. V. Bulaev, and D. Loss, Phys. Rev. B **76**, 241306 (2007).

[12] B. D. Gerardot, D. Brunner, P. A. Dalgarno, P. Ohberg, S. Seidl, M. Kroner, K. Karrai, N. G. Stoltz, P. M. Petroff, and R. J. Warburton, Nature (London) **451**, 441 (2008).

[13] D. Brunner, B. D. Gerardot, P. A. Dalgarno, G. Wüst, K. Karrai, N. G. Stoltz, P. M. Petroff, and R. J. Warburton, Science **325**, 70 (2009).

[14] K. De Greve, P. L. McMahon, D. Press, T. D. Ladd, D. Bisping, C. Schneider, M. Kamp, L. Worschech, S. Höfling, A. Forchel, and Y. Yamamoto, Nat. Phys. **7**, 872 (2011).

[15] A. Greilich, S. G. Carter, D. Kim, A. S. Bracker, and D. Gammon, Nat. Photonics **5**, 702 (2011).

[16] T. M. Godden, J. H. Quilter, A. J. Ramsay, Y. Wu, P. Brereton, S. J. Boyle, I. J. Luxmoore, J. Puebla-Nunez, A. M. Fox, and M. S. Skolnick, Phys. Rev. Lett. **108**, 017402 (2012).

[17] P. Fallahi, S. T. Yilmaz, and A. Imamoğlu, Phys. Rev. Lett. **105**, 257402 (2010).

[18] E. A. Chekhovich, A. B. Krysa, M. S. Skolnick, and A. I. Tartakovskii, Phys. Rev. Lett. **106**, 027402 (2011).

[19] H. Kurtze, D. R. Yakovlev, D. Reuter, A. D. Wieck, and M. Bayer, Phys. Rev. B **85**, 195303 (2012).

[20] E. A. Chekhovich, M. M. Glazov, A. B. Krysa, M. Hopkinson, P. Senellart, A. Lemaitre, M. S. Skolnick, and A. I. Tartakovskii, Nat. Phys. **9**, 74 (2013).

[21] A. J. Bennett, M. A. Pooley, Y. Cao, N. Sköld, I. Farrer, D. A. Ritchie, and A. J. Shields, Nat. Commun. **4**, 1522 (2013).

[22] M. Fleischhauer, A. Imamoglu, and J. P. Marangos, Rev. Mod. Phys. **77**, 633 (2005).

[23] X. Xu, B. Sun, P. R. Berman, D. G. Steel, Allan, Bracker, D. Gammon, and L. J. Sham, Nat. Phys. **4**, 692 (2008).

[24] J. Hansom, C. H. H. Schulte, C. Le Gall, C. Matthiesen, E. Clarke, M. Hugues, J. M. Taylor, and M. Atatüre, Nat. Phys. **10**, 725 (2014).

[25] A. V. Kuhlmann, J. Houel, D. Brunner, A. Ludwig, D. Reuter, A. D. Wieck, and R. J. Warburton, Rev. Sci. Instrum. **84**, 073905 (2013).

[26] A. V. Kuhlmann, J. Houel, A. Ludwig, L. Greuter, D. Reuter, A. D. Wieck, , M. Poggio, and R. J. Warburton, Nat. Phys. **9**, 570 (2013).

[27] C. Latta, A. Högele, Y. Zhao, A. N. Vamivakas, P. Maletinsky, M. Kroner, J. Dreiser, I. Carusotto, A. Badolato, D. Schuh, W. Wegscheider, M. Atature, and A. Imamoglu, Nat. Phys. **5**, 758 (2009).

[28] A. Högele, M. Kroner, C. Latta, M. Claassen, I. Carusotto, C. Bulutay, and A. Imamoglu, Phys. Rev. Lett. **108**, 197403 (2012).

Chapter 8

Conclusion and Outlook

In this thesis the quantum mechanical effect of coherent population trapping was used to investigate holes in semiconductor quantum dots via resonance fluorescence. The analysis of the dark states in a pump-probe experiment is a powerful tool to realise high resolution dark state spectroscopy. Conclusions about the coherence of the single hole spin can be drawn from the dip depth and width. The main result is an answer to a basic semiconductor question: To which extend interacts the hole spin with the nuclei in the QD. Can we extract a value for the hyperfine coefficients?

The CPT measurements in the last Chapter 7 provide the answer: The hole spin is highly anisotropic and its in-plane component is decoupled from the nuclei to a large extent. The in-plane hyperfine coupling coefficient $A_i^{h,x}$ is only 0.1 % of the electron coupling constant A_i^e, and 1 % of the hole hyperfine coupling coefficient out of plane $A_i^{h,z}$.

Based on this important result we conclude in Chapter 7, we have in the very low charge noise devices dephasing times approaching 1 µs in an in-plane magnetic field. The CPT spectroscopy measurements yield decoherence times greater than 1 µs in Chapter 2 and 7. An electrically tunable hole g-factor over a range of more than 100 kV/cm was shown in an in-plane magnetic field (Chapter 6). Very narrow, transform-limited linewidths were demonstrated for the positively charged exciton X^{1+} ($\Gamma_{X^{1+}} = 0.67 \pm 0.13$ µeV) in Chapter 4 and for the negatively charged exciton X^{1-} ($\Gamma_{X^{1-}} = 0.75 \pm 0.1$ µeV) in Chapter 5. These linewidth are extracted during fast scanning through the resonance. However, even for slow measurements with a dwelling time of a few seconds on the transition the transform-limit is reached for the neutral exciton X^0 ($\Gamma_{X^0} = 1.19 \pm 0.13$ µeV) in Chapter 5. In Chapter 3 a feedback scheme was implemented and a frequency stabilized QD emission was realised. The stabilization loop reduces the charge noise in the sample.

The high quality p-doped samples investigated in this thesis in combination with the resonant laser spectroscopy setup, made a whole series of interesting measurements on holes and hole spins possible. In the future a lot of compelling experiments could build on these results:

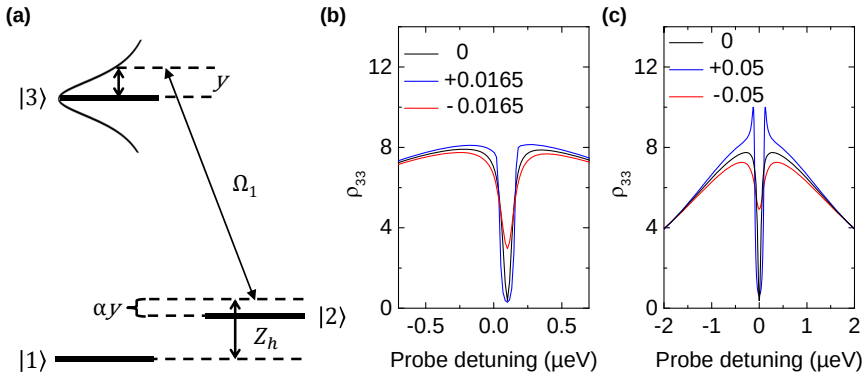

Figure 8.1 | (a) Scheme introducing $\alpha_h = (\mathrm{d}Z_h/\mathrm{d}F)/(\mathrm{d}E_X/\mathrm{d}F)$ in the Λ-system. α_h is the connection between ground state fluctuations and the excitonic fluctuations y. (b) Influence of the α-parameter on the CPT dip under probe detuning. The detuning is relative to the pump laser energy, which is here detuned by 0.1 µeV with respect to the transition. α_h is positive in the case of (a). (c) CPT of the three level model with large α_h and no pump detuning. The resonance dip is either preserved (blue) or washed out (red), dependent on the sign and the magnitude of α_h.

In Chapter 4 the positively charged exciton was analysed in detail. However, the X^{1+} is not yet fully understood. The experiment gives no solid explanation for the mechanism of the large "off" times (τ_{off}) in the middle of the voltage plateau. So far there are only speculations involving the creation of a dark state or a spin pumping process. Additional measurements with an small out of plane magnetic field and two laser would be required to explore this mechanism further.

The coherent population trapping experiment in Chapter 7 and the analysis with the density matrix model (Appendix C) takes only the influence of the spectral fluctuations of the upper level into account. The two ground states are robust against charge fluctuations and the CPT dip is preserved.

In Chapter 6 a electric field dependence of the hole g-factor $g_h(F)$ was measured. Based on this result speculations emerge, the simple model is not completely true and the influence of electric field fluctuations on the hole spins in the ground states is not always negligible. Fig. 8.1 explains and introduces the theory of the "α-parameter". The factor α_h establishes the connection between possible ground state fluctuations and the excitonic fluctuations seen from the upper state (y). Dependent on the dc Stark shift $\mathrm{d}E_X/\mathrm{d}F$ and the change of the hole g-factor, and therefore of the hole Zeeman splitting $\mathrm{d}Z_h/\mathrm{d}F$, the sign and the magnitude of α_h is determined. α_h is a fixed parameter inherent in the sample and given by the ratio $(\mathrm{d}Z_h/\mathrm{d}F)/(\mathrm{d}E_X/\mathrm{d}F)$. The upper level moves according to the dc Stark shift of the exciton

by y, in contrast the Zeeman split ground state levels, which are influenced only by a fraction of the electric field fluctuations $\alpha_h y$.

The concept has to be included in the first convolution of the density matrix calculation with the spectral fluctuations (Appendix C). The sign of α_h and the mutual energy relation of the pump (Ω_2) and probe (Ω_1) laser is very important to include α_h correctly. For the case in Fig. 8.1(a) the equation changes to:

$$\mathrm{CPT}(\delta_2, \delta_1) = \beta_{\mathrm{RF}} \int \rho_{33}\big(\delta_2 - y, \delta_1 - y(1-\alpha_h)\big) L_1(y) dy \tag{8.1}$$

Fig.s 8.1(b) and (c) demonstrate the influence of α_h. For a smaller probe than pump laser energy and a positive alpha, the CPT dip is conserved and broadened, in that case both energy levels move in parallel (blue). If the level move anti-parallel, the dip is smeared out (red). The magnitude of α_h amplifies the effect (c).

Future experiments would be necessary to test the theory of the α_h-parameter. A straight forward experiment could be an artificial noise source integrated in the experiment. A square wave modulation superimposed over the applied gate voltage would lead to an additional broadening of the exciton linewidth. The resulting influence on the CPT dip can provide information about the functionality of α_h.

All experiments presented in this thesis were performed using a continuous wave excitation. The QD states are always in a steady state solution and it is not possible to create an arbitrary superposition of the states. Experiments with fast coherent hole spin manipulation and spin initialisation would be obvious choices for future experiment. These experiments require a change of the measurement method to the time resolved spectroscopy domain and were therefore not yet realised. The possible experiments would include resonant pulsed excitation created by an electro optic modulator (EOM) or a fast pulsed laser. After an initialization pulse, a GHz electromagnetic field could drive the transition between $|\Downarrow\rangle$ and $|\Uparrow\rangle$ directly and induce spin rotations. The big advantage for coherent hole spin rotations is no population in the quickly dephasing excited state. It would be a challenging and very compelling goal to measure hole spin dephasing times as high as 1 µs in these low charge noise devices in the time domain.

APPENDIX

Supplementary Information to Chapters 5–7

Appendix A

Supplementary information to Chapter 5 "Transform-limited linewidth"

Adapted from:

Andreas V. Kuhlmann, Jonathan H. Prechtel, Julien Houel, Arne Ludwig, Dirk Reuter, Andreas D. Wieck and Richard J. Warburton

"Transform-limited single photons from a single quantum dot"

submitted manuscript, arXiv:1307.7109v2

In Chapter 5, the linewidth of the optical transition of a single quantum dot is discussed. Here, we explain details of the experiments, the data processing and the modelling.

A.1 The semiconductor n-doped quantum dot sample

A quantum dot (QD) sample grown by molecular beam epitaxy is used to probe the optical linewidth of single photons from a single QD. All the data presented in the Chapter 5 were measured on three QDs from different samples: QD1 from sample A (Fig.s 5.1 (a)-(e), 5.3 and 5.4 of Chapter 5) , QD2 from sample B (Fig. 5.1 (g)) and QD3 from sample C (Fig. 5.2).

The self-assembled QDs are embedded in a Schottky diode [1, 2] as shown in Fig. A.1 (a). The layer sequence is:

1. *back contact*
   50 nm n^+-GaAs, doping level $\sim 1.7 \times 10^{18}\,\mathrm{cm}^{-3}$
2. *tunnelling barrier*
   25 nm i-GaAs
3. *active layer*
   InGaAs QDs (diameter $\sim$ 20 nm, height $\sim$ 5 nm) with centre wavelength 950 nm
4. *capping layer*
   150 nm i-GaAs
5. *blocking barrier*
   68 periods AlAs/GaAs 3 nm/1 nm
6. *cap*
   10 nm i-GaAs
7. *Schottky gate*
   sample A 5 nm/10 nm Ti/Au
   sample B and C 3 nm/7 nm Ti/Au.

The samples only differ in the gate thickness, they are from the same wafer.

The background doping of as-grown GaAs is p $\sim 10^{13}\,\mathrm{cm}^{-3}$; two-dimensional electron gases grown under similar conditions have mobilities $> 10^6\,\mathrm{cm}^2/\mathrm{Vs}$.

The number of electrons confined to the QD can be precisely controlled by the gate voltage V_g as illustrated in Fig. A.1 (b). A change of gate voltage yields a change of the QD's local potential ϕ by

$$\Delta\phi = \frac{\Delta V_g}{\lambda} \tag{A.1}$$

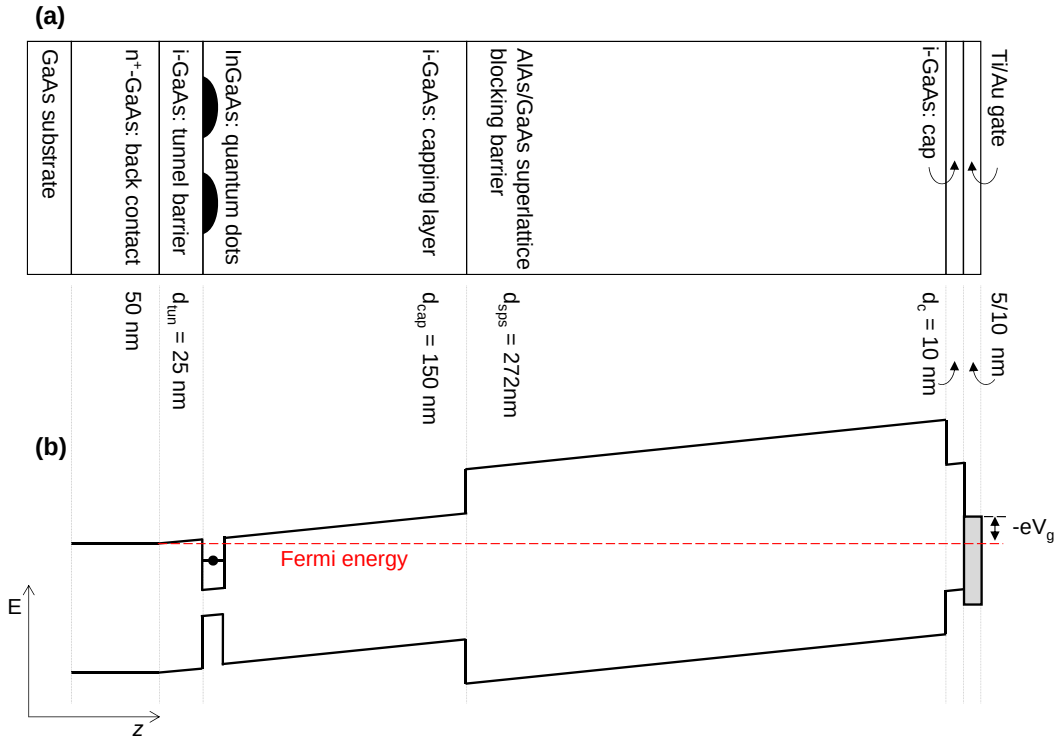

Figure A.1 | (a) Sample layer structure and the corresponding (b) energy band diagram. The Fermi energy is pinned to the conduction band edge of the back contact. The figures are to scale with respect to length.

where $\lambda = 18.3$ denotes the sample's lever arm, defined as the ratio of back contact to gate distance d and tunnel barrier thickness. The exciton energy E is detuned with respect to the constant laser frequency by exploiting the dc Stark effect,

$$\Delta E = a\Delta F, \quad \Delta F = \frac{\Delta V_g}{d} \tag{A.2}$$

with Stark shift coefficient a and electric field F.

A.2 The dc Stark shift

The Stark shift is determined by recording the resonance position in V_g for many laser frequencies, the laser frequency measured in each case with an ultra-precise wavemeter. The Stark shift is linear in ΔF for the small windows of V_g used here, Fig. A.2(a). The neutral exciton X^0 has a larger Stark shift ($a = 0.0306$ µeV cm/V) than the charged exciton X^{1-} ($a = 0.0219$ µeV cm/V) and thus it is more sensitive to charge noise. X^{1-} has a larger linewidth ($\Gamma = 1.48$ µeV) compared to X^0 ($\Gamma = 1.28$ µeV) despite the smaller Stark shift. Also, experiments on

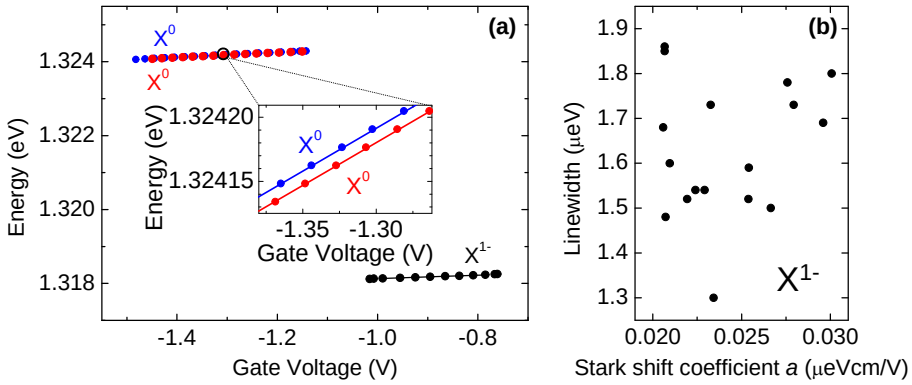

Figure A.2 | (a) Exciton energy voltage plateaus to determine the Stark shift coefficients of the neutral exciton X^0 and the trion X^{1-}. Inset shows a zoom in of X^0 revealing the fine structure splitting $\Delta = 11.5$ μeV. Data from QD1. (b) Linewidth versus Stark shift. Statistics on X^{1-} of 17 QDs from the same wafer with a spread in Stark shift of up to 50% demonstrate no significant correlation between linewidth and Stark shift.

several QDs reveal no dependence of the linewidth on the Stark shift coefficient, Fig. A.2(b). The Stark shift varies from quantum dot to quantum dot by up to 50% without a correlated change in linewidth. Both these facts support the dominant influence of spin noise and not charge noise on the X^0 and X^{1-} linewidths.

A.3 Power broadening

The linewidth of the optical resonance increases with increasing resonant excitation power, Fig. A.3. The additional contribution to the linewidth is known as *power broadening*, described for an ideal 2-level system by [3]

$$\Gamma(\Omega) = \sqrt{\Gamma_0^2 + 2\Omega^2} + \gamma, \quad \Gamma_0 = \hbar/\tau_R \tag{A.3}$$

with Rabi energy Ω and radiative lifetime τ_R. An inhomogeneous broadening is included with the term γ.

For X^{1-}, the 2-level model with constant γ describes the data very well, Fig. A.3(a). The inhomogeneous broadening γ is constant at low power, decreasing at high power but only when power broadening dominates, such that a constant γ allows the experimental data to be described very well (see Chapter 5). By fitting the 2-level model to the data a resonant excitation power measured by a photo diode beneath the sample can be converted to a Rabi energy, Fig. A.3(a).

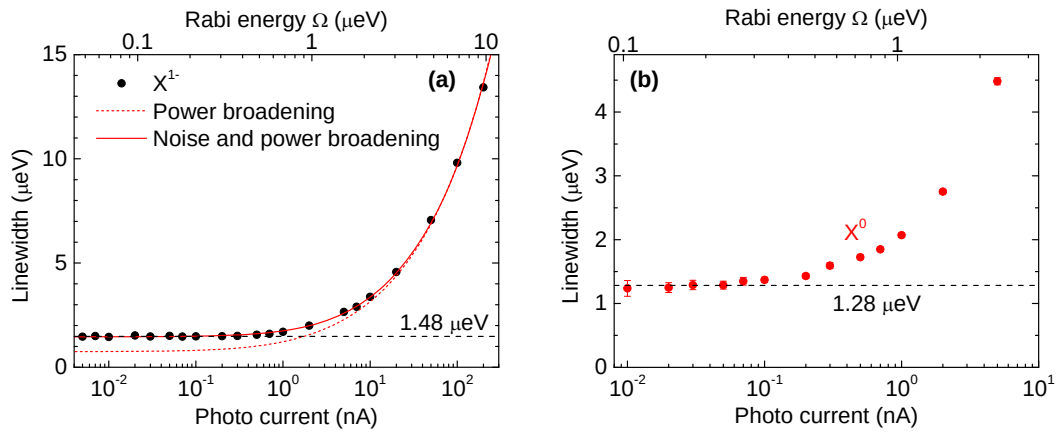

Figure A.3 | Power broadening. Linewidth power dependence for (a) X^{1-} and (b) X^0. The 2-level model with (solid red lines) and without (dashed red lines) an inhomogeneous broadening ($\gamma = 0.56$ μeV) is fitted to the X^{1-} data. The transform-limit Γ_0 is 0.75 μeV for X^{1-} and 0.92 μeV for X^0. Data from QD1.

Conversely for X^0, the 2-level model with constant γ does not describe the data well. The inhomogeneous broadening is strongly power dependent: γ increases significantly with increasing resonant excitation power (see Chapter 5).

A phonon-induced dephasing process as observed at very high Rabi couplings [4] and in pulsed experiments [5] is negligible at these Rabi couplings.

A.4 Resonance fluorescence

The quantum dot optical resonance is driven with a linearly-polarized, resonant continuous-wave laser (1 MHz linewidth) focused on to the sample surface. Reflected or scattered laser light is rejected with a dark-field technique using crossed linear polarizations for excitation and detection [6]. The laser excitation polarization is tilted by an angle of $\pi/4$ with respect to the neutral exciton's linear polarization axes.

Resonance fluorescence is detected with a silicon avalanche photodiode in photon counting mode. The experiment is not shielded against the earth's magnetic field, thus $B_{\min} \sim 50$ μT. All the experiments were performed with the sample at 4.2 K.

A.5 Quantum dot noise spectrum

To determine the QD noise spectrum the arrival time of each photon is recorded over the entire measurement time T. Post measurement, a binning time t_{bin} is selected, typically 1 μs. The number of counts in each time bin is $S(t)$, the average number of counts per bin $\langle S(t) \rangle$. The

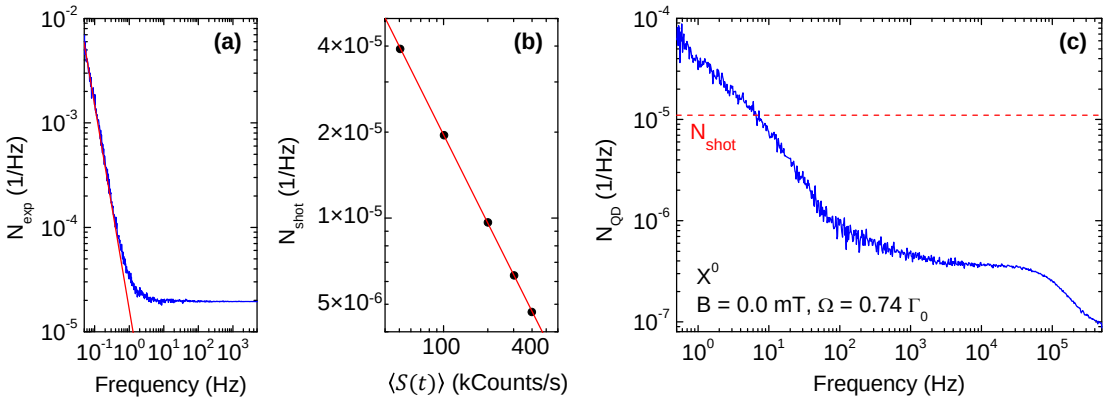

Figure A.4 | (a) Noise spectrum of the experiment. Intensity fluctuations of the laser light in the setup cause a $1/f^2$-behaviour of $N_{\mathrm{exp}}(f)$ at low frequencies (exponent of red fit -1.96). For $f > 10$ Hz the spectrum is dominated by shot noise, thus, the spectrum is flat. The average count rate of the detected laser light is 101 kCounts/s in this particular experiment. (b) Shot noise. Noise spectra of the experiment alone were recorded at different laser light count rates to extract the dependence of the shot noise on the count rate. A proportionality of the shot noise to $\langle S(t)\rangle^{-1}$ is verified (exponent of red fit -1.03). (c) Quantum dot noise spectrum. The noise of the experiment is typically larger than the noise of the QD. The shot noise (red dashed line) typically equals $N_{\mathrm{QD}}(f)$ at low frequencies ($f \sim 10$ Hz), and exceeds $N_{\mathrm{QD}}(f)$ at higher frequencies. The RF count rate is 176 kCounts/s in this particular experiment. Data from QD2.

fast Fourier transform of the normalized RF signal $S(t)/\langle S(t)\rangle$ is calculated to yield a spectrum of the noise power $N_{\mathrm{RF}}(f)$, specifically

$$N_{\mathrm{RF}}(f) = \left|\mathrm{FFT}\left[S(t)/\langle S(t)\rangle\right]\right|^2 (t_{\mathrm{bin}})^2/T. \tag{A.4}$$

$N_{\mathrm{RF}F}(f)$ has the same spectrum independent of the choice of t_{bin} and T: smaller values of t_{bin} allow $N_{\mathrm{RF}}(f)$ to be determined to higher values of frequency f; larger values of T allow $N_{\mathrm{RF}}(f)$ to be determined with higher resolution. The high frequency limit of our experiment is only limited by the photon flux.

All Fourier transforms are normalized [7] such that the integral of the noise power $N_x(f)$ over all positive frequencies equals the variance of the fluctuations δx,

$$\langle(\delta x)^2\rangle = \int_0^\infty df N_x(f). \tag{A.5}$$

To record a noise spectrum of the experiment alone, the QD is detuned by > 100 linewidths relative to the laser and one polarizer is rotated by a small angle to open slightly the detection channel for reflected laser light, choosing the rotation so that the detected laser light gives a count rate similar to the QD RF. A noise spectrum of the reflected laser light (Fig. A.4(a)) is

recorded using exactly the routine used to analyse the RF, yielding $N_{\mathrm{exp}}(f)$. $N_{\mathrm{exp}}(f)$ has a $1/f^2$-behaviour at low frequencies arising from intensity fluctuations in the setup. For $f > 10$ Hz, $N_{\mathrm{exp}}(f)$ has a completely f-independent spectrum, $N_{\mathrm{exp}} \sim 10^{-5}$ Hz^{-1}: this is the shot noise N_{shot}. The noise of the experiment is typically larger than the noise of the QD $N_{\mathrm{QD}}(f)$. The shot noise is proportional to $\langle S(t)\rangle^{-1}$ (Fig. A.4(b)) and not to $\langle S(t)\rangle^{1/2}$ due to the normalization of $S(t)$ by $\langle S(t)\rangle$ in the calculation of the spectrum. N_{shot} is comparable to $N_{\mathrm{QD}}(f)$ at low frequencies ($f \sim 10$ Hz), and exceeds $N_{\mathrm{QD}}(f)$ at higher frequencies, Fig. A.4(c).

The noise spectrum of the QD alone is then determined using

$$N_{\mathrm{QD}}(f) = N_{\mathrm{RF}}(f) - N_{\mathrm{exp}}(f). \tag{A.6}$$

Correction of $N_{\mathrm{RF}}(f)$ with $N_{\mathrm{exp}}(f)$ where $N_{\mathrm{RF}}(f)$ and $N_{\mathrm{exp}}(f)$ are not measured simultaneously is successful on account of the high stability of the setup. Furthermore, no spectral resonances in $N_{\mathrm{QD}}(f)$ have been discovered. We present here $N_{\mathrm{QD}}(f)$ after averaging at each f over a frequency range Δf to yield equidistant data points on a logarithmic scale. This entire procedure enables us to discern $N_{\mathrm{QD}}(f)$ down to values of 10^{-7} Hz^{-1} for $T = 2$ hours.

A.6 Effect of charge noise on the linewidth

The quantum dot noise spectrum $N_{\mathrm{QD}}(f)$ allows us to set an upper limit of the linewidth broadening γ_{c} due to charge noise. The energy jitter due to charge fluctuations is less than the linewidth such that the change in RF is related quadratically to the detuning for fluctuations around $\delta = 0$. This quadratic approximation overestimates the effect of charge fluctuations on the linewidth. The variance of the quantum dot RF noise, $\sigma^2_{\mathrm{QD,c}}$, is related to an integral of the noise curve. Integrating over the bandwidth of charge noise after subtracting spin noise,

$$\gamma_{\mathrm{c}} = \frac{\Gamma}{2}\left(\sigma^2_{\mathrm{QD,c}}/3\right)^{1/4}. \tag{A.7}$$

The charge noise has a $1/f$-like component and a Lorentzian component. We integrate both from 0.1 Hz to 1 GHz. Applying this concept to the X^{1-} noise spectrum of Fig. 5.3(c) of Chapter 5, with $\Gamma = 1.48$ µeV this predicts $\gamma_{\mathrm{c}} < 0.05$ µeV.

A.7 Noise spectra modelling

Our previous experiments [8] demonstrate that the spectrum of the noise in the RF is dominated by charge noise at low frequency, spin noise at high frequency. The noise sensor, the RF from a single quantum dot, has a trivial dependence on the fluctuating electric $F(t)$ and magnetic

fields $B_N(t)$ only for small fluctuations in the detunings around particular values of detuning δ. Monte Carlo simulations allow us to determine both the electric field and magnetic field noise accurately by describing the response of the sensor for all δ, treating charge noise and spin noise on an equal footing.

The basic approach is to calculate $F(t)$ and $B_N(t)$, in each case from an ensemble of independent, but identical, 2-level fluctuators using a Monte Carlo method; to calculate the RF signal $S(t)$ from $F(t)$ and $B_N(t)$; and to compute the noise $N(f)$ from $S(t)$ using exactly the same routine as for the experiments (but without the correction for extrinsic noise of course). Here, we discuss the spin noise modelling of the neutral exciton X^0 used to extract the root-mean-square (rms) values of the magnetic field $B_{N,\mathrm{rms}}$ in Fig. 5.3(b) of Chapter 5. The modelling of charge noise is explained in detail elsewhere [8].

For X^0, the RF depends on the electric and magnetic fields according to

$$S(t) = \frac{\left(\frac{\Gamma_0}{2}\right)^2}{\left(aF(t) + \delta_0(t) + \delta\right)^2 + \left(\frac{\Gamma_0}{2}\right)^2}, \quad \delta_0(t) = \pm\frac{1}{2}\sqrt{\Delta^2 + \delta_1(t)^2}, \quad \delta_1(t) = \frac{1}{2}g\mu_B B_N(t), \tag{A.8}$$

where a is the dc Stark coefficient, g the electron g-factor and Δ the fine structure splitting. For the blue Zeeman branch $\delta_0(t)$ is positive, for the red one negative, respectively.

An ensemble of identical 2-level fluctuators fully describes spin noise, Fig. 5.3(a) of Chapter 5.

A.7.1 Spectrum of a 2-level fluctuator

A 2-level fluctuator occupies either state 0 with lifetime τ_0 or state 1 with lifetime τ_1. The probability p of being, at any time, in state 1 is $\tau_1/(\tau_0 + \tau_1)$; the probability of being in state 0 is $\tau_0/(\tau_0 + \tau_1)$. The configuration $C(t)$ of a 2-level fluctuator, either 0 or 1, is determined by the probabilities of a $0 \to 1$ transition [9],

$$p_{0\to1}(\delta t) = 1 - \frac{1}{\tau_0 + \tau_1}\left[\tau_1 \exp\left(-\left(\frac{1}{\tau_0} + \frac{1}{\tau_1}\right)\delta t\right) + \tau_0\right] \tag{A.9}$$

and a $1 \to 0$ transition,

$$p_{1\to0}(\delta t) = 1 - \frac{1}{\tau_0 + \tau_1}\left[\tau_0 \exp\left(-\left(\frac{1}{\tau_0} + \frac{1}{\tau_1}\right)\delta t\right) + \tau_1\right] \tag{A.10}$$

where δt denotes the time over which the system evolves. The power spectrum of a 2-level fluctuator $S(\omega)$ is Lorentzian [9],

$$S(\omega) = \frac{1}{\pi}\frac{\tau_0\tau_1}{(\tau_0 + \tau_1)^2}\frac{1/T}{\omega^2 + (1/T)^2}, \quad 1/T = 1/\tau_0 + 1/\tau_1. \tag{A.11}$$

A.7.2 Spin noise

The calculation of the time trace of the magnetic field $B_N(t)$ is simplified, such that each nucleus is treated as a two-level fluctuator, with equal $0 \to 1$, $1 \to 0$ transition rates, $1/\tau$. At $t = 0$, each nucleus is initialized by a random number generator giving a configuration of nuclear spins $C(0)$. At a later time, δt, $C(\delta t)$ is calculated from $C(0)$ again with a random number generator using the probabilities $p_{1\to0}(\delta t)$ and $p_{0\to1}(\delta t)$ from the theory of a two-level fluctuator. The nuclei are treated independently.

The nuclear magnetic field, the so-called Overhauser field B_N, is given by [10]

$$B_N = \frac{v_0}{g\mu_B} \sum_{i=1}^{N} A_i \left|\psi(\mathbf{r}_i)\right|^2 I_i \tag{A.12}$$

where v_0 is the atomic volume, A_i the hyperfine interaction constant, $\mathbf{r}_i$ is the position of the nuclei i with spin I_i, and $\psi(\mathbf{r})$ is the normalized electron envelope function. By using an average hyperfine constant [11] $A = 90$ µeV and approximating the electron envelope function $\psi(\mathbf{r})$ by a top hat, Eq. (A.12) simplifies to

$$B_N = \frac{A}{g\mu_B N_{\text{eff}}} \sum_{i=1}^{N_{\text{eff}}} I_i. \tag{A.13}$$

N_{eff} denotes the number of nuclear spins inside the top hat envelope function.

Regarding the dimensionality of B_N, a 1D model for the nuclear spins is appropriate for X^0. The isotropic part of the electron-hole exchange interaction "protects" the X^0 from the in-plane fluctuations of the nuclear magnetic field. Specifically, the z-component of the Overhauser field enters along the diagonals of the exchange/Zeeman Hamiltonian [12] in the $|\Uparrow\downarrow\rangle$, $|\Downarrow\uparrow\rangle$, $|\Uparrow\uparrow\rangle$, $|\Downarrow\downarrow\rangle$ basis and results in the dispersion of Eq. A.8. The in-plane components of the Overhauser field couple $|\Uparrow\downarrow\rangle \leftrightarrow |\Uparrow\uparrow\rangle$ and $|\Downarrow\uparrow\rangle \leftrightarrow |\Downarrow\downarrow\rangle$ but these states are split by the dark-bright splitting, 100s of µeV, determined by the isotropic part of the exchange interaction. As a result the dependence of the exciton energy on the in-plane fields is negligible.

We assume that each nuclear spin I can be represented by a spin-$\frac{1}{2}$, a 2-level fluctuator. To account for an underestimate of the hyperfine interaction (the real spins are larger than $\frac{1}{2}$) the Overhauser field is enhanced via a reduction in the total number of nuclei, $N \to N_{\text{eff}}$. Equivalently, we could work with a higher N_{eff} and larger A. The model represents a phenomenological way to create $B_N(t)$ which mimics the experiment. $B_N(t)$ is unique, the route to $B_N(t)$ is not.

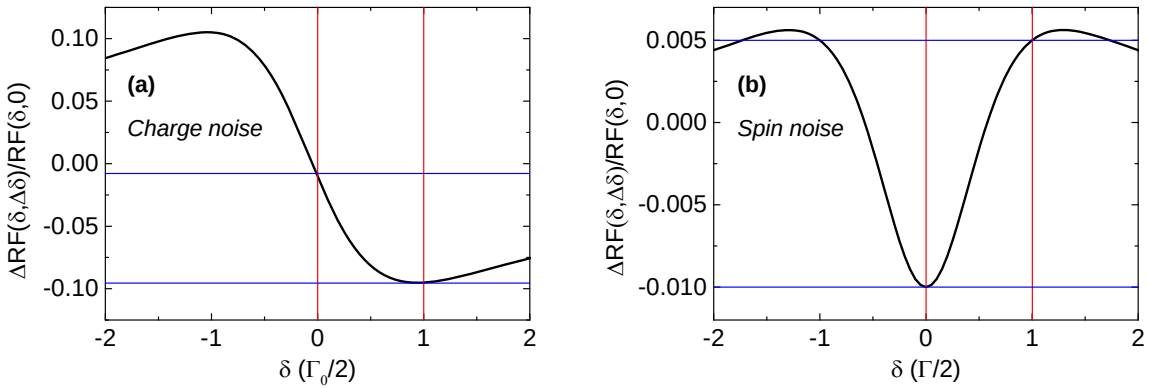

Figure A.5 | Noise sensitivity dependence on detuning for charge noise (a) and spin noise (b) for both X^0 (two lasers with frequency splitting equal to the fine structure) and X^{1-} (one laser). The relative change in the RF caused by an energy fluctuation of $\Gamma_0/20$ is shown as a function of detuning δ. The blue lines indicate the noise sensitivity for $\delta = 0$ and $\delta = \Gamma/2$.

There are two independent parameters that control spin noise in the simulation: the correlation time τ and the rms field $B_{N,\mathrm{rms}}$. For the simulation shown in Fig. 5.3 (a) of Chapter 5 $A = 90$ µeV, $N_{\mathrm{eff}} = 178$, corresponding to $B_{N,\mathrm{rms}} = 116$ mT, and $\tau = 6.0$ µeV were used. The noise spectra at higher Rabi energies were fitted by decreasing N_{eff} (increasing $B_{N,\mathrm{rms}}$) and the same τ.

A.7.3 Charge noise and spin noise sensitivity dependence on laser detuning

The sensitivity in the RF to charge noise and spin noise depends on the laser detuning δ, Fig. A.5. For X^{1-}, only one laser is required to distinguish charge noise and spin noise yet two lasers with frequencies separated by the fine structure splitting are required for X^0. Both charge noise (Fig. A.5(a)) and spin noise (Fig. A.5(b)) exhibit the same detuning dependence for X^{1-} (one laser) and X^0 (two lasers). On detuning the laser/both lasers (X^{1-}/X^0) from $\delta = 0$ to $\delta = \Gamma/2$, the sensitivity to charge noise changes from second order to first order yet the sensitivity to spin noise decreases by a factor $\sim$2.

A.7.4 Effect of a small magnetic field on the nuclear spin dynamics

A small magnetic field of $B = 10.0$ mT was applied to measure the Ω-dependence of $N_{\mathrm{QD}}(f)$, Fig. 5.3 of Chapter 5. As a result, the sensitivity of the charged exciton to spin noise is increased [8]. The nuclear spin dynamics are however not strongly changed by such a small magnetic field. Noise measurements on X^0 with and without a small magnetic field of 10.0 mT demonstrate an unchanged spin noise level, Fig. A.6.

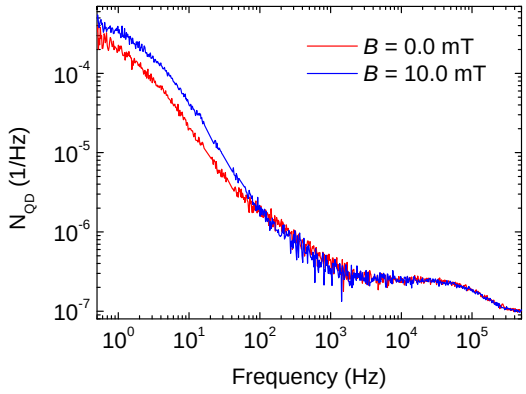

Figure A.6 | Noise measurements on X^0 at $\Omega = 0.45$ µeV with and without a small magnetic field. The small difference in charge noise is due to a different charging configuration of the device (see history effects in Ref. [8]). Data from QD1.

A.7.5 Relationship to Autler-Townes splitting

In a two-laser experiment at zero magnetic field with a resonant pump laser the optical resonance of the charged exciton splits into two resonances. The splitting reflects a static electron Zeeman splitting in the single electron ground-state and not an Autler-Townes splitting [13]. We can rule out an Autler-Townes splitting as first, the splitting is not given by the Rabi energy Ω as is the case for an Autler-Townes splitting, and secondly, we do not observe an optically-induced splitting when the X^{1-} resonance is pulled apart in a small magnetic field, Fig. A.7.

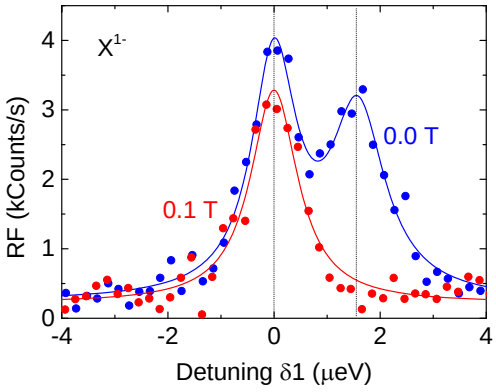

Figure A.7 | Two-laser experiment performed with identical parameters ($\Omega_1 = 0.15$ µeV, $\Omega_2 = 0.5$ µeV) on X^{1-} with and without a magnetic field. Data from QD1.

References

[1] H. Drexler, D. Leonard, W. Hansen, J. P. Kotthaus, and P. M. Petroff, Phys. Rev. Lett. **73**, 2252 (1994).

[2] R. J. Warburton, C. Schäflein, D. Haft, F. Bickel, A. Lorke, K. Karrai, J. M. Garcia, W. Schoenfeld, and P. M. Petroff, Nature (London) **405**, 926 (2000).

[3] R. Loudon, *The Quantum Theory of Light* (Oxford University Press, 2010) p. 358.

[4] S. M. Ulrich, S. Ates, S. Reitzenstein, A. Löffler, A. Forchel, and P. Michler, Phys. Rev. Lett. **106**, 247402 (2011).

[5] A. J. Ramsay, A. Gopal, E. M. Gauger, A. Nazir, B. W. Lovett, A. M. Fox, and M. S. Skolnick, Phys. Rev. Lett. **104**, 017402 (2010).

[6] A. V. Kuhlmann, J. Houel, D. Brunner, A. Ludwig, D. Reuter, A. D. Wieck, and R. J. Warburton, Rev. Sci. Instrum. **84**, 073905 (2013).

[7] S. Kogan, *Electronic Noise and Fluctuations in Solids* (Cambridge University Press, London, 1996).

[8] A. V. Kuhlmann, J. Houel, A. Ludwig, L. Greuter, D. Reuter, A. D. Wieck, , M. Poggio, and R. J. Warburton, Nat. Phys. **9**, 570 (2013).

[9] S. Machlup, J. Appl. Phys. **25**, 341 (1954).

[10] B. Urbaszek, X. Marie, T. Amand, O. Krebs, P. Voisin, P. Maletinsky, A. Högele, and A. Imamoglu, Rev. Mod. Phys. **85**, 79 (2013).

[11] C. Kloeffel, P. A. Dalgarno, B. Urbaszek, B. D. Gerardot, D. Brunner, P. M. Petroff, D. Loss, and R. J. Warburton, Phys. Rev. Lett. **106**, 046802 (2011).

[12] M. Bayer, G. Ortner, O. Stern, A. Kuther, A. A. Gorbunov, A. Forchel, P. Hawrylak, S. Fafard, K. Hinzer, T. L. Reinecke, S. N. Walck, J. P. Reithmaier, F. Klopf, and F. Schäfer, Phys. Rev. B **65**, 195315 (2002).

[13] B. D. Gerardot, D. Brunner, P. A. Dalgarno, K. Karrai, B. Badolato, P. M. Petroff, and R. J. Warburton, New Journal of Physics **11**, 013028 (2009).

Appendix B

Supplementary information to Chapter 6 "Electric field dependence of the hole g-factor"

Adapted from:

Jonathan H. Prechtel, Franziska Maier, Julien Houel, Andreas V. Kuhlmann, Arne Ludwig, Andreas D. Wieck, Daniel Loss and Richard J. Warburton

"Electrically-tunable hole g-factor of an optically-active quantum dot for fast spin rotations"

Phys. Rev. B **91**, 165304 (2015)

A theoretical model is introduced in Chapter 6 which describes the electric field dependence of the in plane hole g-factor (Fig. 6.4). The details about the Hamiltonian, the g-factor calculation and the influence of the material parameters are described here.

(The theoretical model, including the g-factor calculation, was developed by Dr. Franziska Maier. The author's contribution was to work out the right material parameters.)

B.1 Theory

We derive the in-plane g-factor of the lowest valence states in a self-assembled InGaAs quantum dot (QD) with an In concentration gradient with applied fields, a vertical electric field and an in-plane magnetic field. The heavy-hole (HH) and light-hole (LH) states of the bulk material are well described by the 4×4 Luttinger Hamiltonian. The strain fields in self-assembled QDs are of considerable strength and affect the band splitting. Strain is therefore incorporated via the Bir-Pikus Hamiltonian. To go from a bulk description to a quantum dot, we add three-dimensional harmonic confinement leading to a change from bands to quantized levels and a mixing of the HH and LH states. We include external out-of-plane electric and in-plane magnetic fields and derive an effective Hamiltonian for the two lowest, Zeeman-split HH states by decoupling them perturbatively from the higher energy states. This effective Hamiltonian is diagonalized exactly allowing the g-factor of this subsystem to be determined. The exact value of g_h^x depends on the electric field-dependent hole position and the associated local alloy composition within the QD.

B.1.1 Hamiltonian

The Hamiltonians can all be found in Ref. [1]. They are written in terms of the spin-3/2 matrices J_i, $i = x, y, z$, which are given in a basis of angular momentum eigenstates $|j, m_j\rangle$ with $j = 3/2$ and $m_j = \{3/2, 1/2, -1/2, -3/2\}$. Here, the HH band corresponds to $m_j = \pm 3/2$ and the LH band to $m_j = \pm 1/2$. For our calculations, we locate the origin of the coordinate system at the center of the QD and let the z axis point along the growth direction [001].

The bulk valence band states are described by the Luttinger Hamiltonian

$$\begin{aligned} H_k &= -\frac{\hbar^2}{2m_0}\left[\gamma_1 k^2 - 2\gamma_2\left[\left(J_x^2 - \frac{1}{3}J^2\right)k_x^2 + \text{cp}\right]\right] \\ &\quad + \frac{\hbar^2}{2m_0} 4\gamma_3 \left[\{J_x, J_y\}\{k_x, k_y\} + \text{cp}\right] \\ &\quad + \frac{2}{\sqrt{3}} C_k \left[\{J_x, J_y^2 - J_z^2\}k_x + \text{cp}\right], \end{aligned} \tag{B.1}$$

where $\{A, B\} = (AB + BA)/2$, cp denotes cyclic permutation, $\hbar k_i = -i\hbar\partial_i$, $i = x, y, z$, is the momentum operator, $k^2 = k_x^2 + k_y^2 + k_z^2$ and $J^2 = J_x^2 + J_y^2 + J_z^2$. The γ_l, $l = 1, 2, 3$, are the Luttinger parameters and the parameter C_k arises as a consequence of the spin-orbit

interaction with higher bands. We denote the diagonal part of H_k by $H_{k,0}$. We account for strain by taking into account the Bir-Pikus Hamiltonian

$$\begin{aligned} H_\varepsilon &= D_d \,\mathrm{Tr}\varepsilon + \frac{2}{3} D_u \left[\left(J_x^2 - \frac{1}{3} J^2 \right) \varepsilon_{xx} + \mathrm{cp} \right] \\ &\quad + \left[C_4 (\varepsilon_{yy} - \varepsilon_{zz}) J_x k_x + \mathrm{cp} \right], \end{aligned} \tag{B.2}$$

where we consider only diagonal elements ε_{ii}, $i = x, y, z$, of the strain tensor ε since the off-diagonal shear strain components are negligible everywhere except at the dot interfaces [2]. D_d and D_u denote vector potentials and the constant C_4 is defined in Ref. [[3]]. In the following, we refer to the diagonal, $\boldsymbol{k}$-independent part of H_ε as $H_{\varepsilon,0}$.

We model a flat, cylindrical QD by choosing a harmonic confinement potential,

$$V_c = \begin{pmatrix} V_{c,\mathrm{HH}} & 0 & 0 & 0 \\ 0 & V_{c,\mathrm{LH}} & 0 & 0 \\ 0 & 0 & V_{c,\mathrm{LH}} & 0 \\ 0 & 0 & 0 & V_{c,\mathrm{HH}} \end{pmatrix}, \tag{B.3}$$

where

$$V_{c,j}(\mathbf{r}) = -\frac{1}{2} m_{j,\perp} \omega_{j,\perp}^2 z^2 - \frac{1}{2} m_{j,\parallel} \omega_{j,\parallel}^2 (x^2 + y^2), \tag{B.4}$$

with band index $j = \mathrm{HH}, \mathrm{LH}$. The in-plane and out-of-plane confinement energies $\omega_{j,\parallel} = \hbar/(m_{j,\parallel} L^2)$ and $\omega_{j,\perp} = \hbar/(m_{j,\perp} a^2)$ are defined by the confinement lengths L and a. The corresponding effective masses in the single bands are given by $m_{\mathrm{HH/LH},\perp} = m_0/(\gamma_1 \mp 2\gamma_2)$ and $m_{\mathrm{HH/LH},\parallel} = m_0/(\gamma_1 \pm \gamma_2)$. We include an external electric field in z direction, $\boldsymbol{F} = (0, 0, F_z)$, by adding the electric potential

$$V_{el}(z) = e F_z z. \tag{B.5}$$

The in-plane magnetic field, $\boldsymbol{B} = \nabla \times \boldsymbol{A} = (B_x, 0, 0)$, is included by adding two more terms to the Hamiltonian [4, 5]. The first term is found by replacing $\boldsymbol{k} \to \boldsymbol{k} + e\boldsymbol{A}$ in $H_k + H_\varepsilon$ in a semi-classical manner. This yields the implicit magnetic field dependence given by the vector potential $\boldsymbol{A}$. We keep only terms linear in $\boldsymbol{A}$ and define

$$H_{mc} = e\boldsymbol{A} \cdot \boldsymbol{v}, \tag{B.6}$$

where $\boldsymbol{v} = \partial(H_k + H_\varepsilon)/\partial \boldsymbol{k}$ is the velocity operator. We note that proper operator ordering is still enforced. The second term is the magnetic interaction term

$$H_B = -2\mu_B [\kappa \boldsymbol{J} \cdot \boldsymbol{B} + q \boldsymbol{\mathcal{J}} \cdot \boldsymbol{B}], \tag{B.7}$$

where κ is the isotropic and q the anisotropic part of the hole g-factor, $\boldsymbol{J} = (J_x, J_y, J_z)$ and $\boldsymbol{\mathcal{J}} = (J_x^3, J_y^3, J_z^3)$.

The QD states are then described by

$$H_{qd} = H_k + H_\varepsilon + V_c + V_{el} + H_{mc} + H_B. \tag{B.8}$$

We subdivide H_{qd} into a leading order term

$$H_{qd,0} = H_{k,0} + H_{\varepsilon,0} + V_c + V_{el} \tag{B.9}$$

and a perturbation $H_{qd,1}$. The Hamiltonian $H_{k,0} + V_c + V_{el}$ can be directly mapped onto a three-dimensional, anisotropic harmonic oscillator with an energy shift and a coordinate shift along z, both introduced by V_{el}. The eigenenergies E_j in band j are given by

$$\begin{aligned} E_j &= \frac{1}{2}\frac{(F_z e)^2}{m_{j,\perp}\omega_{j,\perp}^2} - \hbar\omega_{j,\perp}(n_z + \frac{1}{2}) \\ &\quad -\hbar\omega_{j,\parallel}(n_x + n_y + 1). \end{aligned} \tag{B.10}$$

The associated eigenfunctions are the usual three dimensional harmonic oscillator eigenfunctions $\phi_{j,\boldsymbol{n}}(x, y, z_j)$, where $\boldsymbol{n} = (n_x, n_y, n_z)$ is a vector of the associated quantum numbers and $z_j = z - F_z e/(m_{j,\perp}\omega_{j,\perp}^2)$. We choose the basis states of $H_{qd,0}$ to be products of type $\phi_{j,\boldsymbol{n}}(x, y, z_j)\,|j, m_j\rangle$. We rewrite H_{qd} in terms of these new basis states and obtain $H_{qd,\text{ext}}$.

B.1.2 g-factor

We are interested in the Zeeman splitting of the two lowest HH states, $\phi_{\text{HH},\mathbf{0}}\,|3/2, 3/2\rangle$ and $\phi_{\text{HH},\mathbf{0}}\,|3/2, -3/2\rangle$. These states are decoupled from the higher energy states in $H_{qd,\text{ext}}$ by a Schrieffer-Wolff transformation (SWT) of the form $\tilde{H}_{qd,\text{ext}} = e^{-S} H_{qd,\text{ext}} e^{S}$, where $S = -S^\dagger$ is an anti-Hermitian operator. The exact procedure is described in detail e.g. in Ref. [1]. We perform the SWT up to second order and, by projecting on $\{\phi_{\text{HH},\mathbf{0}}\,|3/2, 3/2\rangle\,, \phi_{\text{HH},\mathbf{0}}\,|3/2, -3/2\rangle\}$, we obtain an effective, 2×2 Hamiltonian H_{eff}. The single elements of H_{eff} turn out to be too lengthy to be written down here explicitly. Exact diagonalization of H_{eff} gives two eigenenergies, $E_\Uparrow$ and $E_\Downarrow$, from which we calculate g according to

$$g_h^x = \frac{E_\Uparrow - E_\Downarrow}{\mu_B |\boldsymbol{B}|}. \tag{B.11}$$

B.1.3 Hole Position and Material Parameters

The applied electric field $\boldsymbol{F}$ shifts the hole position within the QD along z. Since the QD has an In concentration gradient in the growth direction, the hole experiences an electric-field dependent local material composition. A linear interpolation of the InAs and GaAs material parameters is insufficient to describe ternary alloys. Instead, the gap energy and other band parameters such as the HH mass along [001] and κ are given by a quadratic form [6, 7], where a bowing parameter is introduced to represent the deviation from a linear dependence on composition. We take into account the bowing of the HH mass along z and calculate the hole position within the QD as a function of the applied electric field, $z_{\mathrm{HH}}(F_z)$. This is carried out by minimizing the parabolic part of the HH confinement potential in z direction,

$$\frac{1}{2} m_{\mathrm{HH},\perp} \omega_{\mathrm{HH},\perp}^2 \left[z - \frac{eF_z}{m_{\mathrm{HH},\perp} \omega_{\mathrm{HH},\perp}^2} \right]^2 . \tag{B.12}$$

We express the local material composition in terms of the hole position and model the material parameters as functions of $z_{\mathrm{HH}}(F_z)$. Inserting these material parameters in Eq.(B.11) results in $g = g(F_z)$. We observe that the slope of $g(F_z)$ depends strongly on the confinement length a, a smaller a corresponding to a flatter QD and less admixture of the LH states to the effective HH states. This effect can be exploited to tailor the observed electric field dependence of g by choosing an appropriate QD height. The confinement lengths are taken according to the values measured on very similar quantum dots, $a = 2.4$ nm [8] and $L = 4.6$ nm [9]. We take for these In-flushed QDs the In concentration of $\sim 40\%$ at the bottom and $\sim 60\%$ at the top of the QD. The change in In concentration is taken from structural measurements on flushed $In_{0.5}Ga_{0.5}As_{0.5}$ QDs [10–12]. In our case, the average In concentration is higher as the pre-flush In concentration is higher. We estimate the average In concentration to be $\sim 50\%$. The average In concentration in combination with the strain parameters for quantum wells ($\varepsilon_{xx} = a_0(\mathrm{GaAs})/a_0(\mathrm{In_{0.5}Ga_{0.5}As}) - 1$) lead to an estimated strain $\varepsilon_{xx} = \varepsilon_{yy} = -\varepsilon_{zz} = -0.035$ of the system. The material parameters (see Table B.1) were modified by the corresponding bowing parameters [6, 7] where available. Note that the values of q reported in the literature [1, 13–15] vary e.g. for GaAs between $q_{\mathrm{GaAs}} = 0.01 - 0.04$, meaning that, dependent on q, different choices of strain distribution, QD geometry and In profile may produce the same curve.

	GaAs	InAs
κ	1.1[6]	7.68[6]
q	0.01[16]	0.04[13]
γ_1	6.85	20.40
γ_2	2.10	8.30
γ_3	2.90	9.10

		GaAs	InAs
C_k	[eVÅ]	-0.0034	-0.0112
D_d	[eV]	-1.16[7]	-1.0[7]
D_u	[eV]	3.0	2.7
C_4	[eVÅ]	6.8[17]	7.0[17]

Table B.1 | Material parameters used in this work. If not stated otherwise, the parameters were taken from Ref. [1].

References

[1] R. Winkler, *Spin-Orbit Coupling Effects in Two-Dimensional Electron and Hole Systems* (Springer Verlag, Berlin, 2003).

[2] M. Tadić, F. M. Peeters, K. L. Janssens, M. Korkusiński, and P. Hawrylak, J. Appl. Phys. **92**, 5819 (2002).

[3] H. R. Trebin, U. Rössler, and R. Ranvaud, Phys. Rev. B **20**, 686 (1979).

[4] E. Ivchenko and A. Kiselev, JETP Lett. **67**, 43 (1998).

[5] A. A. Kiselev, E. L. Ivchenko, and U. Rössler, Phys. Rev. B **58**, 16353 (1998).

[6] N. J. Traynor, R. T. Harley, and R. J. Warburton, Phys. Rev. B **51**, 7361 (1995).

[7] I. Vurgaftman, J. R. Meyer, and L. R. Ram-Mohan, J. Appl. Phys. **89**, 5815 (2001).

[8] R. J. Warburton, C. Schulhauser, D. Haft, C. Schäflein, K. Karrai, J. M. Garcia, W. Schoenfeld, and P. M. Petroff, Phys. Rev. B **65**, 113303 (2002).

[9] B. D. Gerardot, S. Seidl, P. A. Dalgarno, R. J. Warburton, D. Granados, J. M. Garcia, K. Kowalik, O. Krebs, K. Karrai, A. Badolato, and P. M. Petroff, Appl. Phys. Lett. **90**, 041101 (2007).

[10] J. P. McCaffrey, M. D. Robertson, S. Fafard, Z. R. Wasilewski, E. M. Griswold, and L. D. Madsen, J. Appl. Phys. **88**, 2272 (2000).

[11] V. Jovanov, T. Eissfeller, S. Kapfinger, E. C. Clark, F. Klotz, M. Bichler, J. G. Keizer, P. M. Koenraad, M. S. Brandt, G. Abstreiter, and J. J. Finley, Phys. Rev. B **85**, 165433 (2012).

[12] J. G. Keizer, M. Bozkurt, J. Bocquel, T. Mano, T. Noda, K. Sakoda, E. C. Clark, M. Bichler, G. Abstreiter, J. J. Finley, W. Lu, T. Rohel, H. Folliot, N. Bertru, and P. M. Koenraad, J. Appl. Phys. **109**, 102413 (2011).

[13] P. Lawaetz, Phys. Rev. B **4**, 3460 (1971).

[14] S. Glasberg, H. Shtrikman, I. Bar-Joseph, and P. C. Klipstein, Phys. Rev. B **60**, R16295 (1999).

[15] I. Toft and R. T. Phillips, Phys. Rev. B **76**, 033301 (2007).

[16] H. Mayer and U. Rössler, Phys. Rev. B **44**, 9048 (1991).

[17] M. Silver, W. Batty, A. Ghiti, and E. P. O'Reilly, Phys. Rev. B **46**, 6781 (1992).

Appendix C

Supplementary information to Chapter 7 "The decoupling of the hole spin from the nuclear spins"

Adapted from:

Jonathan H. Prechtel, Andreas V. Kuhlmann, Julien Houel, Arne Ludwig, Andreas D. Wieck and Richard J. Warburton

"The hole spin qubit: decoupling from the nuclear spins"

Submitted manuscript

In Chapter 7 we show that the hole spins in our quantum devices are highly decoupled from the nuclear spins in an in-plane magnetic field. We use a very sensitive optical probe, the narrow dip of the two-photon resonance in a two-laser pump-probe experiment. In the supplementary information we explain the sample structure in detail, the density matrix approach to model the coherent population trapping (CPT) signal and the data processing.

C.1 The semiconductor p-doped quantum dot Sample

The quantum device used to probe the nuclear spin – hole spin interaction is a quantum dot (QD) sample grown by molecular beam epitaxy. The data presented in Chapter 7 were measured on two QDs, one from the n-i-p structure (sample A) and one from the Schottky diode structure (sample B).

In sample B, the self-assembled QDs are embedded in a p-doped Schottky diode [1, 2] as shown in Fig. C.1(a). The order of the layers in sample B is:

1. *substrate*
   50 nm i-GaAs
2. *"cleaning" superlattice*
   30 periods AlAs/GaAs 2 nm/2 nm
3. *buffer layer*
   50 nm i-GaAs
4. *back contact*
   50 nm p^+-GaAs, C-doping level $\sim 2.0\times10^{18}$ cm^{-3}
5. *tunnelling barrier*
   25 nm i-GaAs
6. *active layer*
   InGaAs QDs (diameter $\sim$ 20 nm, height $\sim$ 5 nm) with centre wavelength 950 nm.
7. *capping layer*
   10 nm i-GaAs
8. *blocking barrier*
   111 periods AlAs/GaAs 3 nm/1 nm
9. *cap*
   10 nm i-GaAs
10. *Schottky gate*
    6 nm Au

Sample A (n-i-p-structure) is inverted and uses epitaxial gates, with a tunnel barrier also of 25 nm i-GaAs. This sample is described in detail in Chapter 4.

The background doping of as-grown GaAs is p $\sim 2.5 \times 10^{13}\,cm^{-3}$; two-dimensional electron gases grown under similar conditions at 4.2 K have mobilities $> 5 \times 10^6\,cm^2/Vs$.

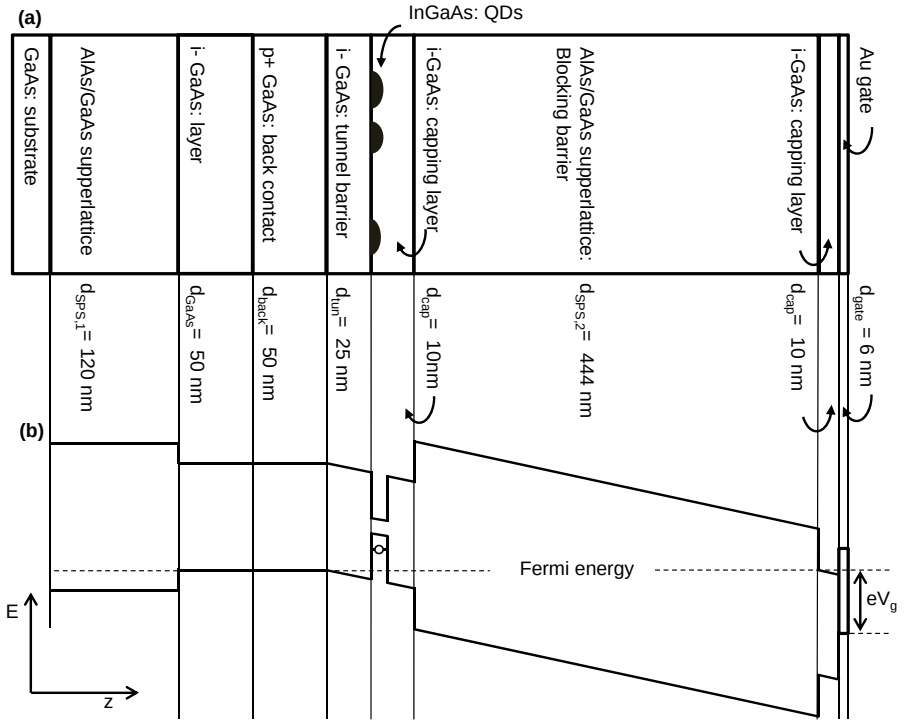

Figure C.1 | (a) Structure of sample B and (b) the corresponding energy band diagram. The Fermi energy is pinned to the valence band edge of the back contact by the high doping. The figures are to scale with respect to length.

C.1.1 dc Stark shift

The number of positive carriers (holes) confined to the QD can be precisely controlled by the gate voltage V_g: the device works in the Coulomb blockade regime. A change of gate voltage yields a change of the QD's local potential ϕ by

$$\Delta\phi = \frac{\Delta V_g}{\lambda} \tag{C.1}$$

where λ denotes the sample's lever arm, defined as the ratio of back contact to gate distance d and tunnel barrier thickness. For sample A, $\lambda = 12.98$ and for sample B, $\lambda = 19.56$. The exciton energy E is detuned with respect to the constant laser photon energy by exploiting the dc Stark effect,

$$\Delta E = p\Delta F, \quad \Delta F = \frac{\Delta V_g}{d} \tag{C.2}$$

with Stark shift coefficient (dipole moment) p and electric field F. The Stark shift is determined by recording the resonance position in V_g for several laser frequencies, the laser frequency measured in each case with an ultra-precise wavemeter. The Stark shift is linear in ΔF for

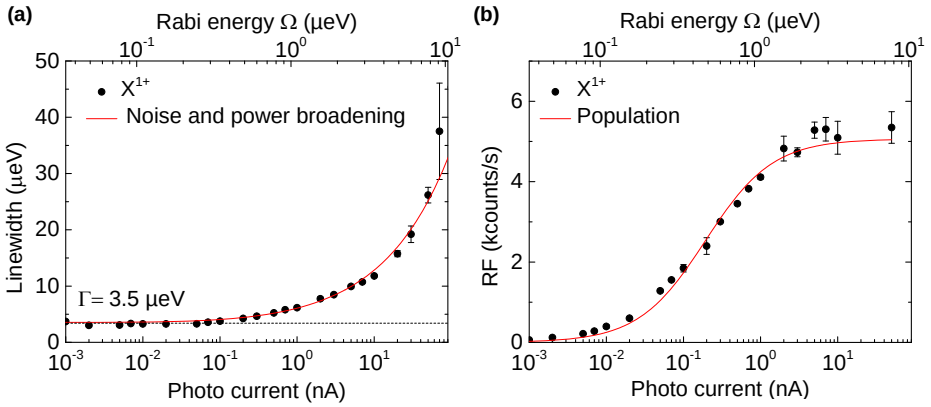

Figure C.2 | Power broadening: X^{1+} power dependence on sample B. (a) RF linewidth versus in situ photodiode measurement on the laser power. The fit to the two-level model uses parameters $\gamma = 2.85 \pm 0.05$ μeV, radiative linewidth of the exciton $\Gamma_{21} = 0.68 \pm 0.1$ μeV and $\gamma_2 \leq 0.1$ μeV. The resulting relation between the Rabi coupling and the photo current ($I = \alpha\Omega^2$) is $\alpha = 0.833$ nA/μeV^2. (b) Maximum RF counts versus photodiode current. The line is the fit to the two-level model with $\mathrm{RF} = \mathrm{RF}_0\rho_{22}$. The fit results in the same α as the linewidth dependence, including the additional parameter $\mathrm{RF}_0 = 47 \pm 1$ kcts/s.

the small range of V_g used here. For sample A we determine a Stark shift for the positively charged trion X^{1+} of $p = 0.0165$ μeV cm/V and for sample B, 0.0076 μeV cm/V.

C.1.2 Rabi couplings

The Rabi couplings in the quantum devices are determined by taking advantage of the dependence of the optical resonance linewidth on the resonant excitation power. In an ideal 2-level system, the power broadening effect increases the optical linewidth [3]. For the resonantly driven system, the total decoherence rate of the upper level is $\Gamma_0 = \Gamma_{21} + \gamma_2$, where Γ_{21} corresponds to the radiative decay ($\Gamma_{21} = \hbar/\tau_r$) and γ_2 the pure dephasing of the upper level. The optical linewidth Γ and the population of the upper level ρ_{22} at zero detuning for the two level system are [3]

$$\Gamma = \sqrt{\Gamma_0^2 + 2\Omega^2\left(1 + \frac{\gamma_2}{\gamma_{21}}\right)} + \gamma \tag{C.3}$$

and

$$\rho_{22} = \frac{\Omega^2}{\Gamma_{21}\Gamma_0^2 + 2\Omega^2} \cdot \frac{\Gamma - \gamma}{\Gamma}. \tag{C.4}$$

The inhomogeneous broadening of the linewidth is included with the term γ which describes a spectral fluctuation with a Lorentzian probability distribution. The experimental data (linewidth, RF signal at the resonance) are both described by (Γ, ρ_{22}) with the same parameter set.

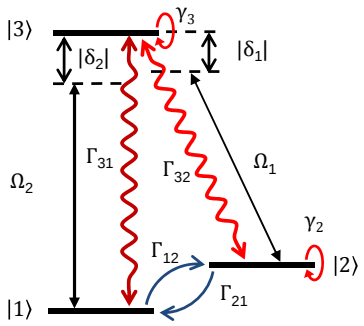

Figure C.3 | 3-level Λ-system. The energetically split ground state levels $|1\rangle$ and $|2\rangle$ are coupled by two optical fields Ω_1 and Ω_2, respectively, to a common upper level, $|3\rangle$. All incoherent decay processes (radiative decay, spin relaxation, exciton dephasing and spin dephasing) are included.

The conversion of the power measured in transmission to the Rabi energy can be determined by fitting to both linewidth and RF signal, Fig. C.2(a),(b). The pure dephasing turns out to be negligible: $\gamma_2 \ll \Gamma_{21}$.

A phonon-induced dephasing process as observed at very high Rabi couplings [4] and in pulsed experiments [5] is negligible at these Rabi couplings.

C.2 Theoretical model

The resonance fluorescence experiment is described by means of the density matrix formalism [6] including a Markovian coupling to the environment via the Lindblad formalism [7]. The master equation is solved in the steady state limit and the dependence of the population of the upper level on the probe laser detuning is calculated numerically in order to simulate the probe spectrum. We solve the equations numerically: we do not rely on the results in the perturbative limit. Spectral fluctuations of the exciton are taken into account via a convolution of the density matrix result with a Lorentzian function, thereby accounting for the measured RF linewidths [8]. Finally, the mutual coherence of the two lasers used in the experiments is also included in the model, again with a convolution.

C.2.1 Density matrix formalism 3-level system

The Hamiltonian of a 3-level Λ-system in Fig. C.3 is a combination of the bare QD state energies and the interactions induced by the laser fields (semiclassical approximation).

$$\begin{aligned} H &= H_0 + H_{\text{int}} \\ H_0 &= \hbar\omega_1 |1\rangle\langle 1| + \hbar\omega_2 |2\rangle\langle 2| + \hbar\omega_3 |3\rangle\langle 3| \end{aligned} \tag{C.5}$$

The interaction part of the Hamiltonian, which contains the interaction of the optical field of the laser with the QD, is given by

$$H_{\text{int}} = -\boldsymbol{dE}. \tag{C.6}$$

The interaction is described by the dipole approximation, including the optical excitation field:

$$\boldsymbol{E} = E_0 \cdot \cos(\omega_{\text{ex}} t) = \frac{1}{2}\left(e^{i\omega_{\text{ex}} t} + e^{-i\omega_{\text{ex}} t}\right) E_0 \tag{C.7}$$

with the field amplitude E_0 and the frequency of the excitation laser ω_{ex}. We take the optical field inside the interaction part of the Hamiltonian as linearly polarized along the x-direction, because of the excitation axis of the microscope head [9]. Therefore the dipole moment between the ground $|1\rangle$ and excited state $|3\rangle$ can be written as

$$\begin{aligned} H_{\text{int}} &= -\boldsymbol{d}\cdot\boldsymbol{E} = -exE \\ &= -e(|3\rangle\langle 1|\, x_{13} + |1\rangle\langle 3|\, x_{31})E \\ &= -(|3\rangle\langle 1| + |1\rangle\langle 3|)d_x E, \end{aligned} \tag{C.8}$$

with $d_x = ex_{31}$ as the matrix element of the atomic dipole moment and $x_{11} = x_{33} = 0$, and the electric field E. The parameters d_x and x_{31} are assumed to be real. The Rabi frequency Ω is a general representation of the coupling strength between the quantum states and the driving source, the optical excitation is defined as

$$\Omega_{\text{ex}} = d_x E_0/\hbar. \tag{C.9}$$

Hence the interaction Hamiltonian becomes

$$H_{\text{int}} = -\frac{\hbar}{2}\Omega_{\text{ex}}\big(\,|3\rangle\langle 1| + |1\rangle\langle 3|\,\big)\big(e^{i\omega_{\text{ex}} t} + e^{-i\omega_{ex} t}\big) \tag{C.10}$$

In the Heisenberg presentation the transition operators $|3\rangle\langle 1|$ and $|1\rangle\langle 3|$ oscillate with $e^{i\omega_{31}t}$ and $e^{-i\omega_{31}t}$, respectively. This results in quickly varying terms $e^{i(\omega_{31}+\omega_{\text{ex}})t}$ and $e^{-i(\omega_{31}+\omega_{\text{ex}})t}$, which are neglected via the rotating-wave approximation. This two terms correspond the fact of photon emission while population creation, and photon absorption while population

annihilation. Applying equally considerations for a second laser field, the Hamiltonian for the three level system in Fig. C.3 under pump-probe excitation becomes:

$$\begin{aligned} H &= H_0 + H_{\text{int}} \\ &= \frac{\hbar}{2}\begin{pmatrix} 0 & 0 & \Omega_2 e^{i\omega_2 t} \\ 0 & 2\omega_{12} & \Omega_1 e^{i\omega_1 t} \\ \Omega_2 e^{-i\omega_2 t} & \Omega_1 e^{-i\omega_1 t} & 2\omega_{13} \end{pmatrix} \end{aligned} \tag{C.11}$$

The diagonal terms represent the energy difference between the states $|1\rangle$ and $|2\rangle$ ($\hbar\omega_{12}$) and between the states $|1\rangle$ and $|3\rangle$ ($\hbar\omega_{13}$). The Rabi couplings of the probe and pump laser are Ω_1 and Ω_2, respectively.

The Schrödinger equation for this Hamiltonian

$$i\hbar\frac{\partial}{\partial t}|\Psi\rangle = \hat{H}|\Psi\rangle \tag{C.12}$$

leads to the coupled equations:

$$i\hbar\begin{pmatrix} \dot{c}_1 \\ \dot{c}_2 \\ \dot{c}_3 \end{pmatrix} = \frac{\hbar}{2}\begin{pmatrix} 0 & 0 & \Omega_2 e^{i\omega_2 t} \\ 0 & 2\omega_{12} & \Omega_1 e^{i\omega_1 t} \\ \Omega_2 e^{-i\omega_2 t} & \Omega_1 e^{-i\omega_1 t} & 2\omega_{13} \end{pmatrix} \cdot \begin{pmatrix} c_1 \\ c_2 \\ c_3 \end{pmatrix}, \tag{C.13}$$

where $|\Psi\rangle = \sum_i c_i |i\rangle$. The diagonal terms represent the energy difference between the states $|1\rangle$ and $|2\rangle$ ($\hbar\omega_{12}$) and between the states $|1\rangle$ and $|3\rangle$ ($\hbar\omega_{13}$). The Rabi couplings of the probe and pump laser are Ω_1 and Ω_2, respectively. The Hamiltonian exhibits a time dependence via the coherent optical excitation. Changing the system to the rotating frame of the laser eliminates this dependence. The new variables $((\tilde{c}_1, \tilde{c}_2, \tilde{c}_3))$ in the rotating frame are:

$$\begin{aligned} c_1 &= \tilde{c}_1 & \dot{c}_1 &= \dot{\tilde{c}}_1 \\ c_2 &= \tilde{c}_2 e^{-i(\omega_2-\omega_1)t} & \dot{c}_2 &= [\dot{\tilde{c}}_2 - i(\omega_2-\omega_1)\tilde{c}_2]e^{-i(\omega_2-\omega_1)t} \\ c_3 &= \tilde{c}_3 e^{-i\omega_2 t} & \dot{c}_3 &= [\dot{\tilde{c}}_3 - i\omega_2\tilde{c}_3]e^{-i\omega_2 t} \end{aligned} \tag{C.14}$$

The new time-independent Hamiltonian follows inserting Eq. C.14 into Eq. C.13

$$i\hbar\begin{pmatrix} \dot{\tilde{c}}_1 \\ \dot{\tilde{c}}_2 \\ \dot{\tilde{c}}_3 \end{pmatrix} = \frac{\hbar}{2}\begin{pmatrix} 0 & 0 & \Omega_2 \\ 0 & 2(\delta_1-\delta_2) & \Omega_1 \\ \Omega_2 & \Omega_1 & -2\delta_2 \end{pmatrix} \cdot \begin{pmatrix} \tilde{c}_1 \\ \tilde{c}_2 \\ \tilde{c}_3 \end{pmatrix} \tag{C.15}$$

Here $\delta_2 = \omega_2 - \omega_{13}$ and $\delta_1 = \omega_1 - \omega_{23}$ are the detunings of the pump and probe laser frequencies with respect to the corresponding transition.

The density matrix formalism is a convenient way to solve the Schrödinger equation. This formalism describes the mixed state, a statistical ensemble of quantum states, with the density operator defined as

$$\hat{\rho} = \sum_k^N p_k \left|\psi_k\right\rangle \left\langle\psi_k\right| . \tag{C.16}$$

The Schrödinger equation transforms with the density matrix of Eq. C.16 to

$$i\hbar \frac{\partial}{\partial t}\hat{\rho} = [\hat{H}, \hat{\rho}] \tag{C.17}$$

There are two physical meanings of the density matrix elements. The diagonal elements ρ_{nn} correspond to the population in the state $|\psi_n\rangle$, whereas the off-diagonal elements ρ_{nm} are the coherences between the two states.
The density matrix formalism takes the coherent and non-coherent properties of the QD into account. The combined master equation is the von Neumann equation. The coherent system is given with the Hamiltonian Eq. C.15. Non-coherent relaxation and dephasing processes are included via the Lindblad formalism.

$$\frac{\partial}{\partial t}\hat{\rho} = \Lambda\hat{\rho} \tag{C.18}$$

The Lindblad operator Λ is defined as [7]

$$\Lambda\hat{\rho} = \sum_{ij}^N [\gamma_{ij} \left|j\right\rangle \left\langle i\right| \hat{\rho} \left|i\right\rangle \left\langle j\right| - \frac{\gamma_{ij}}{2}(\left|j\right\rangle \left\langle j\right| \hat{\rho} + \hat{\rho} \left|i\right\rangle \left\langle i\right|))]. \tag{C.19}$$

The extended von Neumann equation including both, the coherent and the non-coherent, processes is

$$i\hbar \frac{\partial}{\partial t}\hat{\rho} = [H, \hat{\rho}] + i\Lambda\hat{\rho} \tag{C.20}$$

The following non-coherent processes are included (Fig. C.3): radiative decay from $|3\rangle$ to $|2\rangle$ (rate Γ_{32}) and from $|3\rangle$ to $|1\rangle$ (rate Γ_{31}); relaxation between the hole spin ground states $|2\rangle$ and $|1\rangle$ (in both directions, rates Γ_{21} and Γ_{12}); pure hole spin dephasing (of state $|2\rangle$ at rate γ_2); pure electron spin dephasing (of state $|3\rangle$ at rate γ_3).

The master equation, Eq. C.20, results in 9 equations, the optical Bloch equations for this 3-level atom:

$$
\begin{aligned}
i\dot{\rho}_{11} &= \frac{1}{\hbar}\left[\frac{\Omega_2}{2}\big(\rho_{31}-\rho_{13}\big)+i\big(\rho_{33}\Gamma_{31}+\rho_{22}\Gamma_{21}-\rho_{11}\Gamma_{12}\big)\right]\\
i\dot{\rho}_{22} &= \frac{1}{\hbar}\left[\frac{\Omega_1}{2}\big(\rho_{32}-\rho_{23}\big)+i\big(\rho_{33}\Gamma_{32}-\rho_{22}\Gamma_{21}+\rho_{11}\Gamma_{12}\big)\right]\\
i\dot{\rho}_{33} &= \frac{1}{\hbar}\left[\frac{\Omega_1}{2}\big(\rho_{23}-\rho_{32}\big)+\frac{\Omega_2}{2}\big(\rho_{13}-\rho_{31}\big)-i\rho_{33}\big(\Gamma_{31}+\Gamma_{32}\big)\right]\\
i\dot{\rho}_{12} &= \frac{1}{\hbar}\left[\frac{\Omega_2}{2}\rho_{32}-\frac{\Omega_1}{2}\rho_{13}+\rho_{12}\big(\delta_2-\delta_1-\frac{i}{2}\big(\Gamma_{12}+\Gamma_{21}+\gamma_2\big)\big)\right]\\
i\dot{\rho}_{13} &= \frac{1}{\hbar}\left[\frac{\Omega_2}{2}\big(\rho_{33}-\rho_{11}\big)-\frac{\Omega_1}{2}\rho_{12}+\rho_{13}\big(\delta_2-\frac{i}{2}\big(\Gamma_{12}+\Gamma_{31}+\Gamma_{32}+\gamma_3\big)\big)\right]\\
i\dot{\rho}_{23} &= \frac{1}{\hbar}\left[\frac{\Omega_1}{2}\big(\rho_{33}-\rho_{22}\big)-\frac{\Omega_2}{2}\rho_{21}+\rho_{23}\big(\delta_1-\frac{i}{2}\big(\Gamma_{21}+\Gamma_{31}+\Gamma_{32}+\gamma_2+\gamma_3\big)\big)\right]\\
i\dot{\rho}_{21} &= \frac{1}{\hbar}\left[-\frac{\Omega_2}{2}\rho_{23}+\frac{\Omega_1}{2}\rho_{31}+\rho_{21}\big(-\delta_2+\delta_1-\frac{i}{2}\big(\Gamma_{12}+\Gamma_{21}+\gamma_2\big)\big)\right]\\
i\dot{\rho}_{31} &= \frac{1}{\hbar}\left[\frac{\Omega_2}{2}\big(\rho_{11}-\rho_{33}\big)+\frac{\Omega_1}{2}\rho_{21}-\rho_{31}\big(\delta_2+\frac{i}{2}\big(\Gamma_{12}+\Gamma_{31}+\Gamma_{32}+\gamma_3\big)\big)\right]\\
i\dot{\rho}_{32} &= \frac{1}{\hbar}\left[\frac{\Omega_1}{2}\big(\rho_{22}-\rho_{33}\big)+\frac{\Omega_2}{2}\rho_{12}-\rho_{32}\big(\delta_1+\frac{i}{2}\big(\Gamma_{21}+\Gamma_{31}+\Gamma_{32}+\gamma_2+\gamma_3\big)\big)\right]
\end{aligned}
\tag{C.21}
$$

The system of linear Bloch equations is solved, for instance for the population ρ_{33} of the upper state $|3\rangle$, in the steady state ($t \to \infty$):

$$\mathrm{RF}(\delta_2, \delta_1) = \beta_{\mathrm{RF}}\rho_{33}. \tag{C.22}$$

where β_{RF} is a scaling factor to link the calculated population to the signal in the experiment.

C.2.2 Coherent population trapping model

Coherent population trapping is a spectroscopic quantum interference phenomenon which arises in a three level Λ-system like the one in Fig. C.3. The two ground states $|1\rangle$ and $|2\rangle$ are coupled individually to a common upper level $|3\rangle$ by a "pump" and a "probe" laser with the Rabi couplings Ω_2 and Ω_1. The two-photon resonance is fulfilled when the frequency difference of the two lasers is equal to the Zeeman–splitting of the ground states. Then a "dark" state is formed, a superposition of the two ground states with no amplitude from the common upper level. The signature of the dark state in optical spectroscopy measurements is a dip in the resonance fluorescence signal or in the probe absorption spectrum. The dip "visibility" is a sensor of the hole spin coherence in the ground state [8, 10]. The dip depth is sensitive to the

coherence time T_2 of the hole spin (see Chapter 2 and for a coherent spin ($1/T_2 \ll \Omega_2^2/\Gamma_r$) the dip goes to zero. An increase in the dip width can be associated with ensemble averaging (i.e. the dephasing time T_2^*) resulting from a fluctuating dip position.

In a semiconductor device the inherent charge noise [11] leads to a broadening of the exciton resonance, term γ in Eq. C.3, a fluctuation in the energy of the upper level. However the ground state coherence in the form of the CPT dip prevails [8]. The dark state is robust even if the upper level is shifted by an energy y as in this case the pump and the probe detunings both experience the same shift. However, the spectral fluctuations have a significant influence on the CPT envelope [8] and are included by convolution of the density matrix calculations with a probability distribution $L_1(y)$:

$$\mathrm{CPT}(\delta_2, \delta_1) = \beta_{\mathrm{RF}} \int \rho_{33}\big(\delta_2 - y, \delta_1 - y\big) L_1(y) dy \tag{C.23}$$

$L_1(y)$ represents a Lorentzian function reflecting the Lorentzian RF experimental lineshapes.

Finally, a second convolution is required to account for the finite mutual coherence of the pump and probe lasers:

$$\mathrm{CPT}'(\delta_2, \delta_1) = \int \mathrm{CPT}\big(\delta_2, \delta_1 - x\big) L_2(x) dx \tag{C.24}$$

In the mathematics we assign the laser phase noise to the probe laser only. The measured mutual coherence of the two lasers is a Lorentzian function $L_2(y)$ with a linewidth of 2.0 MHz (8.2 neV).

The Λ-system modelled so far consists of three energy levels. A real X^{1+} in an in-plane magnetic field is a more complex 4-level system. The 3-level system is adequate under certain conditions. First, the Λ-system description is valid for a small detuning range near the two photon resonance where the spectrally well-separated fourth level has no influence. Secondly, the model assumes that the pump couples $|1\rangle \leftrightarrow |3\rangle$ but not $|1\rangle \leftrightarrow |2\rangle$. This second condition is met well for sample A but not for sample B. In sample B, the hole Zeeman splitting is rather small, just 6.2 µeV at 3.00 T. A pump laser tuned into resonance with $|1\rangle \leftrightarrow |3\rangle$ results additionally to a weak coupling $|1\rangle \leftrightarrow |2\rangle$. (Note that to detect RF with our dark–field technique, the pump and probe laser have the same polarization.) This unwanted coupling reduces our ability to achieve high fidelity spin pumping [12] and it also reduces the lifetime of the dark state. This issue is important for sample B but much less so for sample A. A complete theoretical description involves four levels and three laser couplings. A rotating frame does not exist and the problem is complex. We can safely use the 3-level model for sample A; we can safely extract Z_h from sample B and we include here the additional coupling in an ad hoc manner described below.

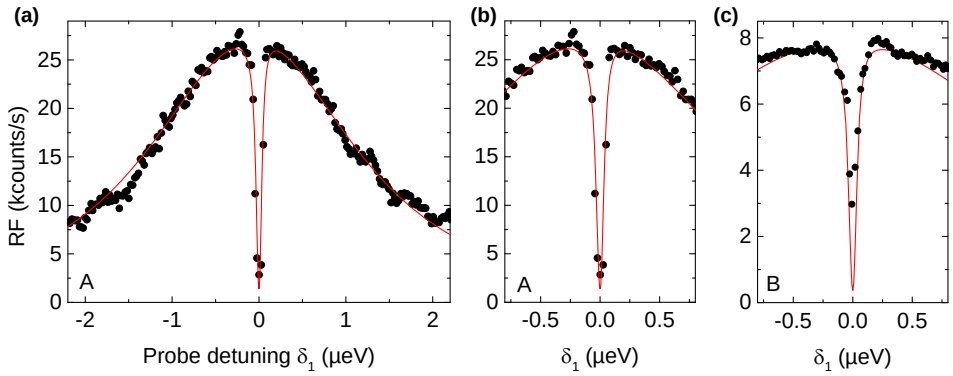

Figure C.4 | (a) CPT resonance of sample A (n-i-p) with the density matrix model (red line) using $\Omega_2 = 0.40$, $\delta_2 = 0.1$ µeV and $\Omega_1 = 0.06$ µeV. δ_1 is tuned with respect to the pump frequency. (b) Zoom-in of the CPT dip. (c) CPT dip of Sample B (p-i-Schottky) with the density matrix model (red line) using $\Omega_2 = 0.49, \delta_2 = 0.0$ µeV and $\Omega_1 = 0.049$ µeV.

The parameters in the equations for the density matrix are now linked to the experiment. The Rabi energies of the probe and the pump laser, $\hbar\Omega_1$ and $\hbar\Omega_2$, respectively, are experimentally determined by power broadening fits of the linewidth and the count rates of an 2-level system (see the section on Rabi couplings). The radiative decay rates are set to be equal and half of the radiative decay of the positive charged exciton X^{1+} ($\Gamma_{32} = \Gamma_{31} = \frac{1}{2}\Gamma_r$). Γ_r is determined from the the exciton decay curves after pulsed excitation, 0.7 ± 0.1 µeV [13]. The relaxation time of the hole spins in the ground state is set to be $\Gamma_{12} = \Gamma_{21} = \hbar/T_1$ with $T_1 = 1$ ms [12]. The pure dephasing rate of the ground states γ_2, which represents the decoherence rate of the hole spin, is determined with a lower bound of $T_2 > 1$ µs from different fits to the dip depth. The remaining parameters are dependent on the sample structures, n-i-p-structure (A) and p-i-Schottky (B). The scaling factor β_{RF} (Eq. C.22) is determined by the RF count rate in the experiment. The FWHM of the Lorentzian $L_1(y)$, which describes the exciton linewidth, is 2.5 µeV for the low–noise sample A. Sample B shows a broader linewidth (Fig. C.3), reflecting a higher noise level and the FWHM is 4.0 µeV at 3.00 T. The pure level dephasing of the upper level γ_3 broadens the envelope of the transition. γ_3 is set to zero (sample B), for (A) a small value of 10 ns (0.07 µeV) can be determined from the fit to the RF envelope.

Fig. C.4 shows density matrix model along with the measured RF signals. For sample A, Fig. C.4(a), the model reproduces not just the envelope but also the dip (b) perfectly. For sample B, the fit to the envelope close to the CPT dip is good, but the theory predicts a “deeper” dip than the one observed experimentally, a consequence of the influence of the pump laser on the probe transition, as described below.

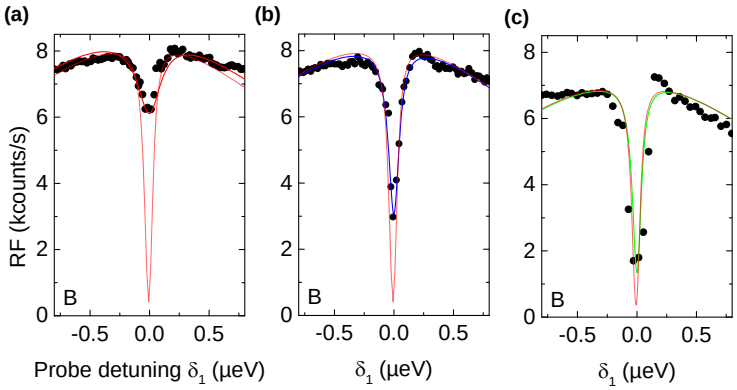

Figure C.5 | CPT data on sample B with different pump detunings, δ_2. (a) $\delta_2 = -1.1$ μeV; (b) $\delta_2 = 0.0$; (c) $\delta_2 = +3.4$ μeV. The data are modeled with the 3-level density matrix system with an artificially lowered T_2 and an adjustment of the fit parameter β_{RF}. In all three cases, $\Omega_2 = 0.49$ μeV and $\Omega_1 = 0.049$ μeV. (a) $T_2 = 4$ ns; (b) $T_2 = 20$ ns; (c) $T_2 = 60$ ns. Each plot shows in addition the calculated result for $T_2 = 1$ μs.

C.3 The CPT dip on sample B

The CPT dip on sample B does not go all the way to zero, Fig. C.4. Fig. C.5 shows how the CPT develops as the pump is detuned. A red-detuned pump worsens the CPT, Fig. C.5(a); a blue-detuned pump improves it, Fig. C.5(c) as compared to the case of zero detuning, Fig. C.5(b).

To shed some light on this behaviour, we explore the details of the dynamic nuclear polarization (DNP). In the regime of dragging, the QD resonance is locked to the laser: DNP is established. This means that the Zeeman splitting of the exciton Z_e depends on the pump detuning δ_2. By probing the lower energy "vertical" transition, this change in Z_e, ΔZ_e, can be measured (Fig. 7.3(a) of Chapter 7). Fig. C.6 plots $-\Delta Z_e/2$ versus δ_2 for sample B. The slope turns out not to be 1 as might be expected for perfect dragging but -0.70. This 0.7 factor is included in the data analysis of Fig. 7.3 in Chapter 7. With this as input, this leads to a simple interpretation of Fig. C.5.

The QD on the p-i-Schottky sample B has a very small hole Zeeman splitting of just 6.2 μeV at 3.00 T, larger than the optical linewidth but not hugely so. The pump drives its own transition on resonance but it can drive also the probe transition weakly: the detuning is insufficient to suppress this coupling completely. One hypothesis is that this unwanted coupling of the probe transition with the pump laser can destroy the dark state. The data in Fig.s C.5 and C.6 are consistent with this hypothesis. On blue-detuning the pump by $\Delta\delta_2$, the upper level of the Λ-system is blue-detuned by $0.70\Delta\delta_2$ such that the detuning of the same laser to the probe transition is increased by $0.30\Delta\delta_2$: the unwanted coupling is lessened, and the CPT

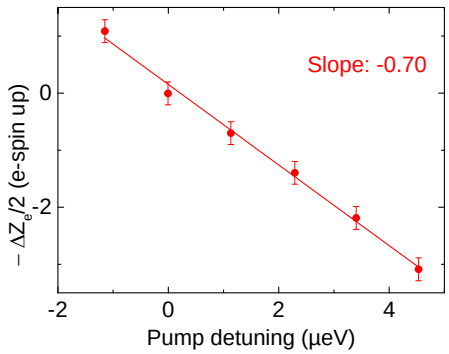

Figure C.6 | Dependence of the lower energy "vertical" transition on pump detuning under dragging for sample B. A linear fit to the data shows that $\Delta Z_e/2 = -0.70\delta_2$.

improves. Conversely, on red-detuning the pump by $\Delta\delta_2$, the upper level of the Λ-system is red-detuned by $0.70\Delta\delta_2$ such that the detuning of the same laser to the probe transition is decreased by $0.30\Delta\delta_2$: the unwanted coupling is increased, and the CPT worsens. The origin of the 0.70 factor is in itself probably related to the unwanted coupling of the probe transition by the pump: it may influence the DNP.

A full model to describe sample B would require a 3-level system with 3 laser couplings and a model to describe the detuning dependence of DNP. This is complex: a rotating frame does not exist; DNP is hard to describe quantitatively. Instead, we take the pragmatic approach of describing the unwanted coupling of the probe transition by the pump laser as a decay mechanism of the dark state: we describe it simply by adjusting the hole spin decoherence time T_2. This is very successful, as shown in Fig. C.5. We would comment that, first, a detailed understanding of DNP is not necessary to deduce the anisotropic part of the hole hyperfine interaction, the main result in Chapter 7. Secondly, these unwanted coupling effects are suppressed in sample A. The gradient of the ΔZ_e versus δ_2 dependence increases to 0.93; the CPT dip is fully formed.

C.4 Stability of the dark state

The assertion of a low-noise device is supported by demonstrating a stable dark state. The robustness of the dark state is probed by stopping the probe laser scanning in the centre of the dip. With constant pump and probe frequencies, the RF signal is then recorded, Fig. C.7. The constant RF signal in Fig. C.7 shows that the hole spin stayed in the dark state throughout.

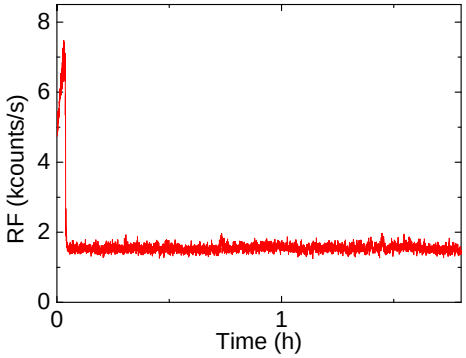

Figure C.7 | Time-dependent representation of a CPT measurement with $\Omega_2 = 0.49$ µeV and $\Omega_1 = 0.049$ µeV. The probe detuning was tuned until the dip centre was reached after which it was held constant. Plotted is the RF signal versus time thereafter. The dark state is maintained over a time exceeding one hour.

References

[1] H. Drexler, D. Leonard, W. Hansen, J. P. Kotthaus, and P. M. Petroff, Phys. Rev. Lett. **73**, 2252 (1994).

[2] R. J. Warburton, C. Schäflein, D. Haft, F. Bickel, A. Lorke, K. Karrai, J. M. Garcia, W. Schoenfeld, and P. M. Petroff, Nature (London) **405**, 926 (2000).

[3] R. Loudon, *The Quantum Theory of Light* (Oxford University Press, 2010).

[4] A. J. Ramsay, A. Gopal, E. M. Gauger, A. Nazir, B. W. Lovett, A. M. Fox, and M. S. Skolnick, Phys. Rev. Lett. **104**, 017402 (2010).

[5] S. M. Ulrich, S. Ates, S. Reitzenstein, A. Löffler, A. Forchel, and P. Michler, Phys. Rev. Lett. **106**, 247402 (2011).

[6] M. Fleischhauer, A. Imamoglu, and J. P. Marangos, Rev. Mod. Phys. **77**, 633 (2005).

[7] G. Lindblad, Comm. Math. Phys. **48**, 119 (1976).

[8] D. Brunner, B. D. Gerardot, P. A. Dalgarno, G. Wüst, K. Karrai, N. G. Stoltz, P. M. Petroff, and R. J. Warburton, Science **325**, 70 (2009).

[9] A. V. Kuhlmann, J. Houel, D. Brunner, A. Ludwig, D. Reuter, A. D. Wieck, and R. J. Warburton, Rev. Sci. Instrum. **84**, 073905 (2013).

[10] A. Imamoglu, Phys. Stat. Sol. (b) **243**, 3725 (2006).

[11] A. V. Kuhlmann, J. Houel, A. Ludwig, L. Greuter, D. Reuter, A. D. Wieck, , M. Poggio, and R. J. Warburton, Nat. Phys. **9**, 570 (2013).

[12] B. D. Gerardot, D. Brunner, P. A. Dalgarno, P. Ohberg, S. Seidl, M. Kroner, K. Karrai, N. G. Stoltz, P. M. Petroff, and R. J. Warburton, Nature (London) **451**, 441 (2008).

[13] P. A. Dalgarno, J. M. Smith, J. McFarlane, B. D. Gerardot, K. Karrai, A. Badolato, P. M. Petroff, and R. J. Warburton, Phys. Rev. B **77**, 245311 (2008).

List of Publications

Publications in journals

1. *Fast Electro-Optics of a Single Self-Assembled Quantum Dot in a Charge-Tunable Device*,
   Jonathan H. Prechtel and Paul A. Dalgarno and Robert H. Hadfield and Jamie McFarlane and Antonio Badolato and Pierre M. Petroff and Richard J. Warburton,
   J. Appl. Phys **111**, 043112 (2012).

2. *A frequency-stabilized source of single photons from a solid-state qubit*,
   Jonathan H. Prechtel, Andreas V. Kuhlmann, Julien Houel, Lukas Greuter, Arne Ludwig, Dirk Reuter, Andreas D. Wieck, and Richard J. Warburton,
   Phys. Rev. X **3**, 041006 (2013).

3. *High resolution coherent population trapping on a single hole spin in a semiconductor*,
   Julien Houel, Jonathan H. Prechtel, Andreas V. Kuhlmann, Daniel Brunner, Christopher E. Kuklewicz, Brian D. Gerardot, Nick G. Stoltz, Pierre M. Petroff, and Richard J. Warburton,
   Phys. Rev. Lett. **112**, 107401 (2014).

4. *Electrically-tunable hole g-factor of an optically-active quantum dot for fast spin rotations*,
   Jonathan H. Prechtel, Franziska Maier, Julien Houel, Andreas V. Kuhlmann, Arne Ludwig, Andreas D. Wieck, Daniel Loss and Richard J. Warburton,
   Phys. Rev. B **91**, 165304 (2015)

5. *Transform-limited single photons from a single quantum dot*,
   Andreas V. Kuhlmann, Jonathan H. Prechtel, Julien Houel, Arne Ludwig, Dirk Reuter, Andreas D. Wieck and Richard J. Warburton,
   Submitted manuscript, arXiv:1307.7109v2 (2015).

6. *The hole spin qubit: decoupling from the nuclear spins*,
   Jonathan H. Prechtel, Andreas V. Kuhlmann, Julien Houel, Arne Ludwig, Andreas D. Wieck, and Richard J. Warburton,
   Submitted Manuscript.

7. *The positively charged exciton in a low-noise InGaAs quantum dot heterostructure*,
   Jonathan H. Prechtel, Andreas V. Kuhlmann, Julien Houel, Arne Ludwig, Andreas D. Wieck, and Richard J. Warburton,
   Unpublished Manuscript.

International conference contributions

1. *A wavelength stabilized source of single photons from a quantum dot*,
   Jonathan H. Prechtel, Julien Houel, Andreas V. Kuhlmann, Lukas Greuter, Arne Ludwig, Dirk Reuter, Andreas D. Wieck, and Richard J. Warburton,
   31st International Conference on the Physics of Semiconductors 2012 (ICPS12), Zürich, Switzerland (Poster)

2. *Massively voltage-tunable hole g-factor of an optically-active quantum dot*
   Jonathan H. Prechtel, Franziska Meier, Julien Houel, Andreas V. Kuhlmann, Arne Ludwig, Dirk Reuter, Andreas D. Wieck, D. Loss and Richard. J. Warburton,
   7th International Conference on Spintronics and Quantum Information Technology 2013 (Spintech VII), Chicago, IL (Poster)

3. *Frequency-stabilized source of single photons from a single quantum dot*
   Jonathan H. Prechtel, Andreas V. Kuhlmann, Julien Houel, Arne Ludwig, Andreas D. Wieck and Richard J. Warburton,
   8th International Conference on Quantum Dots 2014 (QD2014), Pisa, Italy (Poster)

4. *Coherent population trapping on a single hole spin in a semiconductor quantum dot*
   Jonathan Prechtel, Andreas V. Kuhlmann, Julien Houel, Arne Ludwig, Andreas D. Wieck, and Richard J. Warburton,
   32nd International Conference on the Physics of Semiconductors 2014 (ICPS14), Austin, TX (Invited Talk)

Acknowledgements

At this point, as the end of my PhD is approaching very fast, I realise there are so many people I would like to thank for their kindness and support during the last years.

First and most importantly, I would like to thank my advisor Richard J. Warburton, who inspired, encouraged and motivated me. He always had the right ideas and guidance that made the achievements in this thesis possible. Richard, I am very glad for the possibility of being a part of your group, not only here in Basel, yet already during my master project back in Edinburgh. Thank you Dr. Gian Salis for accepting to be in my PhD committee on rather short notice and for reading my PhD thesis. And many thanks to Prof. Martino Poggio for chairing my defence.

Many thanks to the entire Nano-Photonics Group, especially the people with whom I worked the most: Andreas Kuhlmann and Julien Houel. We spend countless hours in the dark lab, trying to figure out various problems, building optics or trying to get the software running. Thank you Julien for helping me in the beginning of my PhD, explaining with patience the details of the experiments and motivating me to keep going during the first problems with the samples. Andi it was a pleasure working and discussing with you, but not only that, you have been a friend since the beginning of my studies in Würzburg, went with me to Scotland and even convinced me to run a Marathon. A special thanks goes to Gunter Wüst and Lukas Greuter, who started their PhD together with me and now share the task of writing their thesis. Thank you Luuki for introducing me to the work in the clean room and Gunter for the time we spent together when we were setting up the labs in the beginning or working on the Meridian project. And of course for introducing me to mountain biking. Furthermore it was a pleasure to work in the same office with you guys and I very much enjoyed the discussions about the world's problems during the coffee break or the occasional beer. Thanks to the rest of the Warburton group for the discussions and joint lunch breaks: Mathieu Munsch, Sebastian Starosielec, Timo Kaldewey, Daniel Riedel, Jan-Philipp Jahn, Daniel Najer, Martina Renggli and our guest Martha Arcari.

I want to thank Arne Ludwig and Prof. Andreas Wieck which provided the high quality samples. Especially Arne, who always answered questions about the samples, the structure and the material composition. Thanks to the Poggio and Maletinsky group for the joint Journal clubs in the past.

Certainly the work presented in this thesis would not be possible, if not for the mechanical and electronics workshop. Great thanks to Sascha Martin and Michael Steinacher, but as well to the rest of the technical staff, Dominik Sifrig and Patrick Stöcklin for providing always liquid Helium and Daniel Sacker for sharing the responsibility for the ICP etching machine. I am grateful for the administrative help, if there was something to send back or if I had to deal with the insurance you knew what to do. Thank you Germaine Weaver, Audrey Fischer, Astrid Kalt and Barbara Kammermann.

Many thanks for the discussions and support regarding the simplest questions about k·p or other theories goes to Franziska Maier and Christoph Klöffel. And thank you Christoph for the great time at the Unisport, especially the Lauftraining and Crossfit.

Isla, Dennis, Michele and Brandon thanks for being my flat mates. Thank you Isla for your friendship, I learned a lot from you about Switzerland and you helped me to feel welcome in Basel. Thank you Dennis for proofreading parts of the thesis, drinking beer, discussing and living together, hihi. And Michele for providing me with delicious italian food and the great holiday in Lecce.

Great thanks to all other people I met during my studies and my time in Basel, and with whom I enjoyed living.

Very last the greatest thanks goes to my family, especially to my parents who supported me at every point of my life. And to the "Brüderrat": Micha, Simeon, Lukas and Matthäus, it is a real privilege sharing the biggest troubles and greatest joys in life with you.